

A SYNTHESIZED DIRECTLY GEOREFERENCED REMOTE SENSING TECHNIQUE FOR
SMALL UNMANNED AERIAL VEHICLES

By

JOHN HENDRIX PERRY

A THESIS PRESENTED TO THE GRADUATE SCHOOL
OF THE UNIVERSITY OF FLORIDA IN PARTIAL FULFILLMENT
OF THE REQUIREMENTS FOR THE DEGREE OF
MASTER OF SCIENCE

UNIVERSITY OF FLORIDA

2009

© 2009 John Hendrix Perry

To Billy Perry

ACKNOWLEDGMENTS

Thank you, Mom and Dad, for lugging me to the library every week during my more precocious years. Thank you, Fran and Doctor D., for encouraging me during the years I was less so. Kelly, thank you for your support and for always being there, I couldn't have done this without you.

A great deal of recognition is owed to all of the researchers who have contributed to the UF UAV project; it couldn't be done without the strong cooperation of an interdisciplinary team. Scott, thanks for getting me up and running on UAV research. Adam, thank you for your effort and for getting me involved early on. To the late Michael Morton, you will be missed and were an inspiration to us all. Matt, you are a tremendous asset to this program and were my right hand man through this past year. Josh, thanks for the effort and huge contribution to the work on synchronization. Brandon, thank you for the hours of layup to get the fleet of UAVs in the air, I look forward to working with you more. Thank you to the faculty, especially Dr. Percival and Dr. Ifju, who have kept this project going and giving us all the chance to lose some sleep on a worthwhile research effort. Thank you also to our collaborators in the Army Corp of Engineers, who have been solid supporters of our work.

Being a part of the Geomatics Program at the University of Florida has been an excellent experience. Thank you, Dr. Mohamed, for giving me the challenge to explore new fields and develop my math chops. Dr. Dewitt, you have had a huge impact on my work, and not just because of your advice to join the program. Thanks especially to Ben for being a knowledgeable colleague willing to exchange new ideas. Finally, thank you to Damon and Shane for being willing to get out and do some surveying at the Lightning Lab; good luck to both of you in your careers.

TABLE OF CONTENTS

	<u>page</u>
ACKNOWLEDGMENTS.....	4
LIST OF TABLES.....	7
LIST OF FIGURES	8
LIST OF ABBREVIATIONS	11
ABSTRACT	14
CHAPTER	
1 INTRODUCTION.....	16
The NOVA II Project.....	16
Technique Motivation.....	18
Direct Georeferencing.....	19
Previous Approaches.....	20
2 GEOMETRIC MODEL.....	24
Coordinate Systems.....	24
Camera Geometry	27
Interior Orientation Parameters	30
Exterior Orientation Parameters.....	32
Scene Geometry	34
3 PAYLOAD DESCRIPTION	39
Design Goals	39
Imaging System.....	39
Navigation System	40
Sensor Synchronization	44
Payload Control and Data Management	46
Hardware	46
Software.....	47
4 PAYLOAD CALIBRATION AND EVALUATION.....	52
Camera Calibration	52
Boresight and Leverarm Calibration.....	54
Navigation Accuracy.....	59
Synchronization Accuracy.....	61
Image Overlap and Flight Planning	69

5	PROCESSING ALGORITHM.....	87
	Overview of the Algorithm.....	87
	Preprocessing.....	88
	Interest Point Generation	91
	Initial Approximation.....	92
	Semi-Automatic Point Matching.....	95
	Bundle Adjustment.....	100
	Surface Generation.....	104
	Mosaicing	108
	Software Implementation.....	111
6	ASSESSMENT AND CONCLUSIONS	119
	Assessment	119
	Conclusions	122
	Recommendations	124
APPENDIX		
A	EXAMPLE NOVA II DATA	131
B	LIGHTNING LAB CALIBRATION SITE.....	134
C	BUNDLE ADJUSTMENT DEVELOPMENT	138
	LIST OF REFERENCES	147
	BIOGRAPHICAL SKETCH	154

LIST OF TABLES

<u>Table</u>		<u>page</u>
4-1	SCBA-adjusted IOPs for the Lightning Lab camera calibration data set	76
4-2	SCBA-adjusted EOPs for the Lightning Lab camera calibration data set.....	76
4-3	Boresight and leverarm calibration results	76
4-4	Navigation system benchmarking results	76
4-5	The calculated RMS error in the navigation parameters due to synchronization error and aperture uncertainty in the navigation parameters for the given dynamics.....	76
4-6	Ground coverage and overlap parameters for typical NOVA II flight lines	77
6-1	Corrections to the exterior orientation parameters obtained by the bundle adjustment of the assessed data set.....	127
A-1	Description of data packets generated by the NOVA II payload.....	132
B-1	Lightning Lab Calibration Site permanent reference monument coordinates.....	135
B-2	Lightning Lab Calibration Site aerial target coordinates.....	135

LIST OF FIGURES

<u>Figure</u>		<u>page</u>
1-1	Preparing the NOVA II for launch.....	23
2-1	The (a) image coordinate system, (b) navigation coordinate system, and (c) local-level coordinate system illustrated	37
2-2	Illustration of four types of distortions caused by miscalibration of the interior orientation parameters.....	38
3-1	The effect of throttling up the NOVA II electric motor on the payload magnetometer at full throttle (70 amp draw).....	49
3-2	Architecture of the NOVA II Payload	49
3-3	Diagram of the Burredo's operation	50
3-4	Comparison of the Burredo's size through iterations of development	50
3-5	Preparing to load the payload into the NOVA II, arranged beside the plane in their approximate locations inside the airframe	51
3-6	Close-ups of the sensor package (left) and controller package (right)	51
4-1	Lightning Lab Calibration Site calibration data set images 770, 796, 812, 894, 919, and 1004.....	77
4-2	Comparison of the SPAN® and MTi-G™ attitude parameters over time for the static (left) and dynamic (right) portions of the navigation benchmarking experiment	78
4-3	Error profiles of MTi-G™ position and orientation parameters during the static (left) and dynamic (right) portions of the navigation benchmarking experiment	79
4-4	Distribution of the pseudo-random triggers as a fraction of the UTC second during the synchronization accuracy assessment	80
4-5	Evident linear trend in the error of the uncorrected synchronization data attributed to ΔT_{reset}	80
4-6	The correlation of the synchronization error to the fraction of the UTC second at which it occurred plotted against possible values of ΔT_{reset}	80
4-7	The value of the synchronization error over time in hundreds of nanoseconds.....	80
4-8	Normal probability plot of the synchronization error showing low kurtosis	81
4-9	Drift of the Burredo's crystal oscillator over time	81

4-10	Typical NOVA II dynamics while flying straight and level	81
4-11	Flight planning guide for determining flying height and flight line spacing for a desired overlap	82
4-12	Typical flight line configuration for the NOVA II, demonstrating the 'dipole' pattern.....	83
4-13	Example of the image overlap configuration for a typical NOVA II flight	83
4-14	Sequential-image airbase for a typical NOVA II flight showing variations due to flight direction relative to the prevailing wind.....	84
4-15	Typical horizontal deviation of the NOVA II from an ideal flight line.....	84
4-16	Typical vertical deviation of the NOVA II from an ideal flight line	85
4-17	Typical orientation deviation of the NOVA II from ideal flight line.....	85
4-18	Coverage map for a two-day data collection mission conducted on behalf of the Army Corp of Engineers.....	86
5-1	Example of the Log-Polar Transformation. The origin of the transform is the center of the source image with $M = 72$, Source: [Lena]	116
5-2	Comparison of IDW (left) and Kriging (right) interpolation techniques demonstrating the 'bullseye' effect of the IDW	116
5-3	Comparison of resampling techniques at 200% enlargement, Source: [Lena]	117
5-4	Example correct tie point matches between source (left) and target (right) images, matched template in green and search space in red	118
5-5	Example of an incorrect tie point matches due to poor initial approximation of the image boundary, matched template in green and search space in red	118
6-1	The distribution of tie points for the first (left) and second (right) iteration of the assessed data set	128
6-2	Distribution of mosaic seam error measurements and their values.....	128
6-3	Comparison of the mosaic (left) to the unadjusted direct projection of one of the composing images (right) showing the magnitude of the adjustment	129
6-4	Detail of typical mosaicing seam errors at the farther distance from nadir (left) and due to vertical relief in the image (right)	129
6-5	Demonstration of detail with observations of a (a) low flying bird, (b) wading birds, a (c) basking alligator, and (d) swimming alligators	130

A-1	Example snippet of the raw NOVA II log file	133
A-2	Example snippet of the generated NOVA II geotags file	133
B-1	Physical Design of the Lightning Lab Ground Control Point Aerial Targets	136
B-2	Aerial view of the Lightning Lab Calibration Site Targets indicating the target distribution.....	136
B-3	Aerial view of the Lightning Lab Calibration Site Targets captured by NOVA II with a zoomed inset of an individual target	137
B-4	NGS Control Monument KINGSLEY (left) and GPS setup (right)	137

LIST OF ABBREVIATIONS

AT	Aerotriangulation
BA	Bundle Adjustment
BLC	Boresight and Leverarm Calibration
CEP	Circular Error Probable
cm	Centimeter
COTS	Consumer Off-The-Shelf
DAQ	Digital Acquisition Card
DCM	Direction Cosine Matrix
DEM	Digital Elevation Model
DG	Direct Georeferencing
DGRS	Directly Georeferenced Remote Sensing
DLT	Direct Linear Transformation
DMS	Degrees Minutes Seconds
DSM	Digital Surface Model
ECEF	Earth Centered Earth Fixed
EOP	Exterior Orientation Parameters
FFT	Fast-Fourier Transform
GCP	Ground Control Points
GCS	Ground Control Station
GPS	Global Positioning System
HCD	Harris Corner Detector
HSV	Hue-Saturation-Value
Hz	Hertz
IDW	Inverse Distance Weighted

IMU	Inertial Measurement Unit
INS	Inertial Navigation System
IOP	Interior Orientation Parameters
KML	Keyhole Markup Language
LiDAR	Light Detection and Ranging
LPT	Log-Polar Transformation
LSM	Least-Squares Matching
M	Meters
mm	Millimeters
m/s	Meters per Second
ms	Millisecond
μs	Microsecond
MEMS	Micro Electro-Mechanical Systems
NCC	Normalized Cross-Correlation
NGS	National Geodetic Survey
ns	Nanosecond
OPK	Omega Phi Kappa
PPS	Pulse Per Second
PRM	Permanent Reference Monument
RANSAC	Random Sample Consensus
RGB	Red-Green-Blue
RMS	Root Mean Squared
RPY	Roll Pitch Yaw
RTK	Real-Time Kinematic
SATA	Serial Asynchronous Transfer Attachment

SCBA	Self-Calibrating Bundle Adjustment
SLR	Single Lens Reflex
UAV	Unmanned Aerial Vehicle
UTC	Coordinated Universal Time
UTM	Universal Transverse Mercator
V	Volt
VGA	Video Graphics Array
ZUPT	Zero-velocity Update

Abstract of Thesis Presented to the Graduate School
of the University of Florida in Partial Fulfillment of the
Requirements for the Degree of Master of Science

**A SYNTHESIZED DIRECTLY GEOREFERENCED REMOTE SENSING TECHNIQUE FOR
SMALL UNMANNED AERIAL VEHICLES**

By

John Hendrix Perry

August 2009

Chair: Ahmed Mohamed

Major: Forest Resources and Conservation

Directly georeferenced remote sensing is an emerging technique for rapidly gathering accurate and repeatable observations of the landscape. It refers to the ability to independently reconstruct the geometry of the remotely sensed data, allowing the data to be transformed into both maps and three dimensional representations. While direct georeferencing is becoming an established technique on both satellites and manned-aircraft platforms, the implementation on small, hand-launchable unmanned aerial vehicle platforms has been limited due to significant challenges in system integration and sensor accuracy imposed by the platform. A synthesized approach to directly georeferenced remote sensing on a small unmanned aerial vehicle is presented. An order-of-magnitude improvement in the mosaicing seam error over a naïve direct georeferencing approach is demonstrated using field data. Development of the technique is presented in a comprehensive and systematic examination of each essential element of directly georeferenced remote sensing.

The use of empirical models for each element of the approach from raw data to finished product allows for a consistent and reliable evaluation of its accuracy. The geometric model of image formation including camera distortion is developed, and the spatiotemporal integration with the navigation system to accomplish direct georeferencing is formulated and examined in

detail. Payload calibration procedures are developed and analyzed, together with a description of the Lightning Lab Calibration Site, a permanent installation for the calibration and evaluation of UAV-based payloads. The development of the physical payload and operational considerations such as flight planning and required overlap are evaluated. A novel sensor synchronization architecture is described and an error model for synchronization developed and analyzed. A synthesized processing algorithm is developed along with a survey of alternative approaches and potential improvements. The implementation of the algorithm is described and the accuracy of the algorithm is assessed using field data. Limitations of the technique are identified and examined throughout, with recommendations for future developments.

CHAPTER 1

INTRODUCTION

The NOVA II Project

The NOVA II is the most recent evolution of a decade-long interdisciplinary project at the University of Florida to develop a lightweight unmanned aerial vehicle for remote sensing applications [Jones, 2003]. With each successive generation of UAV development, the project has improved the performance and capability of the platform, with great strides being made in flight duration, airframe ruggedness, flight stability, operational flexibility, and payload capacity [Bowman, 2008]. The recent success of the program in transferring the NOVA II platform to operational use with the Army Corp of Engineers is a testament to the maturation of the platform [Burgess et al., 2009]. This transition has signaled that the capability of the small UAV platform for remote sensing in the civilian sector is moving from possible to practical. The NOVA II is pictured in Figure 1-1.

The basic motivation for developing the NOVA II is the need for georeferenced aerial imagery. The ubiquitous adoption of geographic information systems such as Google Earth® and Microsoft Virtual Earth® has only increased the need for spatially registered imagery in an immense variety of applications. Current methods for collecting and updating this imagery rely on manned aircraft and satellite-based remote sensing platforms. Limitations of these platforms include high cost and difficulty of deployment, limited resolution due to flying height restrictions, and risk to human life. In contrast, the small UAV paradigm offers the potential for: 1) low cost, rapid deployment, 2) high resolution, and 3) low risk to operators [Bowman, 2008]. The applications often cited for this UAV-based imagery include infrastructure and environmental monitoring, disaster response and recovery, and surveying and land use planning [Cox et al., 2004; Jones et al., 2006]. Georeferencing is a critical component of these

applications, allowing both localization of features in the image as well as repeatable observations of the scene over time [Bowman, 2008].

Development of the NOVA II has been geared toward specific applications that are of interest to program collaborators. These missions reflect the particular advantages of the small UAV platform. In cooperation with the Army Corp of Engineers, the use of the NOVA II for monitoring invasive aquatic plant species has been highlighted [Bowman et al., 2008]. This application emphasizes the remote operation capabilities of the UAV, as well as the ability to frequently deploy the system for repeatable observations in change detection application. A long-time goal of the program has been adapting small UAVs for wildlife population research, for which the platform is uniquely suitable [Wilkinson, 2007; Jones, 2003]. For this application, very high image resolution for species and nest identification, the dangerously (for manned aircraft) low flying heights, quiet operation, and spatial and temporal repeatability all demonstrate the high potential of the small UAV platform.

Accompanying the development of an operational small UAV platform, significant progress has been made in the development of a suitable remote sensing payload. Although the UAV imposes weight and size constraints on the payload, the use of innovative sensor fusion methods for maximize its operational envelope. To pursue this goal, a major redesign of the payload architecture was undertaken in the fall of 2008. A detailed examination of this hardware design and its architectural elements are presented in Chapter 3. The end result of this redesign was a flexible payload architecture capable of delivering the required geospatial data in a robust operational package.

Following the successful implementation of both the new airframe and payload, which together form the NOVA II, the project began deploying the UAV on an operational basis for a

variety of data collection missions. This stage of development was long been anticipated, and had been partially achieved in the previous generation, the NOVA I [Bowman, 2008a]. However, it presented the new research challenge of developing a robust method for turning the raw data into a deliverable remote sensing product. For each previous generation of the project, methods had been proposed or developed for processing the data delivered by the system [Bowman, 2008; Wilkinson, 2007], however, the previous approaches were incompatible or inadequate for exploiting the new suite of sensors available on the NOVA II.

Technique Motivation

The development of the payload, calibration, and processing techniques stood to take advantage of the two principal sensors on the payload, a high-resolution imaging system and a consumer grade INS/GPS. Together, these two sensors can theoretically deliver georeferenced aerial imagery over terrain with no a priori terrain model or control through the use of a directly georeferenced remote sensing system. The approaches presented in this thesis are intended to fulfill this possibility by fusing all available sensor information to produce a georeferenced and rectified mosaic of the scene.

The emphasis on ‘synthesis’ in describing the proposed technique is purposeful. A great number of methods have been developed for each element of the proposed technique, drawing primarily from the fields of robotics and photogrammetry. The development of the technique was thus guided by the investigation and selection of a suitable approach for each element of the algorithm, and the resulting synthesis of the individual elements producing a novel method for approaching the DGGS paradigm.

Importantly, it should be noted that the scope of the proposed technique is limited to processing data derived from the operational envelope of the data collection platform. Limiting the scope of the technique has the dual impact of optimizing the solvability and effectiveness of

the algorithm for this specific platform, but also limiting the robustness of the technique in more general applications. However, a more general approach is certainly desirable. To this end, the constraints and assumptions of the proposed algorithm are described to the greatest extent possible throughout the thesis, and improvements and alternatives are proposed where possible. As will be demonstrated, it is ultimately the observability of the desired information and the availability of initial approximations which constrains the generality of the algorithm.

Direct Georeferencing

Direct georeferencing is clearly a central theme here, and the concept itself deserves some elucidation. A definition of direct georeferencing is not well established in the general photogrammetric community, perhaps because of the variety of algorithms and systems, including the one described in this thesis, which exploit it (or at least the term). A precise definition might be ‘Direct georeferencing is the act of determining the attitude and position of a remote sensing system at the moment of exposure.’ This definition is by no means simplistic, and implies the key concept that direct georeferencing is necessarily an exercise in sensor integration, wherein the remote sensing system is integrated with a navigation system both spatially and temporally. However, by merely defining direct georeferencing in terms of systems integration, it belies the rich potential of the technique which it proposes. Determining the position and attitude of the imaging sensor does little without exploiting the data synthesis that is made possible by direct georeferencing.

A refined definition of direct georeferencing is therefore proposed: ‘Direct georeferencing is the process of independently reconstructing the geometry of remotely sensed data by integration of remote sensing and navigation systems.’ What this definition loses in conciseness is more than made up for by the explicit description of the purpose of direct georeferencing. It is put forth that direct georeferencing is a process composed of several essential elements. It is true

that this process is in large part a synthesis of well-formed methods. Much is of the methodology is shared with traditional photogrammetry, computer vision, and built upon the rudiments of implementing and integrating remote sensing and navigation systems. However, direct georeferencing offers novel challenges and unique advantages through sensor fusion.

Under this proposed definition, direct georeferencing gains a unique identity among the other methods of reconstructing the geometry of remotely sensed data. Beside the aforementioned aspects of integrating the sensor systems, direct georeferencing is further defined by the independent reconstruction of the geometry. That is, the process of direct georeferencing proceeds with nothing more than the parameters and data associated with its sensor suite. No ground control is needed; no defined scene composition, or a priori terrain model. This definition is perhaps too narrow, since there are processing techniques which invoke the term direct georeferencing but in fact exploit extensive a priori information. To this end, it can be stated up front that a direct georeferencing technique, as defined, is not universally valid. Being directly georeferenced is not a sufficient property of remotely sensed data for the scene geometry to be independently reconstructed.

Previous Approaches

As mentioned, the proposed direct georeferencing technique is synthesized from a number of different scientific fields, and a practical review of the full scope of previous methods from which it derives is not feasible here. To the extent possible, previous approaches to individual elements of the technique are described as the individual elements are discussed. For the purposes of overview, however, the proposed technique is a direct georeferencing technique, and should thus be compared to other direct georeferencing approaches.

Direct georeferencing as a photogrammetric technique is relatively new, coinciding with the availability of the global positioning system (GPS) and inertial navigation systems (INS)

capable of providing sufficiently accurate position and orientation parameters. From the first indications of its advent in the 1980's to the development of practical system implementations in the 1990's, there has been a continual expansion in the recognition of its potential in the photogrammetry community [Mohamed and Price, 2002]. This gave rise to a point of contention within the discipline as to whether direct georeferencing makes methods which require ground control points or other a priori information for a photogrammetric solution obsolete [Cramer, 1999; Greening et al., 2000]. For the proposed technique, as with previous direct georeferencing techniques, it is premature to envision it as a sufficiently robust and accurate method to replace traditional photogrammetric methods for high-accuracy remote sensing applications. However, the operational envelope of the NOVA II leaves little choice in the matter; it is designed and must operate in environments where ground control is not practically available.

Fundamentally, direct georeferencing techniques use position and attitude measurements from an INS/GPS to provide estimates for the exterior orientation parameters of the imaging system [Cramer and Stallman, 2000]. In comparison, traditional photogrammetric techniques recover these parameters by use of space resection by collinearity in the case of a single image and aerotriangulation in the case where a strip of overlapping images is available [Wolf and Dewitt, 2000]. Essentially, the navigation solution is used as the geometric control in the photogrammetric solution rather than ground control points. Once the exterior orientation parameters of the image are recovered, the normal photogrammetric process of generating rectified aerial images is continued. That is, either an extrinsic scene model (e.g., a Digital Elevation Model of LiDAR data) or an intrinsic scene model generated using photogrammetry is used as a surface on which the aerial images are projected and resampled [Mohamed and Price,

2002; Jung and Lacroix, 2003]. Direct georeferencing techniques using LiDAR have been fully implemented on a UAV, but due to size of the NOVA II was not applicable [Nagai et al., 2009].

A significant difference between previous direct georeferencing methods and the proposed technique arise from the difference in the accuracy of the INS/GPS measurements. In typical direct georeferencing scenarios, the IMU has an accuracy of 1°/hr or better [Mostafa and Schwarz, 2000]. Due to size and weight limitations of NOVA II payloads, current commercially-available technology is not capable of delivering this level of accuracy on the NOVA II platform. To compensate, sensor fusion is used to improve the solution with additional geometric information derived from the photogrammetric observations. This does not mean that ground control or surface models are required; the photogrammetric observations may be limited to the intrinsic geometry of image formation. This approach has been termed ‘Integrated Sensor Orientation’ in the photogrammetric community [Khoshelham, 2009], although the usage is not well defined and is also used to refer to combined direct georeferencing and aerotriangulation [Heipke et al., 2002]. Optimally reconstructing the image and scene in a simultaneous adjustment is a well developed technique regardless of the use of control points [Triggs et al., 1999] and is nearly universal in traditional aerotriangulation. [Wolf and Dewitt, 2000].

In the NOVA I, direct georeferencing was implemented by projecting each captured image to a flat surface. Multiple-image geometry was not considered, and mosaicing was not implemented. The horizontal accuracy attained using this method was reported to be 67.6 m RMS [Bowman, 2008a]. This method of using a naïve projection model to a flat surface has been used widely for rudimentary DGRS payloads on a number of UAV systems [Taylor and Anderson, 2008; Xiang and Tian, 2007]. This method compares poorly to photogrammetrically adjusted direct georeferencing solutions found by a fully calibrated metric camera with high-

accuracy navigation systems on traditional aerial platforms, which have been shown to attain horizontal accuracies on the order of centimeters [Cramer and Stallman, 2000]. The proposed technique is intended to improve upon the results of the NOVA I, with the goal of approaching the accuracy of existing larger systems.



Figure 1-1. Preparing the NOVA II for launch

CHAPTER 2 GEOMETRIC MODEL

Coordinate Systems

To begin the development, several Cartesian coordinate frames must be introduced.

Traditional photogrammetry usually employs two coordinate systems, one in the image space and the other in object space. Direct georeferencing requires a third coordinate system for the navigation system, referred to in this paper as the navigation coordinate system. The object space coordinate system is usually defined in the local-level frame, a right-handed coordinate system with an origin at some position defined in a geodetic coordinate system such as graticular latitude and longitude or ECEF. The X and Y axes, along the East and North directions respectively, form a plane tangent to the surface of an earth ellipsoid. The Z axis is normal to the ellipsoid, completing the right-handed system, as illustrated in Figure 2-1(c).

Although the following mathematical development is made in a local-level orthogonal system, it is common to use a conformal mapping projection such as the Universal Transverse Mercator for the object space coordinate system in direct georeferencing to reduce the computation cost of generating output maps [Legat, 2006]. However, this introduces error into the solution due to the curvature of the earth and the vertical relief of the terrain [Ressl, 2002]. A more rigorous solution is found by reconstructing the geometry in a local-level coordinate system defined at the center of the scene, and subsequently transforming the object space coordinate system to a mapping projection using geodetic methods. For a detailed examination of the problems associated with using a conformal mapping projection in direct georeferencing, the reader is referred to [Skaloud and Legat, 2007; Legat, 2006; and Ressl 2002]. In general, these effects are minimal over small land areas when the terrain is essentially at sea level.

The image is a right-handed coordinate system defined with an origin at the perspective center of the camera. The X and Y axes define a plane parallel to the imaging sensor. For the purposes of this research, the X and Y axes correspond to the rightward and upward directions respectively when holding the camera as if you were taking a normal picture. The Z axis of the image coordinate system completes the right-hand coordinate system and extends positively in the direction of the photographer. The intersection of the Z axis of the imaging coordinate system (the ‘optical axis’) with the plane of the image sensor is the principal point. To avoid the complication of dealing with an inverted image, the image sensor can be virtually located ‘in front’ of the perspective center, as shown in Figure 2-1(a). We can thus define the position vector of the perspective center of the camera in the object space, $[X_L, Y_L, Z_L]^T$, and a position vector for any feature in the object space, $[X_I, Y_I, Z_I]^T$, corresponding to a feature in the image space, $[x_I, y_I, z_I]^T$.

The navigation coordinate system is defined by the body frame composed of the ideal sensing axes of the dual triad of accelerometers and gyroscopes in the inertial navigation system. To avoid confusion in nomenclature, it should be made clear that in this thesis the navigation coordinate system is equivalent to the body coordinate system when defined relative to the local-level frame as is commonly found in navigation literature. This system is idealized in the sense that the navigation sensors will not be perfectly aligned in space and will not be truly orthogonal [Schwarz and Wei, 2000]. Its origin is defined at the convergence of these axes, and is illustrated in Figure 2-1(b). The origin is denoted in the object space by $[X_N, Y_N, Z_N]^T$.

The orientations of the image and navigation coordinate system with respect to the object coordinate system can be defined by equivalent Euler angles, direction cosine matrices, or quaternions [Kuipers, 1999]. The rotations are usually expressed using Euler angles and

computed using a DCM. Two conventions are commonly used; 1) omega-phi-kappa for the image coordinate system, and 2) roll-pitch-yaw for the navigation coordinate system. These conventions differ by the direction, order, and choice of axes about which the sequential Euler angles are applied. In this thesis the latter is used only when explicitly noted, and in all cases the OPK convention is used for photogrammetric implementation. We thus denote the rotation from the object coordinate system to the image coordinate system by $R_I = [\omega_I, \phi_I, \kappa_I]^T$ and the navigation coordinate system to the object coordinate system by $R_N = [\phi_N, \theta_N, \psi_N]^T$. The equivalent DCM rotations are given by Equations 2-1 and 2-2.

$$R_I = \begin{bmatrix} \cos \phi_I \cos \kappa_I & \sin \omega_I \sin \phi_I \cos \kappa_I + \cos \omega_I \sin \kappa_I & -\cos \omega_I \sin \phi_I \cos \kappa_I + \sin \omega_I \sin \kappa_I \\ -\cos \phi_I \sin \kappa_I & -\sin \omega_I \sin \phi_I \sin \kappa_I + \cos \omega_I \cos \kappa_I & \cos \omega_I \sin \phi_I \sin \kappa_I + \sin \omega_I \cos \kappa_I \\ \sin \phi_I & -\sin \omega_I \cos \phi_I & \cos \omega_I \cos \phi_I \end{bmatrix} \quad (2-1)$$

$$R_N = \begin{bmatrix} \cos \theta_N \cos \psi_N & \sin \phi_N \sin \theta_N \cos \psi_N - \cos \phi_N \sin \psi_N & \cos \phi_N \sin \theta_N \cos \psi_N + \sin \phi_N \sin \psi_N \\ \cos \theta_N \sin \psi_N & \sin \phi_N \sin \theta_N \sin \psi_N + \cos \phi_N \cos \psi_N & \cos \phi_N \sin \theta_N \sin \psi_N - \sin \phi_N \cos \psi_N \\ -\sin \theta_N & \sin \phi_N \cos \theta_N & \cos \phi_N \cos \theta_N \end{bmatrix} \quad (2-2)$$

Some geodetic transformations are of practical interest in direct georeferencing. Particularly, the navigation coordinate system origin provided by a GPS unit will usually be given in WGS84 latitude, longitude, and height above the ellipsoid. To convert this value to the object space system defined by a local level frame, it is necessary to first convert the latitude, longitude and height to ECEF coordinates using Equation 2-3, which uses the WGS84 ellipsoid parameters [Wolf and Dewitt, 2000]. Using the same formula, the origin of the object coordinate system should also be known.

$$X_{ECEF} = (N + h) \cos(\lambda) \cos(\phi)$$

$$Y_{ECEF} = (N + h) \cos(\lambda) \sin(\phi)$$

$$Z_{ECEF} = \left(\frac{Nb^2}{a^2} + h \right) \sin(\lambda)$$

$$N = \frac{a}{\sqrt{1 - e^2 \sin^2(\lambda)}}$$

$$a = 6378137.000000 \text{ m}, \quad b = 6,356,752.314245 \text{ m}, \quad e = \frac{1}{298.257223563}$$

$$\lambda = \text{latitude (rads)}, \quad \phi = \text{longitude (rads)}, \quad h = \text{HAE (m)} \quad (2-3)$$

A vector between the origin of the object space and the navigation coordinate system can then be calculated in the ECEF coordinate system and by rigid body transformation converted to the local level coordinates system, as given in Equation 2-4.

$$\begin{aligned} \begin{bmatrix} X_N \\ Y_N \\ Z_N \end{bmatrix} &= R_{ECEF}^L \begin{bmatrix} X_{ECEF} - X_O \\ Y_{ECEF} - Y_O \\ Z_{ECEF} - Z_O \end{bmatrix} + \begin{bmatrix} X_O \\ Y_O \\ Z_O \end{bmatrix} \\ R_{ECEF}^L &= \begin{bmatrix} -\sin(\phi) & \cos(\phi) & 0 \\ -\sin(\lambda) \cos(\phi) & -\sin(\lambda) \sin(\phi) & \cos(\lambda) \\ \cos(\lambda) \cos(\phi) & \cos(\lambda) \sin(\phi) & \sin(\lambda) \end{bmatrix} \\ \begin{bmatrix} X_O \\ Y_O \\ Z_O \end{bmatrix} &= \text{Origin of the object coordinate system defined in ECEF coordinates} \end{aligned} \quad (2-4)$$

Camera Geometry

The geometry of camera image formation is described by a perspective projective transformation [Wolf and Dewitt, 2000]. The perspective projective transformation development proceeds by first giving a transformation up to a scaling factor between the image and object space as in Equation 2-5.

$$\begin{bmatrix} x_I \\ y_I \\ z_I \end{bmatrix} = R_I \begin{bmatrix} X_I - X_L \\ Y_I - Y_L \\ Z_I - Z_L \end{bmatrix} \quad (2-5)$$

Applying R_I to the image coordinate system we introduce a temporary coordinate system whose origin is coincident with the image coordinate system but whose axes are parallel with the local-level system. The vector then becomes $[x'_I, y'_I, z'_I]$, given by Equation 2-6.

$$\begin{aligned} x_I &= m_{11}x'_I + m_{12}y'_I + m_{13}z'_I \\ y_I &= m_{21}x'_I + m_{22}y'_I + m_{23}z'_I \\ z_I &= m_{31}x'_I + m_{32}y'_I + m_{33}z'_I \end{aligned}$$

$$R_I = \begin{bmatrix} m_{11} & m_{12} & m_{13} \\ m_{21} & m_{22} & m_{23} \\ m_{31} & m_{32} & m_{33} \end{bmatrix} \quad (2-6)$$

The collinearity condition states that the perspective center and the corresponding image space and object space coordinates are collinear. This is an ideal condition produced by light rays propagating in straight lines through a uniform medium. The collinearity condition thus produces a relationship of similar triangles (Equation 2-7), and by substitution in Equation 2-6, we deduce Equation 2-8.

$$\frac{x'_I}{X_I - X_L} = -\frac{z'_I}{Z_I}, \quad \frac{y'_I}{Y_I - Y_L} = -\frac{z'_I}{Z_I}, \quad \frac{z'_I}{Z_I - Z_L} = -\frac{z'_I}{Z_L} \quad (2-7)$$

$$\begin{aligned} x_I &= m_{11} \frac{z'_I}{Z_L} (X_I - X_L) + m_{12} \frac{z'_I}{Z_L} (Y_I - Y_L) + m_{13} \frac{z'_I}{Z_L} (Z_I - Z_L) \\ y_I &= m_{21} \frac{z'_I}{Z_L} (X_I - X_L) + m_{22} \frac{z'_I}{Z_L} (Y_I - Y_L) + m_{23} \frac{z'_I}{Z_L} (Z_I - Z_L) \\ z_I &= m_{31} \frac{z'_I}{Z_L} (X_I - X_L) + m_{32} \frac{z'_I}{Z_L} (Y_I - Y_L) + m_{33} \frac{z'_I}{Z_L} (Z_I - Z_L) \end{aligned} \quad (2-8)$$

Dividing x_I and y_I by z_I and noting that $z_I = -f$ we arrive at the ideal collinearity condition, given by Equation 2-9. The collinearity equations in their common form are arranged to solve for the image coordinates. This may be thought of as the ‘Project Up’ development of the collinearity equations, since the arrangement makes it straightforward to solve for the perspective projection of the object space coordinates onto the image space. However, it is usually the case that the image coordinate of some object of interest has been identified, and the local-level coordinates of the image are unknown. To do this, we solve the ‘Project Down’ collinearity equations for the object space coordinates, X_I and Y_I , given by Equation 2-10.

$$x_I = -f \left(\frac{m_{11}(X_I - X_L) + m_{12}(Y_I - Y_L) + m_{13}(Z_I - Z_L)}{m_{31}(X_I - X_L) + m_{32}(Y_I - Y_L) + m_{33}(Z_I - Z_L)} \right)$$

$$y_I = -f \left(\frac{m_{21}(X_I - X_L) + m_{22}(Y_I - Y_L) + m_{23}(Z_I - Z_L)}{m_{31}(X_I - X_L) + m_{32}(Y_I - Y_L) + m_{33}(Z_I - Z_L)} \right) \quad (2-9)$$

$$\begin{aligned} X_I &= \frac{X_L(x_I m_{13} + f m_{11}) - Y_I(x_I m_{23} + f m_{21}) + Y_L(x_I m_{33} + f m_{31})}{f m_{11} + x_I m_{13}} \\ Y_I &= \frac{X_L(y_I m_{31} + f m_{21}) - X_I(y_I m_{31} + f m_{21}) + Y_L(y_I m_{32} + f m_{22}) + (Z_L - Z_I)(y_I m_{33} + f m_{23})}{y_I m_{32} + f m_{22}} \\ Y_I &= \frac{c_1 - c_2}{a_1 - a_2} \\ X_I &= \frac{c_1 - b_1 Y_I}{a_1} \\ a_1 &= x_I m_{31} + f m_{11} \\ b_1 &= x_I m_{32} + f m_{21} \\ c_1 &= a_1 X_L + b_1 Y_L + (f m_{13} + x_I m_{33})(Z_L - Z_I) \\ a_2 &= y_I m_{31} + f m_{21} \\ b_2 &= y_I m_{32} + f m_{22} \\ c_2 &= a_2 X_L + b_2 Y_L + (f m_{23} + y_I m_{33})(Z_L - Z_I) \end{aligned} \quad (2-10)$$

Equivalent to the collinearity equations, the ‘Project Down’ system of equations is not directly solvable because it lacks one degree of freedom under usual circumstances. That is, for given internal and exterior orientation parameters and an image coordinate pair, there remains an ambiguity for solving for the object space coordinate. The ideal collinearity equations provide the fundamental physical model for the geometric reconstruction of a scene from image coordinates. However, this model must be extended with additional parameters in order to model the real-world properties of a camera system [Fraser, 1997].

Before proceeding, an important comment is to be made on alternative developments of camera geometry and image formation. This issue is at the crux of the proposed direct georeferencing technique, since it is central to the rigorous approach to direct georeferencing. It is well known that alternative models for camera geometry can be employed and have some desirable properties [Hartley and Mundy, 1994]. Most notably the use of a projective model or a direct linear transformation, as opposed to the perspective projective geometry developed in this

thesis, is commonly employed as an alternative. However, such models ultimately are not an empirical approach to direct georeferencing [Horn, 1999].

Interior Orientation Parameters

Interior orientation parameters are properties of the optical and physical configuration of the camera lens and sensor. The interior orientation parameters of a camera provide a corrective model to adjust for deviations in the internal camera geometry from the ideal collinearity model. Regardless of the model used, the sum effect of the interior orientation parameters is to produce a corrected image coordinate for use in the collinearity equations [Fraser, 1997]. The interior orientation parameters can be further categorized into intrinsic and distortion parameters. The distortion parameters refer to IOPs which apply a correction that is dependent on the value of the image coordinate under consideration, whereas the intrinsic parameters are constant for all image coordinates. Although there are alternative methods for modeling the IOPs [Ebner, 1976], the interior orientation model described here relies on a set of well-described distortions developed in [Brown, 1971].

The calibrated focal length, or principal distance, is an intrinsic parameter and is typically the most significant because it acts as a scale factor in the collinearity equations, Equation 2-9. The calibrated focal length is defined as the true distance from the rear nodal point of the lens to the principal point. The principal point offsets are intrinsic parameters and are a measurement of the physical offset between the geometric center of the sensor and the optical axis of the lens. The principal point offsets are denoted by x_o and y_o . The presence of principal offsets results in a linear shift of the image coordinate system, as illustrated in Figure 2-2. Principal point offsets are present in most imaging systems, and along with focal length are the most commonly calibrated interior orientation parameters.

Radial distortion is caused by variations in the effective refractive index of the lens along a radial axis. This distortion is common and is usually the largest source of error among the image-coordinate dependent errors for non-metric cameras [Wackrow, 2008]. The distortion is dependent not only on the physical aberrations in the lens, but also on the focusing distance and object distance, although these secondary effects are typically minor. Radial distortion is typically modeled as a Seidel series, an odd-ordered polynomial series as given in Equation 2-11. Typically, lenses are modeled with a Seidel series truncated at the second or third term [Fraser, 1997].

$$\begin{aligned}\Delta x_{rad} &= x \frac{\Delta rad}{r} \\ \Delta y_{rad} &= y \frac{\Delta rad}{r} \\ \Delta rad &= k_1 d^3 + k_2 d^5 + k_3 d^7 + \dots \\ d &= \sqrt{x^2 + y^2} \\ k &= \text{coefficients of radial distortion}\end{aligned}\tag{2-11}$$

Tangential distortion, alternately called radial asymmetric or decentering distortion, is typically caused by misalignment of the optical components of the lens and is given in Equation 2-12 [Kraus, 2007]. The magnitude of this error is usually smaller than radial distortion for high quality lenses, but may be significant for lower quality lenses not designed for metric imaging [Wackrow, 2008].

$$\begin{aligned}\Delta x_{tan} &= t_1(d^2 + 2x^2) + 2t_2xy \\ \Delta y_{tan} &= t_2(d^2 + 2y^2) + 2t_1xy\end{aligned}\tag{2-12}$$

Affinity and shear distortion models the effect of a digital sensing array whose elements have non-uniform scales along each axis and/or are non-orthogonal, given by Equation 2-13.

This error is less common for modern digital cameras, but can be accounted for with the correction formula.

$$\begin{aligned}\Delta x_{aff} &= a_1x + a_2y \\ \Delta y_{aff} &= 0\end{aligned}\tag{2-13}$$

As shown in Equation 2-14, both the intrinsic and distortion parameters can be combined into a single perturbation model, which is added as a correction to Equation 2-9. The distorting effect of miscalibrated interior orientation parameters are illustrated in Figure 2-2.

$$\begin{aligned}x_I &= x_o + \Delta x - f \left(\frac{m_{11}(X_I - X_L) + m_{12}(Y_I - Y_L) + m_{13}(Z_I - Z_L)}{m_{31}(X_I - X_L) + m_{32}(Y_I - Y_L) + m_{33}(Z_I - Z_L)} \right) \\ y_I &= y_o + \Delta y - f \left(\frac{m_{21}(X_I - X_L) + m_{22}(Y_I - Y_L) + m_{23}(Z_I - Z_L)}{m_{31}(X_I - X_L) + m_{32}(Y_I - Y_L) + m_{33}(Z_I - Z_L)} \right) \\ \Delta x &= k_1 x d^2 + k_2 x d^4 + k_3 x d^6 + t_1(d^2 + 2x^2) + 2t_2 x y + a_1 x + a_2 y \\ \Delta y &= k_1 y d^2 + k_2 y d^4 + k_3 y d^6 + 2t_1 x y + t_2(d^2 + 2y^2)\end{aligned}\tag{2-14}$$

Exterior Orientation Parameters

We have now developed a sufficient mathematical foundation to illustrate the use of direct georeferencing. Recall that the physical geometry of camera image formation is described by twelve parameters for the ideal camera in Equation 2-9, with additional interior orientation parameters for a more realistic case as in Equation 2-14. The IOPs can be determined by calibration and may be considered knowns. The parameters of the ideal collinearity equations consist of six exterior orientation parameters $[X_L, Y_L, Z_L, \omega, \phi, \kappa]$, which relate an image point $[x_I, y_I, f]$ to a corresponding object point $[X_I, Y_I, Z_I]$ by a perspective projective transformation. The power of direct georeferencing is in providing direct measurements of the six exterior orientation parameters. It should now be clear why direct georeferencing necessarily provides

both position and orientation data. Using direct georeferencing, the collinearity equations lack only a single unknown for reconstructing the geometry of each element of an image formed by the camera.

The ability to treat the EOPs as directly observed values greatly reduces the complexity of the problem, not only from a mathematical standpoint but also for practical purposes. Without directly observed EOPs, the absolute orientation between the image and object space must be provided entirely by image observations of a priori ground control points. Furthermore, the relative orientation between images can be determined only up to a scale factor without ground control points. This requires not only the availability of observable ground control for a solution, but the ground control must be arranged to provide a sufficiently robust geometry for the photogrammetric solution.

Since it is not feasible to have the navigation coordinate system and image coordinate system physically coincident, it is necessary to apply a boresight and leverarm correction to the navigation parameters in order to use them as EOPs. It is essential that the boresight and leverarm parameters remain constant during flight, a requirement that is satisfied by rigidly mounting the navigation and imaging system relative to each other. This is known as a strapdown sensor configuration. In this configuration, the boresight and leverarm correction amounts to a rigid body transformation in the object space. The three parameters of the lever arm correction, $[X_{LA}, Y_{LA}, Z_{LA}]^T$, are the translation from the origin of the navigation coordinate system to the origin of the image coordinate system defined in the navigation coordinate system. Similarly, the boresight correction requires three Euler angles, $[\omega_B, \phi_B, \kappa_B]$, which orient the navigation coordinate system to the image coordinate system. The boresight and leverarm calibration parameters are applied to the navigation parameters to obtain the EOPs using

Equation 2-15. The optimal estimation of the boresight and leverarm equations is discussed in Chapter 4.

$$\begin{bmatrix} X_L \\ Y_L \\ Z_L \end{bmatrix} = \begin{bmatrix} X_N \\ Y_N \\ Z_N \end{bmatrix} + R_N \begin{bmatrix} X_{LA} \\ Y_{LA} \\ Z_{LA} \end{bmatrix}$$

$$R_I = R_B R_N \quad (2-15)$$

Scene Geometry

Reconstruction of the scene geometry is principally accomplished by solving for the object space coordinates of image features. As noted in the previous section, the collinearity equations for an image feature lack a single degree of freedom given the exterior and interior orientation parameters and image coordinate observations. An additional known is required to resolve the ambiguity, referred to from here on as the Z-ambiguity. It is so named because the ambiguity lies largely along the optical axis (the Z-axis) of the image space. The solution set will lie along the three-dimensional line defined by the collinearity equations, parameterized by a scalar t in Equation 2-16.

$$\begin{aligned} X_I &= X_L + t(m_{11}x_I + m_{12}y_I - m_{13}f) \\ Y_I &= Y_L + t(m_{21}x_I + m_{22}y_I - m_{23}f) \\ Z_I &= Z_L + t(m_{31}x_I + m_{32}y_I - m_{33}f) \end{aligned} \quad (2-16)$$

The additional observations required to resolve the ambiguity may take the form of tie points and control points. A tie point is a feature that is observed in two or more images. Each tie point has three unknowns, which define a position vector in the object space, but each image in which the tie point appears gives two knowns corresponding to the pair of image coordinates. Thus, a tie point that appears in two images will add one degree of freedom to the system of equations, and a tie point that appears in three images will add three degrees of freedom to the system. Resolving the Z-ambiguity using tie points is equivalent in a physical sense to finding

the intersection of the lines formed by the collinearity condition of each image observation. Tie points are necessarily limited to image regions which have stereoscopic coverage, i.e. the object space feature is visible from at least two independent camera exposures.

A control point may or may not be a tie point, but has at least one known position parameter in the object coordinate system. For example, a horizontal control point may have a known easting and northing coordinate, or a vertical control point may have a known height. In traditional photogrammetry, the control point has a central role in the photogrammetric solution because it establishes the absolute orientation. Of course, the goal in the development of a DGRS is to disbar their use entirely as was previously discussed. Therefore, a detailed discussion and development of control points will not be given. In general, however, control points should always be used when available because they provide a valuable constraint to the collinearity equations.

One of the most widely-used techniques for resolving the Z-ambiguity for DGRS is to use an extrinsic or assumed model of the physical geometry of the scene. In these scenarios, the collinearity ambiguity is effectively nonexistent since all three object space parameters are observed, and the photogrammetric solution is reduced to merely finding the corresponding image features for each point of interest on the scene model. The use of extrinsic scene models suffers from a serious limitation that is not initially obvious. The direct resolution of the Z-ambiguity using extrinsic scene models does not equate to the use of control points or tie points in the sense that it does not enforce the geometric consistency or accuracy of the physical image formation. In other words, the correspondence between a particular position on a DEM and a position in the image, as defined by the collinearity equations, does not equate to the empirical correspondence of the actual feature and the image feature. If the EOPs provided by direct

georeferencing are in error, then the reliance on the direct solution of the collinearity equations will result in an incorrect correspondence between the scene and image features. Therefore, the use of scene models should be restricted to cases where the relationship between the camera and scene models is established empirically by enforcing the image formation geometry or where the EOPs provided by direct georeferencing are of sufficiently high accuracy.

The technique presented in this thesis does away with the requirement for a priori control points or scene models, and is similar to classic softcopy photogrammetry techniques for DEM generation [Wolf and Dewitt, 2000]. The modern use of photogrammetrically-generated DEMs has been demonstrated for both high-accuracy direct georeferencing [Yastikli and Jacobsen, 2002] and on larger UAV platforms using ground control points [Eisenbeiss and Zhang, 2006]. The technique relies solely on the photogrammetric reconstruction of a tie point network to reconstruct the scene geometry and thereby generate a surface for resolving the collinearity ambiguity *in situ*. This method is limited to resolving the collinearity ambiguity for features which can be observed in two or more images, and the ambiguity for all other features must be interpolated from the observed features. In the sense that this interpolation results in a DEM, it is similar in outcome to the extrinsic scene model but with the fundamental difference that it is empirically related to the camera geometry.

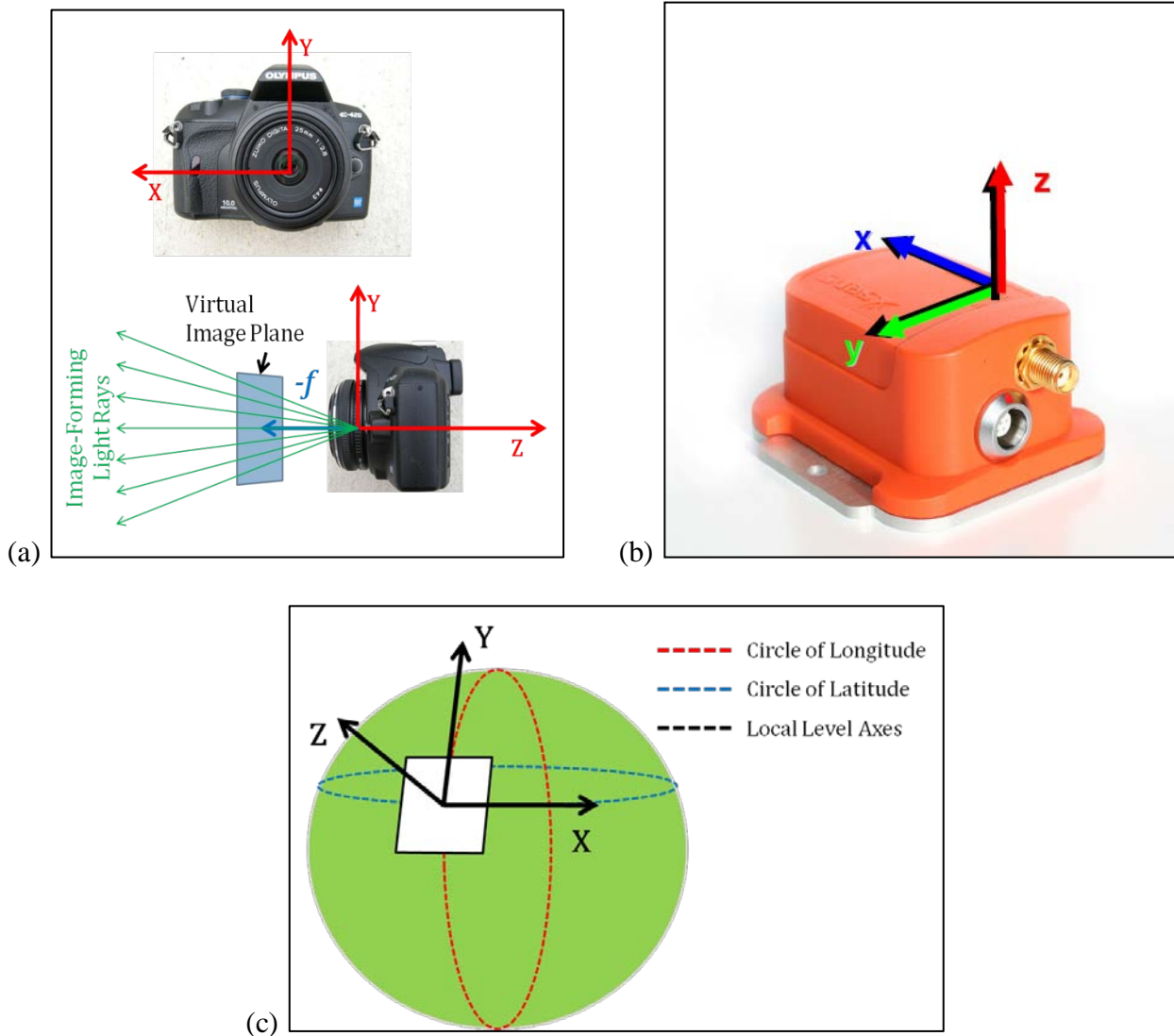


Figure 2-1. The (a) image coordinate system, (b) navigation coordinate system, and (c) local-level coordinate system illustrated

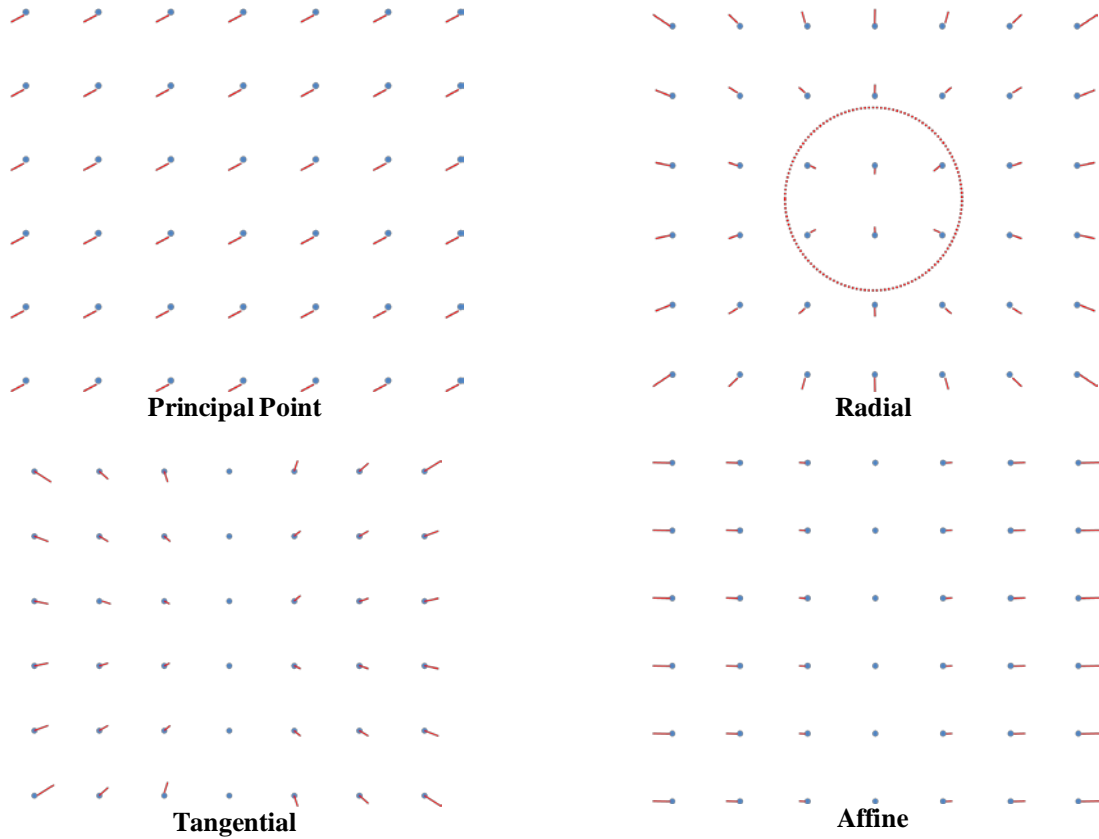


Figure 2-2. Illustration of four types of distortions caused by miscalibration of the interior orientation parameters

CHAPTER 3

PAYOUTLOAD DESCRIPTION

Design Goals

Directly georeferencing airborne data is an exercise in systems integration, and the physical and operational limitations imposed by a small unmanned aerial vehicle constrain the payload [Hruska et al., 2005]. These constraints limit the sensor suite, which tends to increase both in size and ease of integration in direct proportion to the sensor quality and accuracy. Thus, the selection of sensors is a matter of compromise guided by strict design limitations. The design constraints were established by experience gained in previous generations of the NOVA platform and the goal of improving operational and production efficiency, listed here.

- **One kilogram (1 kg) total weight.** The target weight was a component of the airframe design specifications both for flight duration and hand-launch capability.
- **Modular consumer off-the-shelf hardware.** Minimizing cost, ease of replacement, and development time were of primary concern. The ongoing development of the system is a strong deterrent to custom-designed solutions which require specialized knowledge for modification or upgrade.
- **Remote (wireless) and direct (cabled) interfaces.** It is an operational necessity to have remote access to the payload, both for sensor control and for error detection. The large datasets that are generated, however, preclude data transfer over a robust wireless interface. A direct cabling interface is necessary for both post-mission data transfer as well as payload troubleshooting.
- **Unified data bus.** The tight confines of the airframe, as well as the need to minimize electromagnetic interference, suggest the need for simple cabling and interconnects.
- **Single data storage device.** The complexity of the device as well as post-mission data transfer is greatly simplified by having a single repository for all data.

Imaging System

The primary imaging sensor on the NOVA II is an Olympus, Inc. E-420[®] digital single lens reflex camera, see [Olympus E-420] for specifications. This digital camera was selected primarily for its compact size and robust feature set, including a software interface that allows

complete control of the camera settings, exposure triggering, and captured image transfer to the host. A fixed focal length 25mm pancake lens was used due to its light weight and compact size. Important considerations in moving to a digital SLR over the admittedly lighter and smaller consumer point-and shoot-cameras common on most small UAV platforms was the vastly improved optical performance of the available lenses and the low-noise medium-format imaging sensor. This move was foreseen and advised in the analysis of the NOVA I payload [Bowman, 2008]. The overall success of the platform as a remote sensing tool is as reliant on the quality and resolution of the final imagery as much as the accuracy of the mapping.

During a typical mission the camera is operated at the fastest possible exposure speed to minimize the effect of motion blurring. As a result, aperture priority mode is usually set to an exposure duration of 1/2000th of a second or better and an ISO sensitivity of 100. The Olympus automatic exposure metering program, set to shutter priority, has in all experience set the aperture to 2.8 with these parameters under normal daylight conditions. No noticeable motion blurring is seen at these settings, and increasing the exposure duration to 1/4000th does not result in marked improvement in sharpness and has less contrast in lower-light conditions.

Navigation System

The navigation sensors are of paramount importance to the mapping accuracy of the direct georeferencing solution. As discussed in Chapter 2, the navigation sensors provide the EOPs and hence the absolute orientation of the photogrammetric solution. The two canonical components of the navigation system are the IMU and GPS sensors, which are further integrated using a state estimation filter [Chatfield, 1997]. Additional sensors such as magnetometers and air pressure sensors are often used to augment the navigation performance.

Size, weight, and cost restrictions severely limit the selection of the navigation sensors. In general, the selection for small UAV platforms is limited to the two lowest-accuracy classes of

these devices; a MEMS-based IMU and a code-solution single-frequency GPS. As a result, the primary factors in selecting the INS/GPS were the relative accuracy, robust design, and ease of integration. The Xsens, Inc.[®] MTi-G[™] was chosen for implementation. Key features of the MTi-G[™] include a built-in Kalman filter for a real-time orientation parameter solution, a raw data output mode for post-processing refinement, a high update rate, and a simple serial data communication protocol [Xsens MTi-G]. Importantly, an interface is also provided for device synchronization based on the GPS 1PPS signal. A benchmarking experiment and an analysis of the accuracy of this sensor are discussed in Chapter 6.

A brief discussion of inertial navigation and integration with GPS using a Kalman filter is in order due to its importance in direct georeferencing. A canonical INS design consists of a triad of accelerometers axially coincident with a triad of gyroscopes, with the sensing axes of the triads arranged orthogonally. This allows for the measurement of the linear acceleration and angular rate along the axes of the navigation coordinate system relative to an inertial frame of reference. Considering motion within the inertia frame, the position and orientation of a rigid body can be entirely determined from the initial state and the observations of motion by applying Newton's laws of motion. This is summarized by the mechanization of the equation of motion in the inertial frame of reference given in Equation 3-1. Implementation of the laws of motion are complicated by the effects of a rotating frame of reference (earth) introducing the Coriolis effect as well as the definition of the local-level frame.

$$x_i = x_o + \dot{x}_i$$

$$\dot{x}_i = \begin{bmatrix} \dot{P}_i \\ \dot{V}_i \\ \dot{R}_N^i \end{bmatrix} = \begin{bmatrix} V_i \\ R_N^i A_N + G_i \\ R_N^i \Omega_{iN}^N \end{bmatrix}$$

x_i = state vector in the inertial frame

x_o = intial state

$$\begin{aligned}
P_i, V_i, R_N^i &= \text{position, velocity, and orientation in the inertial frame} \\
A_N &= \text{accelerometer measurements} \\
\Omega_{iN}^N &= \text{skew - symmetric form gyroscope measurements} \\
G_i &= \text{gravitational vector in the inertial frame}
\end{aligned}
\tag{3-1}$$

By simple analogy, consider if a ship's navigator were to know that they were at the equator and oriented due north. By dropping a weighted rope in the water and measuring the angle of the rope from vertical, the navigator can determine their average velocity. After a day's sailing, the navigator would simply multiply the measured velocity by the time travelled, giving the distance travelled and their new position. Much like the analogy, the dead reckoning method of inertial navigation is suspect because of the large influence of biased measurement errors compounded in the case of inertial navigation by double integration of the measured acceleration and single integration of the angular rate. This is where the importance of integration with GPS comes into play.

GPS provides both a position and velocity update which can be used to bound the growth of error in the INS solution. This is particularly effective due to the complimentary characteristics of the two systems: GPS error is dominated by short-term white noise whereas the INS error is dominated by long-term drift. On the other hand, GPS provides relatively low-frequency updates whereas INS is typically operated at 100 Hz or more. There are a variety of performance gains by integrating the two systems, but perhaps the most important is the ability to make the bias errors of the INS observable, allowing them to be compensated for. Thus, the typical state vector has fifteen parameters; nine for position, velocity and orientation with six additional parameters for the bias of each inertial sensor. These states are then optimally estimated by employing a Kalman filter, which is an optimal estimator for linear dynamic systems. Integration of INS/GPS is usually accomplished with an Extended Kalman Filter

(EKF). The EKF allows the standard Kalman filter to be extended to nonlinear systems by linearization of the dynamics about the current state. The Kalman filter operates in two stages, a prediction and an update.

In very brief summary, the Kalman filter prediction stage propagates the current state through the system dynamics, providing a prediction of what the next measurement should be if the current states are correct. A state covariance matrix is also propagated through the dynamics. In the update stage, an update is calculated as the difference between the prediction and the update measurement. The Kalman filter gain is calculated, which weights the new update based on the covariance matrix of the states. Conceptually, this means that if the filter has converged and the states have a low covariance, the filter will ‘trust’ the current estimates and not give the update much weight. Thus, the Kalman filter effectively acts as an adaptive low-pass filter, allowing the filter to reject noisy measurements [Simon, 2006]. If the filter has not converged and the current states have a high covariance, the filter will be more optimistic about the new measurements. Either way, the weighted update is applied to generate the filter states for the next iteration and a new estimate for the state covariance matrix is calculated based on how well the prediction performed.

There are a few notes to be had on INS/GPS and the optimality of the Kalman filtering. The first is that the filter must be initialized with unbiased states since the Kalman filter has infinite memory and will propagate initial bias through the entire solution. Additionally, the covariance matrices for the system and measurements must also be accurate. These conditions have to be met for the Kalman filter to be an optimal estimator. In practice, however, the relatively poor quality of consumer-grade INS/GPS means that the initialization of the navigation system is less critical. Initialization for roll, pitch, position, and velocity is straightforward using

GPS and motionless observation of the gravity vector. However, the heading can't be initialized in an INS/GPS by direct measurement unless it is in motion or the INS is accurate enough to find the heading by measuring the earth's rotation of 15°/hour, a process known as gyrocompassing.

The MTi-G™ is augmented with a magnetometer, which by observing Earth's magnetic field is capable of providing heading observations and smooth the angular observations. However, a series of in situ experiments with the NOVA II revealed that the high electrical currents drawn by the electric motor induced magnetic fields that corrupted the MTi-G™ magnetometer measurements. An example of this effect is shown in Figure 3-1. Because of the error introduced by the electromagnetic interference, the magnetometer was disabled. Thus, the heading must be initialized by GPS updates alone. For this reason, it is critical that the NOVA II be in motion for some time to allow for a good estimation of the heading before data collection begins [Xsens MTi-G].

Sensor Synchronization

Synchronization is a challenging aspect of sensor integration when dealing with COTS devices. Since the INS/GPS sensors are already integrated within the MTi-G™ they were not of concern, however, the synchronization of the imaging system with the navigation system was an open problem. A thorough search of the marketplace did not reveal any COTS solution, and therefore the requirement for a completely modular off-the-shelf payload was not met. The solution was to develop a custom synchronization system, which was dubbed the ‘Burredo’. The synchronization architecture was developed by the author and the circuit and microcontroller program was designed and implemented by Joshua Childs.

Although the Burredo was designed specifically for the synchronization of a dSLR camera with an INS/GPS, the basic architecture of the Burredo allows for the synchronization of a wide range of sensors with minor modifications to the signal conditioning circuitry to handle the

voltage level. Cameras that employ SLR technology typically include a standard hotshoe connector, typically used to mount and synchronize flash devices. The flash synchronization signal present at the hotshoe is a ready-made interface for timing the exposure. A variety of flash signal modes are available, but the most common in modern xenon-type flash modules is the X-sync signal. The X-sync signal is designed to trigger the flash at the moment of peak exposure, i.e., at the moment the shutter is fully open [Olympus E-420]. Given the fast shutter speed relative to the dynamics of the UAV, the raw X-sync signal was used, although it does not precisely signal the central moment of exposure. Although adequate for our purposes, a platform with higher dynamics should include a correction factor for the time between when the shutter is fully open and half the exposure duration. This detail is discussed more thoroughly in Chapter 4. An important characteristic of the described synchronization architecture is the advantage of employing a feedback mechanism. The advantage of using a feedback mechanism, such as the flash X-sync signal, guarantees that the timing signal is deterministically related to the actual time of exposure.

The master timing signal is provided by MTi-GTM SyncOut pulse, which is synchronized (in the simultaneous sense) to the sampling rate of the navigation sensors. The internal clock of the MTi-GTM is calibrated to the GPS 1PPS signal. The MTi-GTM can be configured to output the solved navigation parameters at a variety of rates, such as 10, 50, and 100Hz, corresponding to frequency divisions of the GPS 1PPS signal. Choosing the sampling rate of the INS as the master signal was a matter of convenience in terms of hardware interface and has a very practical benefit. Each navigation packet received is accompanied by a Burredo timing packet. Additionally, each camera exposure that occurs within that epoch is reported as a fraction of the epoch. As a result, the synchronization data reported for the camera exposure is a proper fraction

that can be directly used to interpolate the needed direct georeferencing parameters in adjacent navigation packets.

The Burredo utilizes an Atmel, Inc.[®] Atmega[®] 644p processor to synchronize the devices and generate the timing packet. This processor series was chosen due to affordability and ease of development. The X-sync signal is conditioned using a high precision operational amplifier. The programming loop describing the operation of the timing mechanism is described in Figure 3-3. The master timing signal is at TTL voltage level. The Burredo outputs data in a fixed-width data packet over a TTL serial line. An FT232RL chip was used to convert this signal to the USB protocol, allowing for integration with the existing data bus.

To achieve its accuracy the Burredo utilizes the Atmega[®]'s 16 bit input capture register. This allows the slave event time to be recorded asynchronously of the normal program scheduling. The resolution of this timer is 67 ns, dependent on the microcontroller's clock frequency which is implemented at 16.7456 MHz. To further reduce the weight of the overall payload, a second FT232RL chip and a line driver have been added to reduce cabling and packaging requirements. It allows the computer to communicate with the MTi-GTM using USB, and simplifies wiring by having the master timing signal present on the same board. This saves weight and space.

Payload Control and Data Management

Hardware

The control and data management requirements of the NOVA II payload strongly suggested the use of a Microsoft Windows[™] compatible x86-based computer. Such a computer meets many of the payload requirements: readily available components such as human interface devices and storage devices; standardized data buses such as FireWire, USB, SATA II, and RS-

232. Perhaps most importantly, there is a very large market for devices with drivers that are plug-and-play compatible.

The payload control and data management system was built around a VIA Technologies, Inc.[®] Pico-ITX form factor motherboard, the EPIA™ P700-10L [VIA EPIA, 2009]. The data storage device selected was a solid state hard drive connected by SATA, optimal for UAV operations because it has no delicate moving parts. Appropriate interface connectors were wired for the power supply, power switch, power-on indicator light, USB 2.0, RS-232, and VGA. The power supply itself was a Dimension Engineering, Inc.[®] DC-DC regulator, model DE-SWADJ3, that down-regulated the onboard lithium polymer battery voltage from a nominal 18.5 V to the required 12 V level.

Early in the NOVA II testing phase, it was apparent that the onboard computer was a major source of electromagnetic interference which debilitated the radio communications downlink. As a result, it was necessary to shield the computer within a Faraday cage. An 18 gauge steel mesh was used to construct a structurally sound enclosure with satisfactory electromagnetic shielding properties. All devices, cabling, and interconnects with high-frequency signals were carefully shielded and properly grounded based on early testing.

Software

The payload control and data management software, titled the “NOVA II Payload Manager”, was written by the author in Microsoft[®] C#.NET and runs on the Microsoft Windows XP™ operating system. The software also makes use of proprietary dynamic link libraries provided by Olympus USA, Inc.[®] as an interface to the camera. The software has a fully object-oriented paradigm and makes extensive use of interrupt-driven events to minimize device querying overhead. The NOVA II Payload Manager software has the following objectives:

- Reliably startup and begin payload management automatically

- Simultaneously expose local GUI and remote interfaces to control the payload
- Configure settings, trigger exposures, and store images from the camera
- Configure and log data from the IMU/GPS
- Log data from the synchronization device
- Integrate data streams into efficient disk-write operations

The basic structure of the program consists of a Windows™ Form object, which instantiates a single instance of a **NovaOrchestrator** object, which in turn creates instances of the **Logger**, **Procerus**, **Olympus**, **MTiG**, and **Burredo**. These objects are instances for the control of the data logger, the GCS downlink for remote commands, the INS/GPS navigation device, and the synchronization device respectively.

Two critical aspects of the software architecture are the logging subsystem and the event-driven data collection model. First, the logging subsystem is built around a thread safe singleton class. This allows all of the device handlers to have equal access to the same logging system, allowing efficient write operations to the hard drive. This, together with the event-driven device handlers, allows the incoming data to be recorded precisely in the sequence received. This system is necessary for the correct implementation of the synchronization scheme.

In addition to these architectural concerns, there were issues associated with allowing simultaneous command of the payload from both remotely transmitted commands as well as the automated routines. This functionality is provided by implementing command marshal methods with state flags in the **NovaOrchestrator** object. Although an interface between the payload computer and the Procerus Technologies, Inc.® Kestrel™ autopilot system which provides the wireless communication facilities was not implemented, the software was written to allow future integration once this communication link is established.

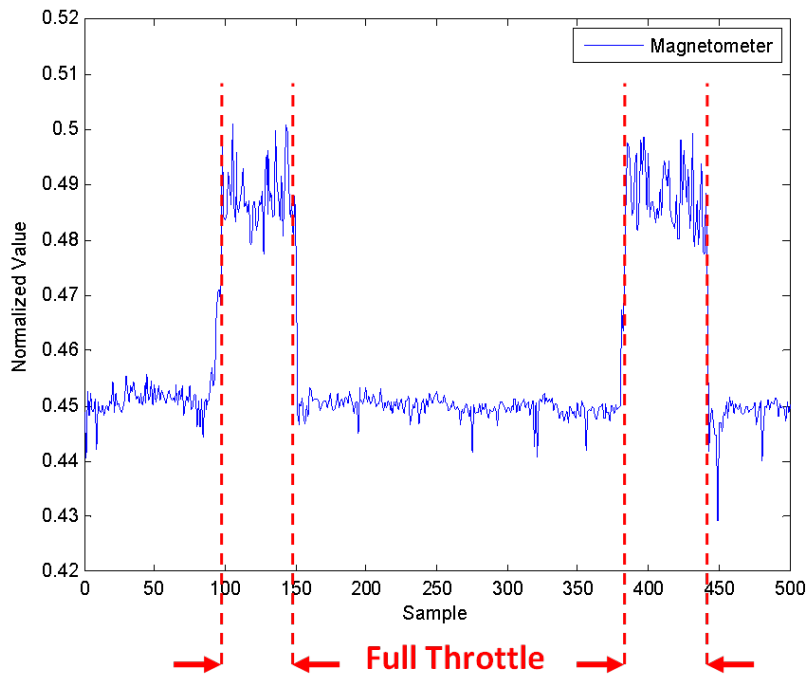


Figure 3-1. The effect of throttling up the NOVA II electric motor on the payload magnetometer at full throttle (70 amp draw)

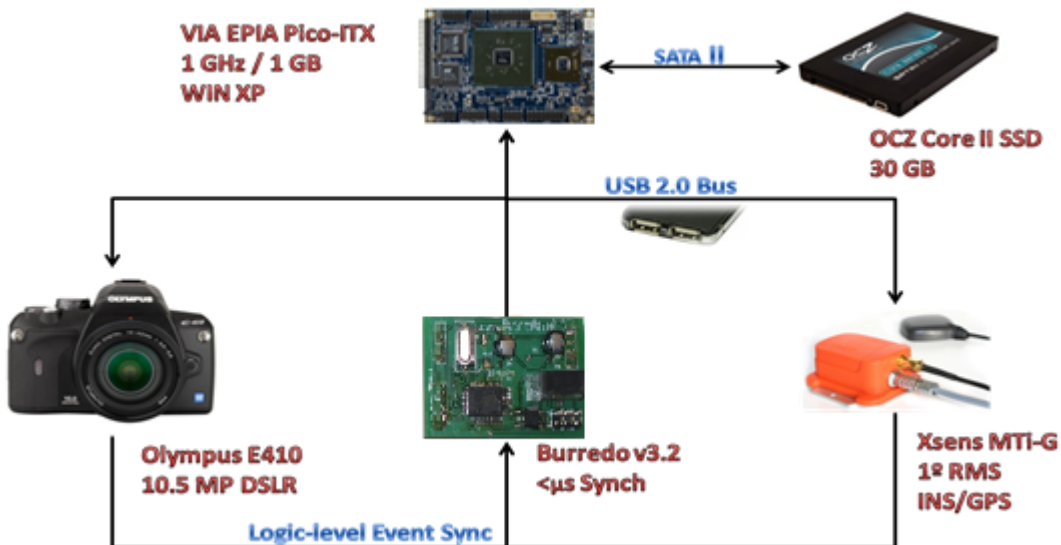


Figure 3-2. Architecture of the NOVA II Payload

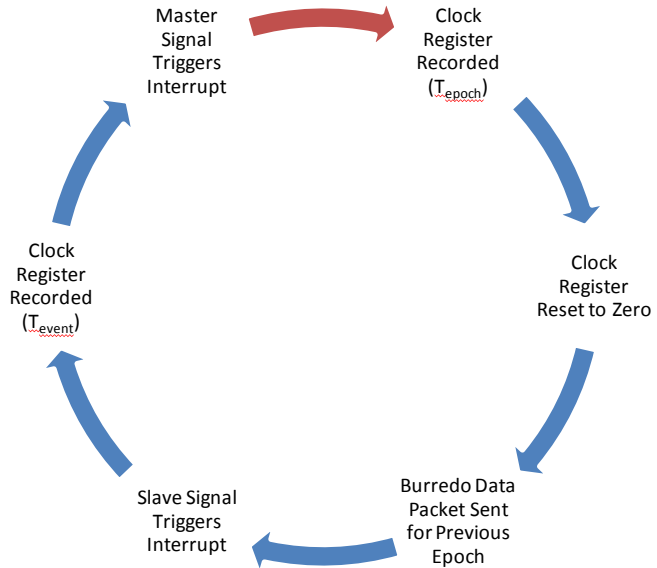


Figure 3-3. Diagram of the Burredo's operation

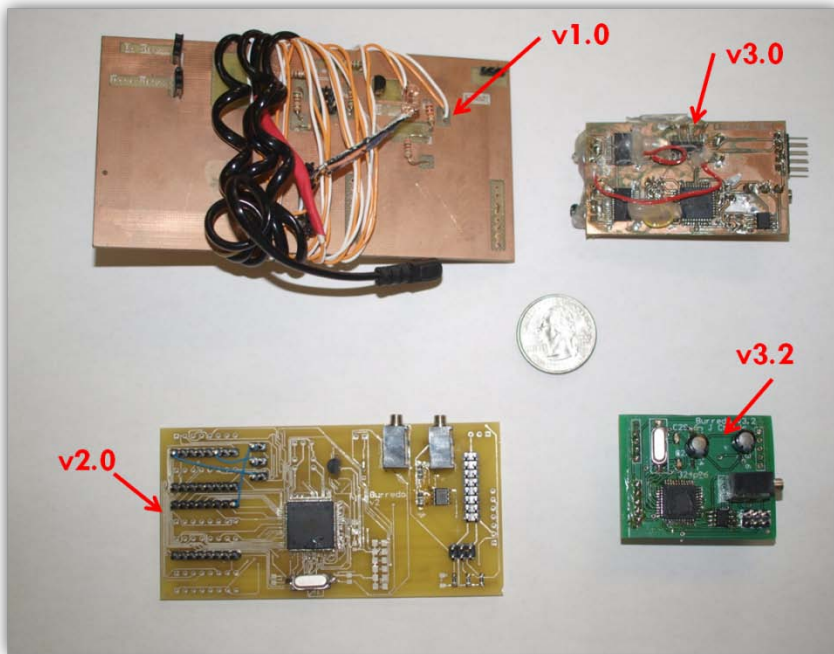


Figure 3-4. Comparison of the Burredo's size through iterations of development



Figure 3-5. Preparing to load the payload into the NOVA II, arranged beside the plane in their approximate locations inside the airframe

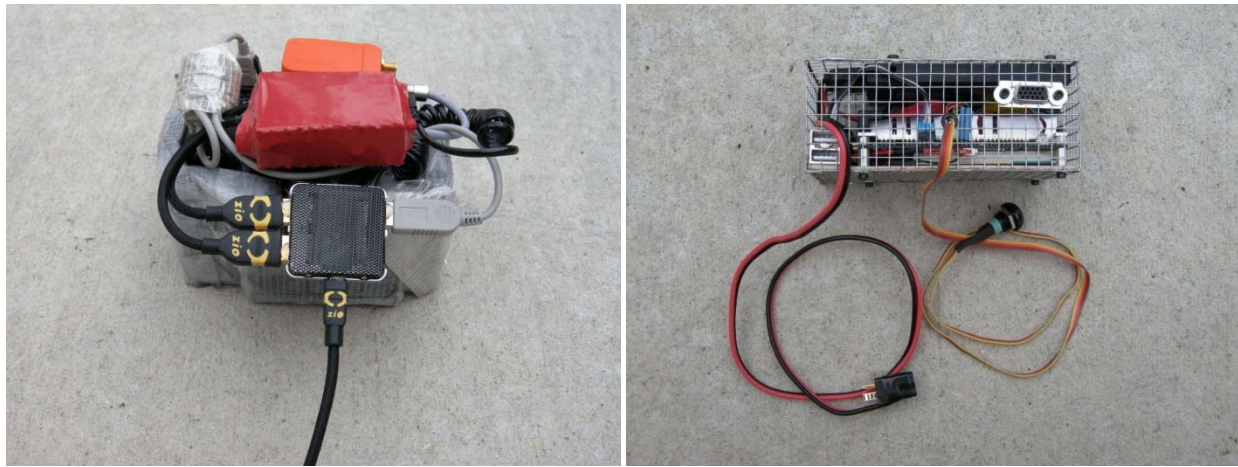


Figure 3-6. Close-ups of the sensor package (left) and controller package (right)

CHAPTER 4

PAYOUTLOAD CALIBRATION AND EVALUATION

Camera Calibration

A camera calibration was performed using data collected at the Lightning Lab Calibration Site (see Appendix B). This calibration is marked by being an in-situ calibration as opposed to a bench calibration as performed on previous generations of the NOVA platform; see [Bowman, 2008], for example. The literature strongly suggests the use of in-situ camera calibration, particularly for non-metric cameras [Habib et al., 2005; Honkaavara et al., 2003]. In situ allows the calibration to include actual geometry, temperature, pressure, and other conditions found during normal operational missions. The camera is also focused at infinity during normal data collection; a condition which is not practically achieved when calibrating the camera using close-range techniques. The calibration data presented was collected on February 2, 2009 at midday and at a flying height of 200 meters with an average groundspeed of 21 m/s. The camera was configured for shutter priority with exposure duration of 1/2000th and with all images taken at a 2.8 F-stop.

The field calibration technique as performed in this section is admittedly inconvenient compared to close range calibration approaches. Considering that the UAV is designed to operate in remote areas without ground control, it is counter-intuitive to expect there to be a calibration site available nearby. Thus, a primary concern was to determine the frequency with which the camera calibration must be performed. If it is found that the calibration parameters change significantly from one mission to the next, then the proposed in-situ calibration would not be practical and less accurate but more convenient close-range techniques would be preferable.

Varying results as to the stability of internal orientation parameters for non-metric digital cameras have been obtained in the literature, and it is unclear whether this is due to methodology

or the camera employed. In Habib, et. al. [2005], the issue of calibration methodology is addressed directly, and a conservative approach for estimating IOP similarity was developed that considered the effect of IOP stability on direct georeferencing without any post-mission adjustment. Using this method, the interior orientation parameters were found to exhibit significant variability. However, a more liberal stability assessment that accounted for using a bundle adjustment with ground control on the same data as the conservative approach showed that in fact the interior orientation parameters did not vary significantly. Using a similar approach as the more liberal stability assessment in Habib, et. al. [2005], no significant variability was found for a lower-grade consumer camera over the course of a year [Wackrow, 2008].

If the parameters are unstable, an alternative approach would be to conduct a self calibrating bundle adjustment for each flight using the photogrammetric data generated by the proposed direct georeferencing technique. Given that such flight data would not include ground control points and would rely on a low-accuracy navigation system for control, it is unclear whether the signal-to-noise ratio would obliterate the sensitive interior orientation parameters. In addition, it has been well-demonstrated that the interior orientation parameters are strongly correlated with various exterior orientation parameters using normal adjustment geometries [Wolf and Dewitt, 2000]. The effect of absorbing biases in the direct georeferencing parameters and perhaps even noise for higher-order distortion parameters on the overall adjustment accuracy is not clear for the technique presented in this thesis. In calibrating a high-accuracy direct georeferencing payload, it was shown that using the in-plane polynomial parameters developed by Ebner [1976] reduced the mixing of the exterior and interior orientation parameters [Cramer, 2002].

The results of the camera calibration are presented in Table 4-1. The self-calibrated bundle adjustment was performed using SCBUN [Wolf and Dewitt, 2000]. The IOPs described in Chapter 2, excluding affine distortion parameters, were modeled. The standard deviation of unit weight of the solution was 1.06. The images used and their adjusted exterior orientation parameters are given in Table 4-2. Interestingly, the principal point offset parameters are not statistically significant at the 95% confidence level. On the other hand, the first-order radial and tangential distortion parameters are both significant, the former strongly so. Such a result is not unexpected for a non-metric camera lens.

Boresight and Leverarm Calibration

Along with synchronization, the boresight and leverarm calibration has been noted as one of the fundamental problems in DGRS [Skaloud, 1999]. While it is at least feasible to directly measure the leverarm on a fixed platform to a suitable degree of accuracy, analytical methods are almost certainly required to obtain the boresight correction for non-metric cameras [Cramer, 2002]. In the NOVA I approach, the boresight parameter was recovered by mounting the system to a platform with a known orientation and solving for the camera orientation by using a computer vision algorithm [Bowman, 2008]. The drawback of this approach is that it is not particularly rigorous and a more robust analytical approach is possible.

Unlike the IOPs, the boresight and leverarm corrections are unlikely to be significantly variable due to the rigidity of the strapdown payload configuration in comparison to the accuracy of the implemented INS/GPS. Using high accuracy platforms some variability the boresight and leverarm parameters have been observed, but it is well below the expected precision of the NOVA II [Honkavaara, 2003; Cramer, 2002]. Unlike nearly every other aspect of direct georeferencing, the boresight and leverarm calibration explicitly relies on the availability of ground control points, a motivating factor in establishing the Lightning Lab Calibration Site (see

Appendix B). Given that an aerotriangulation calculation must be performed anyway, it has been noted that the simultaneous bundle adjustment can be extended to include the boresight and leverarm parameters in a simultaneous solution. Caution is advised given the strong correlation of the boresight and leverarm parameters with the IOPs when using the self-calibrating bundle adjustment [Cramer, 2002].

The technique presented here for boresight and leverarm calibration is independent of the bundle adjustment to avoid mixing of parameters. Thus, it is assumed that a calibration data set is obtained which has a suitable number of corresponding navigation and EOPs recovered by calibrated aerotriangulation. All that remains is to apply an optimal estimation to Equation 2-15 parameterized by linear offset and Euler angles, reformulated here as observation equations in Equation 4-1.

$$\begin{aligned} \begin{bmatrix} X_{LA} \\ Y_{LA} \\ Z_{LA} \end{bmatrix} &= R_N^{-1} \begin{bmatrix} \Delta X \\ \Delta Y \\ \Delta Z \end{bmatrix} \\ R_B &= R_I R_N^T \\ \begin{bmatrix} \Delta X \\ \Delta Y \\ \Delta Z \end{bmatrix} &= \begin{bmatrix} X_L \\ Y_L \\ Z_L \end{bmatrix} - \begin{bmatrix} X_N \\ Y_N \\ Z_N \end{bmatrix} \end{aligned} \tag{4-1}$$

A least squares solution to the leverarm observation Equation 4-1 is linear and reduces to the weighted means of observations, given Equation 4-2. The weighting factor W_{LA} in Equation 4-2 requires the application of the law of propagation of variances to rotation matrices, developed later in this section.

$$\hat{X}_{LA} = \frac{\sum W_{LA} R_N^{-1} [\Delta X, \Delta Y, \Delta Z]^T}{\sum W_{LA}} \tag{4-2}$$

It is important to note that the DCM representation of R_b has intrinsic orthonormality constraints due to the trigonometric relationship of its elements to the Euler angles. It is therefore necessary to parameterize the least squares solution with respect to these Euler angles, enforcing the orthonormality conditions. The alternative of parameterization with respect to the elements of the rotation matrix will generally not produce a proper rotation matrix in the presence of noise. Linearization with respect to the Euler angles produces nine redundant equations as given in a reduced form in Equation 4-3. The linearized least squares formulation requires iterative solution of the weighted normal equations given in Equation 4-5 and requires initial approximations.

$$\left(\frac{\partial R_b}{\partial \omega_B} \right)_0 d\omega_B + \left(\frac{\partial R_b}{\partial \phi_B} \right)_0 d\phi_B + \left(\frac{\partial R_b}{\partial \kappa_B} \right)_0 d\kappa_B = R_I R_N^T - R_{b0} + v_{3 \times 3} \quad (4-3)$$

$$W_B J X = W_B K$$

$$X = \begin{bmatrix} d\omega_B \\ d\phi_B \\ d\kappa_B \end{bmatrix}$$

$$J = \begin{bmatrix} a_1 & a_2 & a_3 & a_4 & a_5 & a_6 & a_7 & a_8 & a_9 \end{bmatrix}^T$$

$$K = \begin{bmatrix} m_{11}n_{11} + m_{12}n_{12} + m_{13}n_{13} - \cos \phi_B \cos \kappa_B \\ m_{11}n_{21} + m_{12}n_{22} + m_{13}n_{23} - \sin \omega_B \sin \phi_B \cos \kappa_B - \cos \omega_B \sin \kappa_B \\ m_{11}n_{31} + m_{12}n_{32} + m_{13}n_{33} + \cos \omega_B \sin \phi_B \cos \kappa_B - \sin \omega_B \sin \kappa_B \\ m_{21}n_{11} + m_{22}n_{12} + m_{23}n_{13} + \cos \phi_B \sin \kappa_B \\ m_{21}n_{21} + m_{22}n_{22} + m_{23}n_{23} + \sin \omega_B \sin \phi_B \sin \kappa_B - \cos \omega_B \cos \kappa_B \\ m_{21}n_{31} + m_{22}n_{32} + m_{23}n_{33} - \cos \omega_B \sin \phi_B \sin \kappa_B - \sin \omega_B \cos \kappa_B \\ m_{31}n_{11} + m_{32}n_{12} + m_{33}n_{13} - \sin \phi_B \\ m_{31}n_{21} + m_{32}n_{22} + m_{33}n_{23} + \sin \omega_B \cos \phi_B \\ m_{31}n_{31} + m_{32}n_{32} + m_{33}n_{33} - \cos \omega_B \cos \phi_B \end{bmatrix}$$

$$a_1 = 0$$

$$a_2 = \cos \omega_B \sin \phi_B \cos \kappa_B - \sin \omega_B \sin \kappa_B$$

$$a_3 = \sin \omega_B \sin \phi_B \cos \kappa_B + \cos \omega_B \sin \kappa_B$$

$$a_4 = 0$$

$$a_5 = -\cos \omega_B \sin \phi_B \sin \kappa_B - \sin \omega_B \cos \kappa_B$$

$$a_6 = -\sin \omega_B \sin \phi_B \sin \kappa_B + \cos \omega_B \cos \kappa_B$$

$$\begin{aligned}
a_7 &= 0 \\
a_8 &= -\cos \omega_B \cos \phi_B \\
a_9 &= -\sin \omega_B \cos \phi_B \\
b_1 &= -\sin \phi_B \cos \kappa_B \\
b_2 &= \sin \omega_B \cos \phi_B \cos \kappa_B \\
b_3 &= -\cos \omega_B \cos \phi_B \cos \kappa_B \\
b_4 &= \sin \phi_B \sin \kappa_B \\
b_5 &= -\sin \omega_B \cos \phi_B \sin \kappa_B \\
b_6 &= \cos \omega_B \cos \phi_B \sin \kappa_B \\
b_7 &= \cos \phi_B \\
b_8 &= \sin \omega_B \sin \phi_B \\
b_9 &= -\cos \omega_B \sin \phi_B \\
c_1 &= -\cos \phi_B \sin \kappa_B \\
c_2 &= -\sin \omega_B \sin \phi_B \sin \kappa_B + \cos \omega_B \cos \kappa_B \\
c_3 &= \cos \omega_B \sin \phi_B \sin \kappa_B + \sin \omega_B \cos \kappa_B \\
c_4 &= -\cos \phi_B \cos \kappa_B \\
c_5 &= -\sin \omega_B \sin \phi_B \cos \kappa_B - \cos \omega_B \sin \kappa_B \\
c_6 &= \cos \omega_B \sin \phi_B \cos \kappa_B - \sin \omega_B \sin \kappa_B \\
c_7 &= 0 \\
c_8 &= 0 \\
c_9 &= 0
\end{aligned}$$

$$R_I = \begin{bmatrix} m_{11} & m_{12} & m_{13} \\ m_{21} & m_{22} & m_{23} \\ m_{31} & m_{32} & m_{33} \end{bmatrix}$$

$$R_N = \begin{bmatrix} n_{11} & n_{12} & n_{13} \\ n_{21} & n_{22} & n_{23} \\ n_{31} & n_{32} & n_{33} \end{bmatrix}$$

$$R_B = \begin{bmatrix} \cos \phi_B \cos \kappa_B & \sin \omega_B \sin \phi_B \cos \kappa_B + \cos \omega_B \sin \kappa_B & -\cos \omega_B \sin \phi_B \cos \kappa_B + \sin \omega_B \sin \kappa_B \\ -\cos \phi_B \sin \kappa_B & -\sin \omega_B \sin \phi_B \sin \kappa_B + \cos \omega_B \cos \kappa_B & \cos \omega_B \sin \phi_B \sin \kappa_B + \sin \omega_B \cos \kappa_B \\ \sin \phi_B & -\sin \omega_B \cos \phi_B & \cos \omega_B \cos \phi_B \end{bmatrix} \quad (4-4)$$

$$X = (J^T W_B J)^{-1} J^T W_B K \quad (4-5)$$

For both the boresight and leverarm calibration, it is necessary to properly weight the observations using W_B and W_{LA} respectively to produce an optimal estimation of the parameters. Unfortunately, the nonlinearity of the propagation of error in Euler angle parameters through the DCM formulation results in very dense weight matrix calculations. The calculation of these matrices is best handled through computerized symbolic algebra programs. Therefore, the

process to construct them is merely described here and not illustrated. From the general law of propagation of variances, we can write a general weighting matrix for the corresponding weight matrix, given by Equation 4-6.

$$W = \sigma_0^2 (A \Sigma A^T)^2$$

$$A = \begin{bmatrix} J_1(x_1, \dots, x_m) \\ \vdots \\ J_n(x_1, \dots, x_m) \end{bmatrix}$$

$$\Sigma = \begin{bmatrix} \sigma_{x_1}^2 & \cdots & \sigma_{x_1 x_m} \\ \vdots & \ddots & \vdots \\ \sigma_{x_m x_1} & \cdots & \sigma_{x_m}^2 \end{bmatrix}$$

σ_0^2 = standard deviation of unit weight

$J_n(x_1, \dots, x_m)$ = Jacobian of the n^{th} function w.r.t. to m unknowns

Σ = covariance matrix of the Euler angle observations

(4-6)

To construct W_B , the Jacobian of the boresight equation in Equation 4-1 must be evaluated with respect to $\omega_I, \phi_I, \kappa_I, \theta_N, \phi_N$, and ψ_N for each observation. The weight matrix is then constructed using Equation 4-6. Similarly, the Jacobian of the leverarm must be evaluated with respect to $\theta_N, \phi_N, \psi_N, X_I, Y_I, Z_I, X_N, Y_N$, and Z_N and the weight matrix constructed.

For the boresight observations, the a posteriori statistics of the AT bundle adjustment should provide the covariance estimate for the Euler angles of R_I, X_I, Y_I , and Z_I . Equivalent statistics should be available for $\theta_N, \phi_N, \psi_N, X_N, Y_N$, and Z_N from the Kalman filter for the navigation system. If these are not available for the navigation system, it may be possible to obtain estimates by benchmarking the navigation system against a more accurate one. Particularly in the case of rotations, off-diagonal covariance terms can be significant and should not be assumed to be zero.

A boresight calibration was conducted using the method described above using the assessment data described in more detail in Chapter 7. It should be noted that because this boresight calibration was conducted using data that did not have ground control, the boresight calibration may be tainted by biases present in the bundle adjustment. Although the above weighting scheme was employed, a priori estimates of the accuracy were not available and so an equal weighting scheme was used. However, even in this state, it serves to demonstrate a proof-of-concept. Because the navigation system is installed on the aircraft within 2 cm of the imaging system, the leverarm calibration can be solved with sufficient accuracy by direct measurement given the relatively poor precision of the navigation system. The results of the example boresight calibration are presented in Table 4-3.

Navigation Accuracy

The accuracy of the navigation system is a critical factor in the success of a directly georeferenced remote sensing system. The values generated by the navigation system, particularly the GPS positioning, serve as the control for the photogrammetric solution. By fusing the navigation parameters with the photogrammetric observations, the accuracy of the INS orientation solution becomes perhaps less critical, but of sufficient accuracy to obtain good initial approximations for the bundle adjustment. To this end, the accuracy of the MTi-G™ was analyzed by benchmarking it against a tactical-grade Novatel, Inc.® HG1700® 1°/hr navigation system integrated with an OEMV4 differential GPS receiver..

This benchmarking exercise produced an unexpectedly poor and therefore much more interesting result. These results generated should not be considered representative of the performance of the navigation system since the error profile observed has never been repeated and the root causes are unclear. This experiment was simultaneously conducted with the test of another geodetic grade dual-frequency DGPS to evaluate its performance under GPS dropout

conditions due to forest canopy cover. It is therefore exceedingly probable that the MTi-GTM was experiencing significant multipath error or GPS dropout. The published accuracy of the MTi-GTM is given as less than 0.5 degrees in tilt and 1.0 degree in heading for static observations and 1.0 degree RMS orientation error under dynamics, with a positional CEP of 2.5 m [Xsens MTI-G].

These specifications are given with the appropriate caveat that the accuracy results are dependent on the Kalman filter scenario selected. As described in Chapter 3, there are augmenting sensors such as a magnetometer and barometer, as well as non-holonomic constraints which can be included in the navigation filter to improve the performance. In the interest of reflecting the performance attainable by the NOVA II, all augmenting sensors and constraints were disabled for this accuracy assessment. A length initialization period of both static and dynamic observations to allow the filter to stabilize was conducted directly before the start of the data collection during a ZUPT of the HG1700[®] over a known control point.

The results of the both the static and dynamic portions of the experiment are given in Table 4-4. The data collection transitioned directly from the static portion to the dynamic portion without a gap. The results of the static portion were not unexpected; the roll and pitch error are somewhat high but not outside a reasonable range given the lack of augmentation. The GPS positions were also acceptable. The heading error, however, was unexpectedly large and drifts during the static test as expected when heading updates are only available by GPS observations. It is unclear whether this initial large error was due to poor initialization, perhaps due to the aforementioned sky obstructions, or whether this is within the range of the typical heading error when using GPS-only updates. A heading error of similar magnitude had been previously noted in the DGRS data sets over known control points, so it is not out of the question.

The most surprising result from this data set was the extremely poor performance of the GPS position solution during the dynamic portion of the test. The roll and pitch estimates performed admirably, converging on the HG-1700® solution within about a 40 s. The roll error was slightly higher than the pitch dynamics, likely due to larger dynamics about that axis because it was a ground-based vehicle. The GPS solution, however, was terrible, with rapidly diverging error nearly reaching 50 m on a single axis. The most reasonable explanation for this behavior was that the GPS lost lock in the transition from the static to the dynamic portions of the data collection. Coinciding with this peak in positioning error, the vehicle made an abrupt turn which resulted in a nearly instantaneous jump in the heading error, must likely caused by the lag of GPS updates. However, the GPS error began a steep decline, probably as it regained lock given the reduced canopy coverage over the road.

This accuracy assessment was revealing for a number of reasons. The first was that the MTi-G™ performs no better than other low-accuracy INS systems when the GPS updates are poor or unavailable; the divergence in position was rapid. Fortunately, GPS dropout conditions are not expect on the NOVA II because the GPS was mounted on the airframe with a clear view of the sky, and the roll- and pitch-limiting autopilot prevent serious horizon occlusion by the airframe. Both the pitch and roll parameters performed well, reliably giving estimates within 2 degrees RMS even under these worst-case conditions. The heading was not as reliable as expected, but this may be explained by the possible GPS reception problems. Undoubtedly, better GPS reception and stable dynamics would improve the quality of all results. Finally, the vertical error was decent and was largely composed of bias error that slowly drifted.

Synchronization Accuracy

Recalling that sensor integration for DGRS requires establishing both the spatial and temporal relationship between the sensors, and having established the accuracy of the spatial

component by boresight and leverarm calibration, it remains that the temporal relationship between the sensor observations be considered. The importance of synchronization in direct georeferencing has been well established [Skaloud and Legat, 2007], and a number of system integration techniques have been developed. The NOVA I employed a rudiment synchronization scheme which relied on the time of arrival of navigation data packets at the host and camera trigger commands, reported to have an accuracy of 87 ms [Bowman, 2008]. An identical implementation using the same hardware showed that the synchronization error was as much as 333ms [Chao et al., 2008]. This method highlights the need for deterministic measures of the time of sensor sampling. Relying on data packets introduces a stochastic component due to both the processing and transmission time of the packet in the INS, as well as a stochastic element from using software-based synchronization on a non-real-time operating system. Particularly for COTS consumer cameras, features such as white balancing and autofocus can produce stochastic and even indeterminant delays between trigger and exposure. Without a feedback mechanism, this error can't be compensated for. A more rigorous approach commonly implemented is the use of a COTS DAQ or similar expansion card in the host computer, which allows deterministic timing of the signals. However, a DAQ card is impractical on a small UAV platform due to its size and lack of an available interface with the host computer. Nonetheless, using this approach has been shown to obtain accuracies ranging from 0.4 ms [Li et al., 2006] to 5 μ s [Toth et al., 2008].

Time synchronization problems can be described in terms of synchronizing an arbitrary ‘slave’ timing signal to a periodic ‘master’ timing signal. This relationship arises from the idea that synchronization of any pair of sensors necessitates the establishment of a temporal reference, which for convenience is typically chosen as the periodic signal. Often, the choice of master

timing signal is evident from the nature and temporal stability of the sensors. It is intuitive in the case of a DGRS that the master signal be based on the GPS 1PPS signal and that the slave signal is the time of exposure of the imaging system, since GPS time is referenced to the standard UTC system. This system conveniently provides the time of exposure in a standard temporal reference system. However, it should be noted that this terminology is purely one of convenience, and that a system where GPS observations are instead synchronized relative to the exposures of a camera is equally valid, if not as sensible. Moreover, the master signal need not be purely periodic; given any two occurrences of a master timing signal, one can define an epoch of time, and the occurrence of a slave signal be synchronized in terms of a proportion of the master-defined epoch.

Each timing signal is generated by an event, e.g. the exposure of a camera sensor or validation of a GPS message, and is subject to an aperture error. The aperture error is defined as the error in synchronization introduced by characterizing an event of finite duration with a timing impulse [Bendat, 2000]. A pertinent example of aperture error is in characterizing the time of exposure of an imaging system, which may on a typical imaging system range from 1/100 to 1/8000th of a second. This begs the question, should the instantaneous timing signal for the exposure event occur at the beginning, end, or at some proportion of the total time which the shutter is open? This question leads to observations regarding the necessary accuracy required of a synchronization system.

Aperture error is closely related to synchronization error due to the dynamics of the system being observed. It is evident that if neither the camera nor the scene is in motion, then whether one defines the moment of exposure at the beginning, middle, or end of the time the shutter is open is irrelevant. Expounding on the purpose of direct georeferencing, the goal is to provide the

parameters of a geometric model which produced the observed image. Thus, the dynamics of the system of interest is the change in the observed image with respect to a change in position and orientation parameters. In the case of DGRS, this relationship is defined by the perspective projective geometry of a camera, and a full derivation is beyond the scope of this thesis. The key understanding, however, is that the accuracy of the system is necessarily limited by the aperture error of the sensors.

To clarify, consider a camera mounted vertically with a shutter speed of 0.25 ms and a nominal focal length of 5000 pixels flying 25 m/s straight and level at 100 meters above ground. In this scenario, the camera will move a linear distance of 6.25 mm while the shutter is open. When motionless, one pixel at the center of the image covers a ground distance of 2 cm in the direction of travel. Due to the dynamics over the exposure duration, the linear distance that the center pixel actually covers is 26.25 mm. Such an image in practice shows no visible image blurring, which indicates that the error due to dynamics is negligible for our purposes. The selection of the parameters in this scenario is not by accident; the shutter speed of the camera is selected based on experiments to eliminate blurring due to what is effectively the aperture error from typical small UAV dynamics.

Having made the somewhat weak assumption that dynamics are negligible for an appropriate shutter speed, one can deduce that the accuracy of the synchronization must be within the magnitude of the exposure duration. A stronger assumption that the dynamics are linear over the duration of exposure implies that synchronization error is minimized by taking the average parameter value over the period of exposure, equivalent to defining the synchronization signal at the center of the duration of exposure. Hence, there is a need for the bias correction between the X-sync signal and the central moment of exposure on higher-dynamics platforms. A

more general approach would be to take the time-weighted average of the parameters over the exposure duration, a case which is only practical (and it's not) where the frequency of the navigation parameter data is much greater than the shutter speed.

In the preceding discussion of synchronization accuracy, the emphasis was on understanding when the synchronization signal is generated in relation to each event of finite duration, and thereby minimizing the aperture error. This is significantly different from considering synchronization error from the standpoint of the accuracy of measuring the relative timing of the master and slave signals. As will be seen in the subsequent analysis, this is because the precision of measuring the relative timing of two signals is orders of magnitude better than the time scale of the aperture error on a typical DGRS. The error due to synchronization is thus diminishingly small relative to the other errors inherent in the described DGRS. However, the analysis of synchronization error is relevant to other types of sensors and payload configurations, particularly laser ranging, and in these it is possible that such synchronization errors will become significant.

The synchronization accuracy of the Burredo was evaluated by comparing its performance to a Trimble AcuTime® Gold GPS receiver. The AcuTime® outputs the GPS 1PPS signal with an accuracy of ± 15 ns and has two event inputs which provide an event timestamp in UTC time with a resolution of 488 ns [Acutime, 2007]. In the experiment, the GPS 1PPS signal from the AcuTime® was the master signal for the Burredo, and a microcontroller-based circuit generated a pseudorandom trigger signal, $T_{trigger}$, for both AcuTime® event input and the Burredo slave input. The signal propagation delay due to cable length introduced an additional parameter, ΔT_{prop} , into the experimental setup, and was calculated to be 120 ns for the AcuTime® cable length of 100 feet. All other propagation delays were negligible due to short cable lengths. The

primary data set was collected over a period of about 6 hours, with a trigger event occurring on average every 2.5 s. Several smaller confirmation data sets were also collected, all showing similar results.

Each timing epoch was defined as the time between the beginning of the UTC second, T_0 , and the end of the second, T_{epoch} . Thus, each event measurement can be defined as a fraction of the UTC second. The measurements were modeled using Equation 4-7 and Equation 4-8 for the AcuTime® and Burredo, respectively. The AcuTime® measurement was taken as the truth value to benchmark the Burredo, thus the observation equation was defined by Equation 4-9.

$$T_{AcuTime} = T_A = \frac{(T_{trigger} + \Delta T_{prop}) - T_0}{T_{epoch} - T_0} \quad (4-7)$$

$$T_{Burredo} = T_B = \frac{T_{trigger} - (T_0 + \Delta T_{prop})}{(T_{epoch} + \Delta T_{prop}) - (T_0 + \Delta T_{prop})} \quad (4-8)$$

$$\epsilon = T_A - T_B = \frac{2\Delta T_{prop}}{T_{epoch} - T_0} + v_e \quad (4-9)$$

Note the Burredo measures all of these values with respect to integer clock cycles, with a clock rate of approximately 14.7456 MHz. Both measurements are effectively ratios of equivalent units, so all units cancel. Because we have defined the epoch as equal to the UTC second, the measurements are effectively in fractions of a second, however the experiment would be equally valid for an arbitrary master signal.

Due to the design of this experiment, it was necessary to apply experimental bias corrections. The most significant adjustment is due to quantization error, which was significant for the Trimble device. The AcuTime® resolution is specified at 488 nanoseconds, and due to the documented sequence of events this error always results in a ‘late’ measurement. A timestamp generated by the Trimble device indicates an event takes place within the *previous* 488 ns [Acutime, 2007]. Assuming a uniform distribution of event times, this indicates the mean

timestamp is generated 244 ns after the actual event. Not by accident, the pseudorandom triggers generated for the experiment resulted in an approximately uniform distribution of measurement values over the fraction of the 1PPS epoch, as shown in Figure 4-4.

Unexpectedly, strong correlation between the fraction of the epoch and the magnitude of the error emerged from the data, as shown in Figure 4-5. Upon further investigation, it was found that the error correlation is explained by a constant bias in the measurement of T_0 in the Burredo caused by the finite time required to retrieve and store the value of the clock register before resetting it at the beginning of each epoch. This error does not occur during the event capture since it is handled by hardware. The reset time, denoted ΔT_{reset} , modifies the Burredo's measurement equation as given in Equation 4-10. Since the Burredo operates on integer clock cycles, this value was found by minimizing the correlation and rounding to the nearest integer value, so that $\Delta T_{reset} = 11$, as shown in Figure 4-6.

$$T_B = \frac{T_{trigger} - (T_0 + \Delta T_{reset} + \Delta T_{prop})}{(T_{epoch\ h} + \Delta T_{prop}) - (T_0 + \Delta T_{reset} + \Delta T_{prop})} \quad (4-10)$$

The synchronization error in the Burredo (Figure 4-7), corrected for the experimental biases and Δt_{reset} , was found to be non-normal (Figure 4-8), rejecting the null hypothesis that the distribution is normal at the 95% confidence level by the Lilliefors test. This result was expected, since a digital system will not be susceptible to large outliers. In Figure 4-9, the oscillator frequency drift for the Burredo is clearly visible. Both low and high rates of change of the oscillator frequency are observed. Additionally, the synchronization error was found to not be correlated to variations in the crystal frequency.

After removing all experimental biases previously mentioned, the resulting mean error between the Trimble and Burredo measurements was 208.9 ns. The bias corresponds to approximately three clock cycles of the Burredo. The actual source of this bias error is unclear,

and may be due to a number of factors including the internal architecture of the Burredo's microprocessor timing facilities or the timing signal line drivers. Without experimental verification of the source of this bias, whether intrinsic to the device or due to experimental setup, the error may not be excluded from a conservative error analysis and is therefore attributed to the Burredo, resulting in a experimental RMS error of 256.4 nanoseconds, a significant improvement over any DGRS synchronization system found in the literature.

The measurements of both the Burredo and AcuTime® are subject to quantization error. The standard deviation of error introduced by quantization (Equation 4-11) was used to calculate the Burredo and AcuTime® quantization error. Applying the special law of propagation of variances for two independently measured quantities, the calculated deviation of the synchronization error due to quantization is given by Equation 4-12.

$$\sigma_x = \sqrt{\frac{1}{12} \Delta x} \quad (4-11)$$

$$\begin{aligned} \sigma_B &= \pm 19.6 \text{ ns} \\ \sigma_A &= \pm 140.9 \text{ ns} \\ F(x) &= \epsilon = T_A - T_B \\ \sigma_\epsilon &= \sqrt{\left(\frac{\partial F}{\partial T_A} \sigma_{T_A}\right)^2 + \left(\frac{\partial F}{\partial T_B} \sigma_{T_B}\right)^2} = \pm 142.2 \text{ ns} \end{aligned} \quad (4-12)$$

This calculated value agrees closely with the observed standard deviation of ϵ , 148.7 ns. This indicates that at least the majority of random error in the Burredo is accounted for by quantization error. The value calculated by the propagation of variances does not take into account the uncertainties associated with the 1PPS measurement, as well as stochastic electromagnetic effects within the physical system, all of which contribute to the greater uncertainty observed in the data. The presence of these additional uncertainties was confirmed by

an F-test of the ratio of calculated to observed variances, which rejected the null hypothesis that the variances are statistically equal at the 95% confidence level.

In order to evaluate the impact of errors due to synchronization, the flight dynamics must also be characterized. The navigation parameters from a typical NOVA II flight line were selected, as shown in Figure 4-10. The flight from which the data was extracted was collected on March 4th, 2009 at 9:45 AM. The temperature was 63°F and winds were out of the north at approximately 3.5 m/s. Flying height above ground during the data sample shown was a commanded 150 meters above ground level. From these parameters, the flight dynamics were calculated and the results given in Table 4-5. The accompanying RMS error due to synchronization error and aperture uncertainty are also indicated in Table 4-5. The synchronization error was calculated using the RMS error of the Burredo and the aperture uncertainty calculated using the typical exposure duration of 1/2000th of a second. The aperture uncertainty was calculated assuming linear dynamics over the exposure period, and indicated the RMS change in navigation parameters over the duration of the exposure.

Image Overlap and Flight Planning

The amount of overlap between adjacent images is an important consideration in the ability to reconstruct scene geometry and improve the EOP estimates. A number of factors influence image overlap, including the camera parameters such as focal length, sensor size, and rate of capture, as well as flight parameters such as target flying height, airspeed, and flight line spacing. A thorough understanding of both the camera parameters and flight parameters allows for a reliable flight planning procedure that provides predictable overlap in the image data set. Using a UAV, where it is necessary to fly relatively low to the ground both to meet federal aviation requirements as well as the more practical concern of getting good resolution results in data sets, has considerable impact on flight planning. The paramount goal of flight planning is to ensure

that there is sufficient image overlap for the desired processing output while maximizing the resolution and efficiency of data capture. Three types of processing output are considered here.

- **Single Image.** No image overlap is required, but direct georeferencing accuracy is limited by the quality of the navigation system alone and cannot take advantage of the technique proposed in this thesis. With single images as the desired output format, high resolution imagery is the primary goal.
- **2D Mosaic.** Appropriate when gathering data over flat terrain with few vertical objects, and continuous mosaic coverage of the target area is required. Sufficient image overlap is needed to generate a robust network of tie points, but is compromised by the desired high-resolution of the imagery.
- **3D Scene Reconstruction.** For a three-dimensional reconstruction of the scene, all objects in the scene must have full stereoscopic coverage, meaning that all ground coverage must be imaged at least twice.

Of the camera parameters mentioned above, the capture rate is perhaps the most significant. Measurements showed that the maximum sustained image capture rate was 0.4 frames/s, or about one frame capture every 2.5 s, similar to the NOVA I capture rate of 0.42 frames/s. [Bowman, 2008a]. There is an implicit tradeoff in image overlap between capture rate, flying height, ground speed, and focal length. Among these variables, the capture rate is nearly constant and the ground speed is constrained to a limited range by aerodynamic constraints, leaving focal length and flying height as variables. Furthermore, given that a minimum image overlap is required for mosaic and 3D outputs, the necessity to fly higher or to use a wider lens (shorter focal length) in order to ensure proper overlap leads to a direct tradeoff with the ground resolution of the camera. It can be shown by way of proof using Equations 2-13 through 2-16, that for a given overlap, capture rate, and ground speed, the ground resolution will be the same regardless of the lens (focal length).

$$\begin{aligned}
H &= \frac{\beta \cdot f}{S_y(O_y - 1)} \\
H &= \frac{\gamma \cdot f}{S_x(O_x - 1)}
\end{aligned}$$

H = flying height
f = focal length
 β = air base
 γ = flight line spacing
 S_y = sensor size parallel to the flight line
 S_x = sensor size perpendicular to the line
 O_y = image overlap along flight line
 O_x = image overlap between flight lines

(4-13)

$$\begin{aligned}
\beta &\cong \text{Frame Rate} * \text{Ground Speed} \\
\frac{\beta}{S_y(O_y - 1)} &\cong C \text{ where } C = \text{constant}
\end{aligned}$$
(4-14)

$$\frac{H}{f} = C$$
(4-15)

$$G_y = \frac{H}{f} \cdot S_y = C \cdot S_y$$

G_y = ground coverage along the flight direction

(4-16)

Equation 4-15 illustrates that the ratio of flying height to focal length is a constant scale factor for a given sensor size, airbase, and required overlap. Since all terms on the right side of Equation 4-16 are constant, the resulting ground coverage along the flight direction is constant for a given overlap, sensor size, and airbase regardless of focal length and associated flying height. The number of pixels per ground area, a rough measure of resolution, will remain constant regardless of focal length selection. Equations 4-15 and 4-16 indicate that increasing the focal length to improve resolution requires an increase in flying height to maintain image overlap, effectively canceling the improvement in ground resolution. This leads to the conclusion

that selection of an appropriate lens should be dependent on factors other than focal length, namely resolving power, lens distortion, and the need to reduce flying height to minimize atmospheric effects on resolution and accuracy.

The primary purpose of the technique proposed in this thesis is to generate 2D mosaics; however, the technique may be applied to 3D outputs. Although the flight parameters can be calculated for a desired image overlap using Equation 4-13, the flight planning process is complicated by the fact that Equation 4-13 is only valid for vertical photographs oriented in the direction of flight. Because the autopilot flight control system has a limited ability to maintain constant course and the winds aloft can induce changes in orientation and ground speed of the aircraft, the planned overlap rarely corresponds with the true image overlap. Therefore, a conservative approach is required when estimating flight parameters. A flight planning table was developed for the NOVA II to aid in selecting proper flying height and flight line spacing given the expected groundspeed, and is shown in Figure 4-11.

The orientation of the camera with respect to the flight direction has a significant impact on the resulting image overlap. Sideslip, also called crabbing, occurs when the direction of travel is nonparallel to the longitudinal axis of the aircraft. This causes the camera to be rotated relative to the direction of travel. Sideslip is most commonly caused when the prevailing wind is nonparallel to the direction of travel. Thus, the direction of the planned flight lines should be oriented into the prevailing wind to minimize crabbing. Unfortunately flight paths parallel to wind direction also maximize effects of wind variation to the ground speed of the aircraft, as the plane must maintain a constant airspeed with respect to the moving air mass to remain airborne. This relationship is given by Equation 4-18.

$$\begin{bmatrix} v_x^l \\ v_y^l \\ v_z^l \end{bmatrix} = \begin{bmatrix} v_x^{air} \\ v_y^{air} \\ v_z^{air} \end{bmatrix} + \begin{bmatrix} v_x^{wind} \\ v_y^{wind} \\ v_z^{wind} \end{bmatrix} \quad (4-18)$$

From Equation 4-13, the airbase is determined by the ground speed when the capture rate of the camera is constant, so the overlap will be greater when flying upwind and will decrease when flying downwind. As a result, flight planning must always be determined by using a conservative estimate for target groundspeed equal to the required airspeed to maintain flight plus wind speed. This procedure will result in upwind flight lines having remarkably better overlap than their downwind counterparts, which allows the operator to target upwind flight lines over the areas of greatest interest.

A final flight planning consideration for the NOVA II platform concerns the turning radius of the aircraft. Sufficient space must be provided at the ends of flight lines to allow the aircraft to change direction and regain straight and level flight before entering the target area. By incorporating turning radius details with the other flight planning considerations mentioned earlier, the ‘dipole’ flight pattern was developed by Matthew Burgess and found to be effective (Figure 4-12). The dipole flight pattern has the advantage of concentrating the highest image overlap in the center of the region of interest, and all but two pairs of flight lines have a flight direction common to the adjacent flight line.

The sample data set used to evaluate the overlap is shown in Figure 4-13. As can be, the stereoscopic coverage is nearly (but not consistently) continuous, which precludes the data set from being used for full 3D reconstruction outputs. This flight plan did achieve respectable 2D mosaic results as demonstrated in Chapter 6. The analysis of image overlap was using the output generated by the full technique described in this thesis. Only upwind flight lines were evaluated, resulting in a predicted groundspeed of 19.5 m/s. The flight line analysis was conducted using a

flight line which composed part of the sample data set, and was found to be consistent with other flight line samples.

The overlap values observed in the data set agreed with the calculated values presented in the NOVA II Flight Planning Guide (Figure 4-11). Using Figure 4-13 with a commanded altitude of 150 m, a predicted value of 45% overlap in the direction of travel (forward lap or endlap) and 30% overlap between flight lines (sidelap) was expected. The actual measured image overlap values obtained are shown in Table 4-6. As expected, the upwind and downwind velocities were significantly different and corresponded to the variations in the airbase between sequential images shown in Figure 4-14, verifying the need for using downwind groundspeed estimates in the flight planning process.

Analysis of the flight lines showed that the NOVA II was able to maintain remarkably straight and level flight, with a mean deviation (or error) from a straight flight line of 1.2 m and a standard deviation of .92 m, shown in Figure 4-15. The ideal straight flight line was calculated by taking a general least squares linear regression of the horizontal position data, allowing for error in both the easting and northing directions. The general least squares approach produces a more realistic error assessment by calculating residuals normal to the fitted line. The standard deviation in height from the ideal flight line was found to be 0.6 m (Figure 4-16).

It goes without saying that the true flying height of the aircraft is a critical part of the flight planning and overlap analysis. The accuracy of the flying height is determined by the autopilot navigation system, not the payload navigation system. Unfortunately, the error between the commanded and actual height can't be empirically evaluated *in situ* because the data could not be benchmarked on the current platform. An independent evaluation of the performance of the system at ground level conducted by the author on the NOVA I platform showed that the system

has a height accuracy of approximately 2 m [Perry et al., 2008]. This value is somewhat better than the typical code-solution GPS height error, probably because the autopilot aids the altitude solution with a barometer calibrated at ground level before flight.

The success of orienting the flight lines in parallel to the prevailing wind direction is evident in the angle of sideslip, shown in Figure 4-17. The sideslip was estimated by using the previously described least-squares fitted line for the true flight direction and comparing it to the heading provided by the payload navigation system. It should be noted that this estimate suggests a much higher in situ heading accuracy than the one found in the Navigation Accuracy section of this chapter. The mean angle of sideslip was 1.7 degrees with a standard deviation of 1.2 degrees. The mean magnitude of the deviation from vertical (tilt) was 7.8 degrees with a standard deviation of 1.5 degrees, also shown in Figure 4-17. Given that a strong bias is evident in the tilt angle, it may indicate the need to more precisely orient the camera relative to the ‘level’ orientation of the plane during flight. It should be noted that the standard deviation in the roll direction, 1.9 degrees, was significantly higher than the pitch direction, 1.1 degrees. This is most likely attributed to the relative ability of the plane to maintain level flight (inducing pitch) to maintaining direction (inducing roll), suggesting that flight line spacing estimates should be even more conservative.

Table 4-1. SCBA-adjusted IOPs including distortion parameters for the Lightning Lab camera calibration data set (* denotes pixel units)

Parameter	Type	Value	Stan. Dev.	t-statistic
f	Focal Length*	5308.1342	8.3492	2.1720
x_o	Principal Point*	-0.1034	3.1247	0.0331
y_o	Principal Point*	-1.5013	3.0906	0.4857
k_1	Radial	+5.6493e-009	3.9899e-010	14.1591
k_2	Radial	+1.5363e-016	1.8984e-016	0.8092
k_3	Radial	-3.5228e-023	2.7153e-023	1.2974
t_1	Tangential	-1.3741e-007	5.0827e-008	2.7035
t_2	Tangential	+7.0757e-008	4.2883e-008	1.6500

Table 4-2. SCBA-adjusted EOPs for the Lightning Lab camera calibration data set

Image	Omega (deg)	Phi (deg)	Kappa (deg)	Easting (m)	Northing (m)	Height (m)
770	+5.11	+7.14	-3.53	400393.48	3312756.85	235.87
796	+1.80	+4.12	-0.47	400427.16	3312748.56	239.23
812	-17.70	-22.02	-217.74	400344.32	3312801.44	237.61
894	+10.61	+11.32	-71.40	400426.18	3312747.42	229.37
919	-9.41	+5.44	+45.13	400423.19	3312778.38	231.22
937	+10.81	+4.82	-68.89	400432.49	3312720.75	232.68
1004	-12.25	+6.00	+51.21	400447.67	3312831.82	231.49

Table 4-3. Boresight and leverarm calibration results

	Omega (deg)	Phi (deg)	Kappa (deg)
<i>Boresight Angles (deg)</i>	-4.9639	-0.4139	0.9933
<i>Mean Residual</i>	-0.0098	-0.0150	0.0415
<i>Std.Dev. Residual</i>	1.8615	1.5022	1.9312

Table 4-4. Navigation system benchmarking results

	Roll (deg)	Pitch (deg)	Heading (deg)	Easting (m)	Northing (m)	Height (m)
<i>Dynamics RMS error</i>	1.7969	1.1286	16.2244	11.5007	26.0204	6.9016
<i>Static RMS error</i>	1.4167	1.1267	8.3706	4.9467	5.5153	4.2197

Table 4-5. The calculated RMS error in the navigation parameters due to synchronization error and aperture uncertainty in the navigation parameters for the given dynamics

	Roll (deg)	Pitch (deg)	Yaw (deg)	Horizontal Position (m)	Vertical Position (m)
<i>Dynamics</i>	3.22°/s	7.19°/s	2.53°/s	18.61 m/s	0.79 m/s
<i>Sync Error</i>	$8.26^\circ \cdot 10^{-7}$	$18.46^\circ \cdot 10^{-7}$	$6.50^\circ \cdot 10^{-7}$	$4.77\text{m} \cdot 10^{-6}$	$2.03\text{m} \cdot 10^{-7}$
<i>Aperture Error</i>	$1.6^\circ \cdot 10^{-3}$	$3.6^\circ \cdot 10^{-3}$	$1.3^\circ \cdot 10^{-3}$	$9.3\text{m} \cdot 10^{-2}$	$4.0\text{m} \cdot 10^{-4}$

Table 4-6. Ground coverage and overlap parameters for typical NOVA II flight lines

	Width (m)	Height (m)	Forward (m)	Side (m)	% Endlap	% Sidelap
Average	116.8	87.1	44.9	41.2	52%	35%
Std. Dev.	1.5	0.9	8.7	10.3		



Image770



Image796



Image812



Image894



Image919



Image937



Image 1004

Figure 4-1. Lightning Lab Calibration Site calibration data set images 770, 796, 812, 894, 919, and 1004

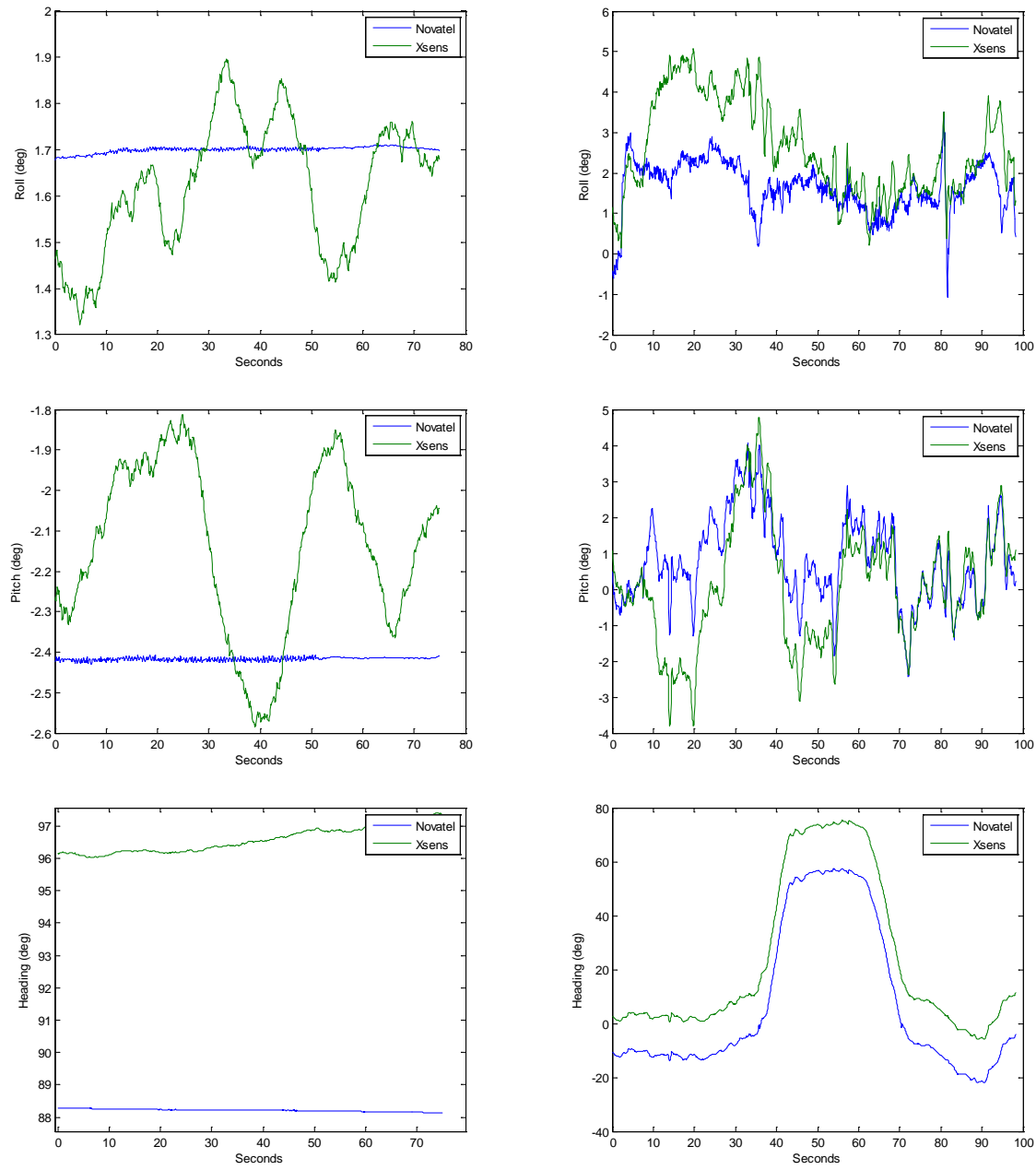


Figure 4-2. Comparison of the SPAN[®] and MTi-G[™] attitude parameters over time for the static (left) and dynamic (right) portions of the navigation benchmarking experiment

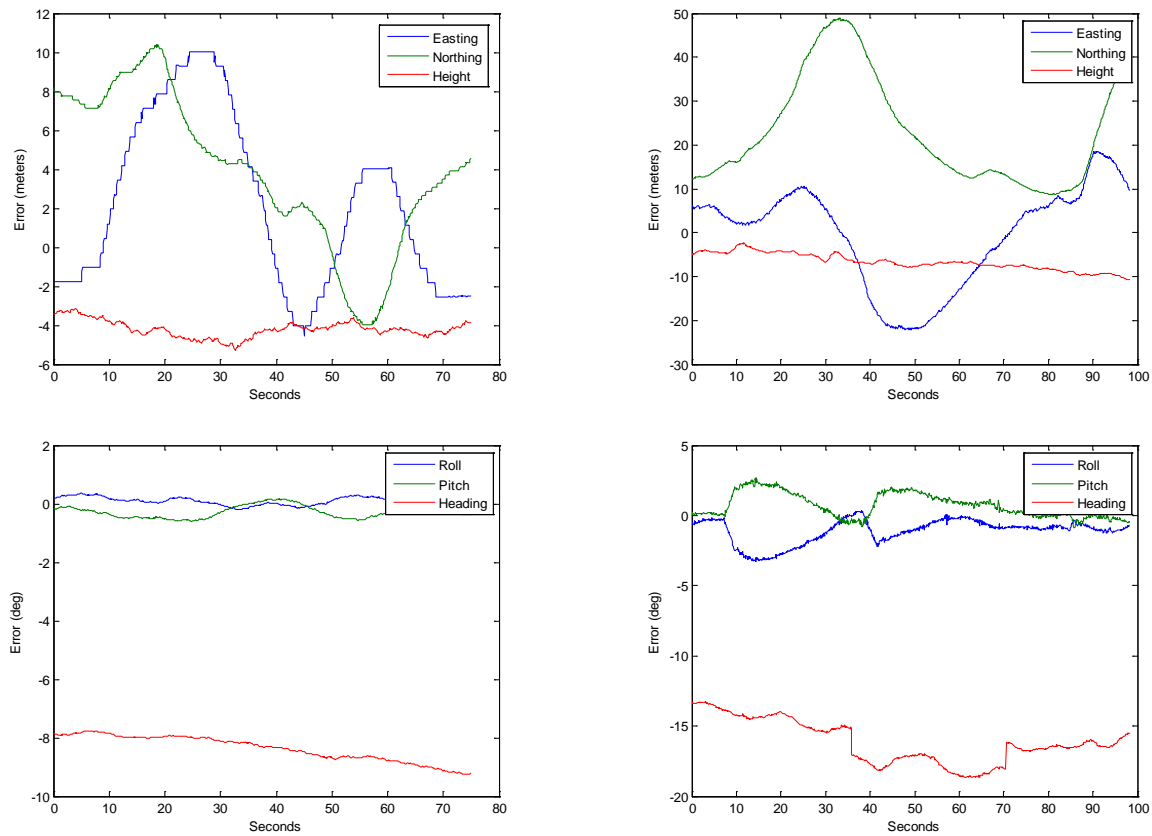


Figure 4-3. Error profiles of MTi-G™ position and orientation parameters during the static (left) and dynamic (right) portions of the navigation benchmarking experiment

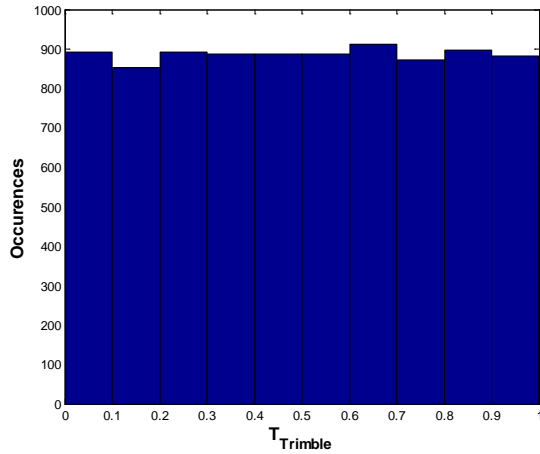


Figure 4-4. Distribution of the pseudo-random triggers as a fraction of the UTC second during the synchronization accuracy assessment

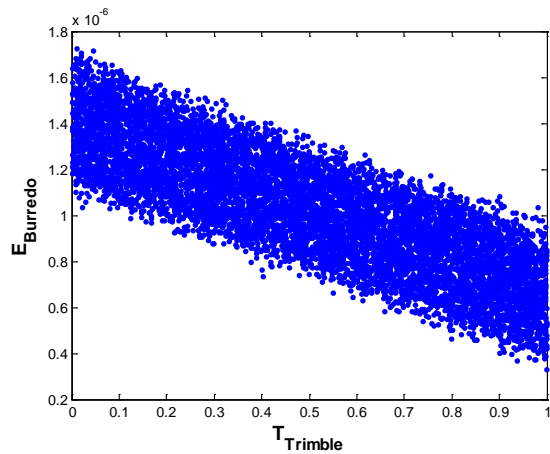


Figure 4-5. Evident linear trend in the error of the uncorrected synchronization data attributed to ΔT_{reset}

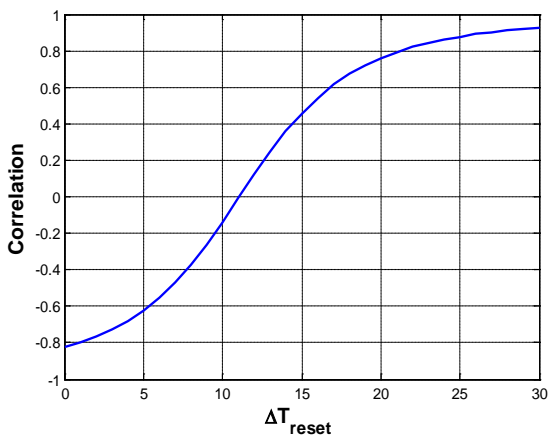


Figure 4-6. The correlation of the synchronization error to the fraction of the UTC second at which it occurred plotted against possible values of ΔT_{reset}

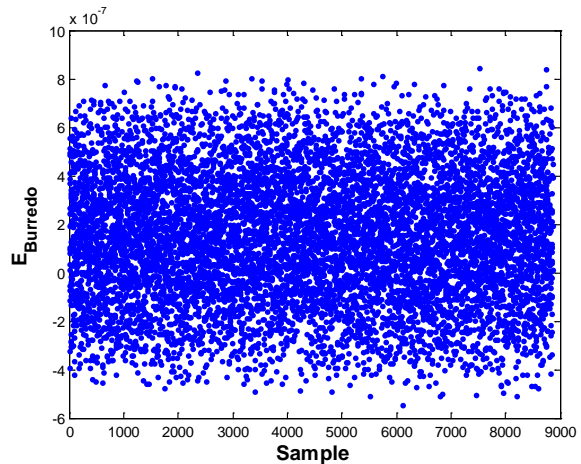


Figure 4-7. The value of the synchronization error over time in hundreds of nanoseconds

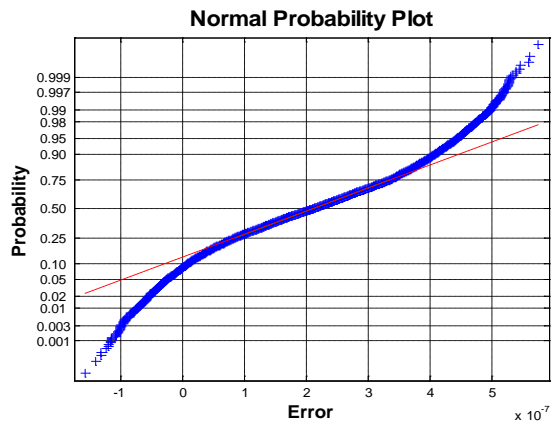


Figure 4-8. Normal probability plot of the synchronization error showing low kurtosis

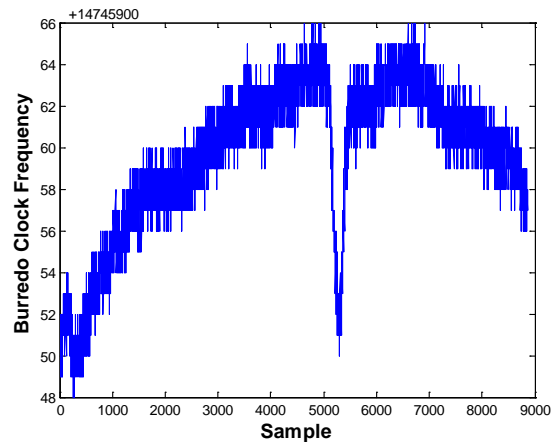


Figure 4-9. Drift of the Burredo's crystal oscillator over time

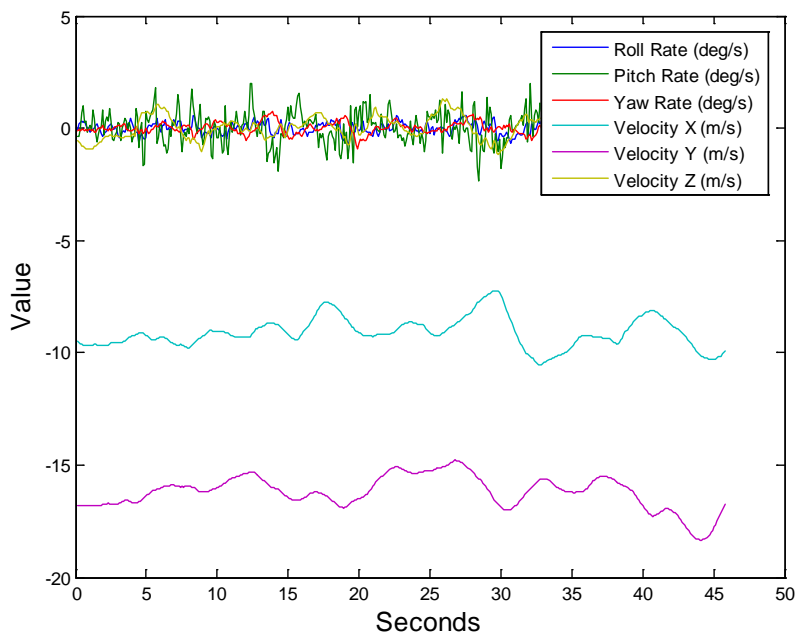


Figure 4-10. Typical NOVA II dynamics while flying straight and level

Flight Planning Guide

				Altitude (m)																			
				400	79%	78%	77%	76%	75%	73%	72%	71%	70%	68%	67%	66%	65%	64%	3D Coverage				
55	110	165	220	400	79%	78%	77%	76%	75%	73%	72%	71%	70%	68%	67%	66%	65%	64%	61%				
52	103	155	206	375	78%	77%	75%	74%	73%	72%	70%	69%	68%	66%	65%	64%	62%	61%					
48	96	144	192	350	76%	75%	74%	72%	71%	70%	68%	67%	65%	64%	63%	61%	60%	58%					
45	89	134	179	325	75%	73%	72%	70%	69%	67%	66%	64%	63%	61%	60%	58%	57%	55%	53%	52%	2D Mosaic		
41	82	124	165	300	73%	71%	69%	68%	66%	64%	63%	61%	60%	58%	56%	55%	53%	52%					
38	76	113	151	275	70%	68%	66%	65%	63%	61%	59%	58%	56%	54%	52%	51%	49%	47%					
34	69	103	137	250	67%	65%	63%	61%	59%	57%	55%	53%	52%	50%	48%	46%	44%	42%					
31	62	93	124	225	63%	61%	59%	57%	55%	53%	50%	48%	46%	44%	42%	40%	37%	35%					
27	55	82	110	200	59%	56%	54%	52%	49%	47%	44%	42%	39%	37%	35%	32%	30%	27%					
24	48	72	96	175	53%	50%	47%	45%	42%	39%	36%	33%	31%	28%	25%	22%	20%	17%	Individual				
21	41	62	82	150	45%	42%	39%	35%	32%	29%	26%	22%	19%	16%	13%	9%	6%	3%					
17	34	52	69	125	34%	30%	26%	22%	19%	15%	11%	7%	3%	-1%	-5%	-9%	-13%	-16%					
14	27	41	55	100	18%	13%	8%	3%	-2%	-7%	-12%	-16%	-21%	-26%	-31%	-36%	-41%	-45%					
10	21	31	41	75	-10%	-16%	-23%	-29%	-36%	-42%	-49%	-55%	-62%	-68%	-75%	-81%	-88%	-94%					
7	14	21	27	50	-65%	-75%	-84%	-94%	-104%	-113%	-123%	-133%	-142%	-152%	-162%	-172%	-181%	-191%					
3	7	10	14	25	-230%	-249%	-269%	-288%	-307%	-327%	-346%	-366%	-385%	-404%	-424%	-443%	-463%	-482%					
80%	60%	40%	20%		17	18	19	20	21	22	23	24	25	26	27	28	29	30					
Sidelap %				Groundspeed (m/s)																			

Instructions:

1. Calculate groundspeed = programmed airspeed + observed wind
2. Select altitude based on desired endlap using the right side of the table
3. Select flight line spacing distance on the left side of the table based on desired sidelap percentage

Figure 4-11. Flight planning guide for determining flying height and flight line spacing for a desired overlap

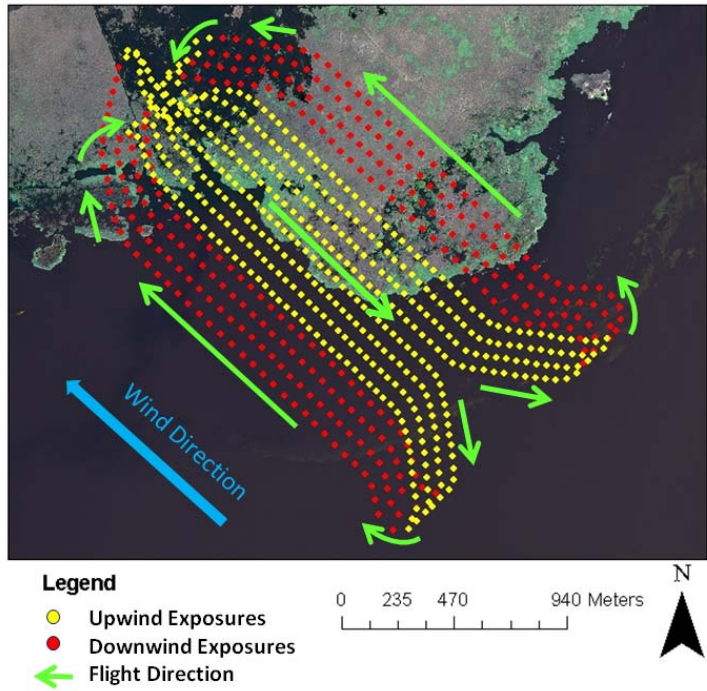


Figure 4-12. Typical flight line configuration for the NOVA II, demonstrating the 'dipole' pattern

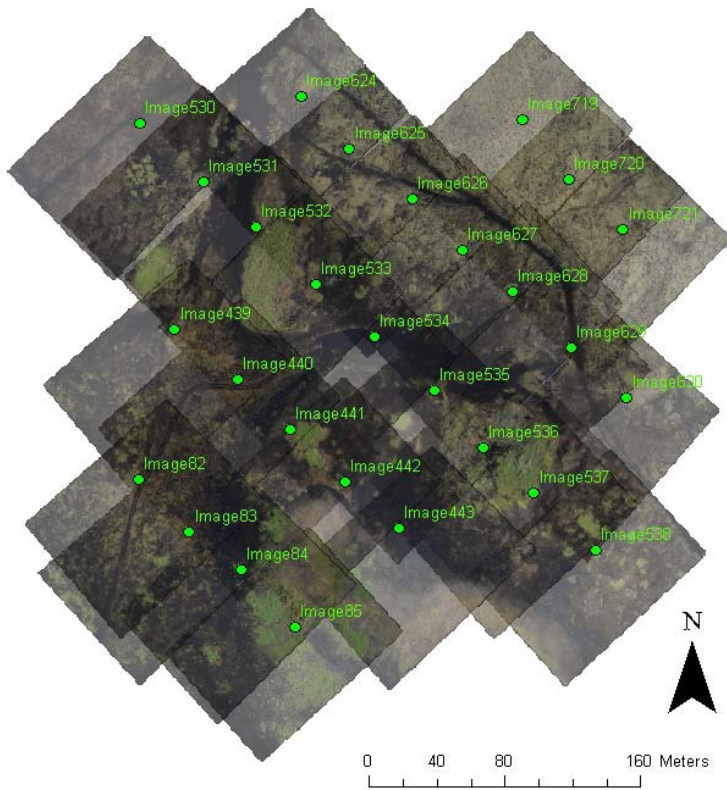


Figure 4-13. Example of the image overlap configuration for a typical NOVA II flight

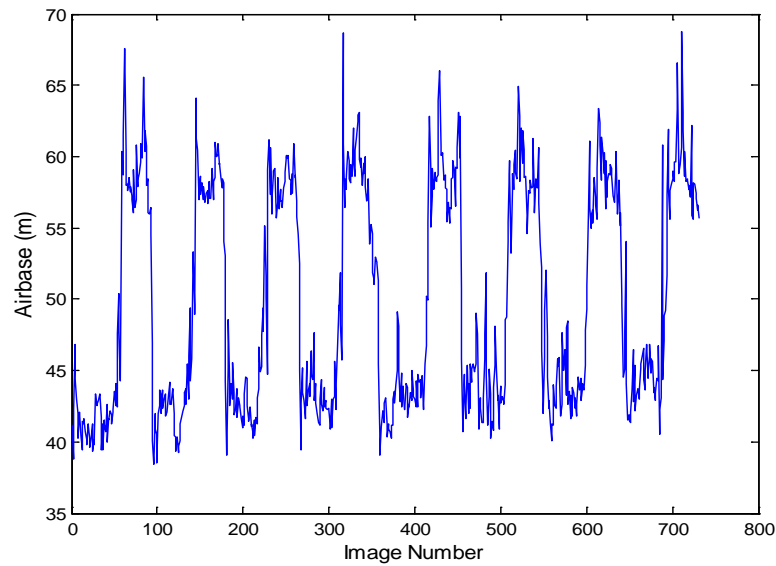


Figure 4-14. Sequential-image airbase for a typical NOVA II flight showing variations due to flight direction relative to the prevailing wind

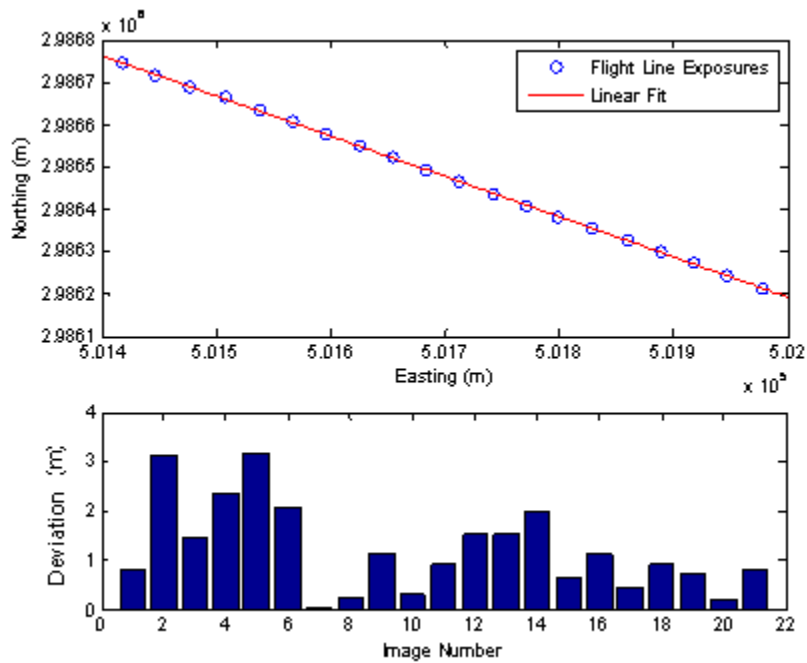


Figure 4-15. Typical horizontal deviation of the NOVA II from an ideal flight line

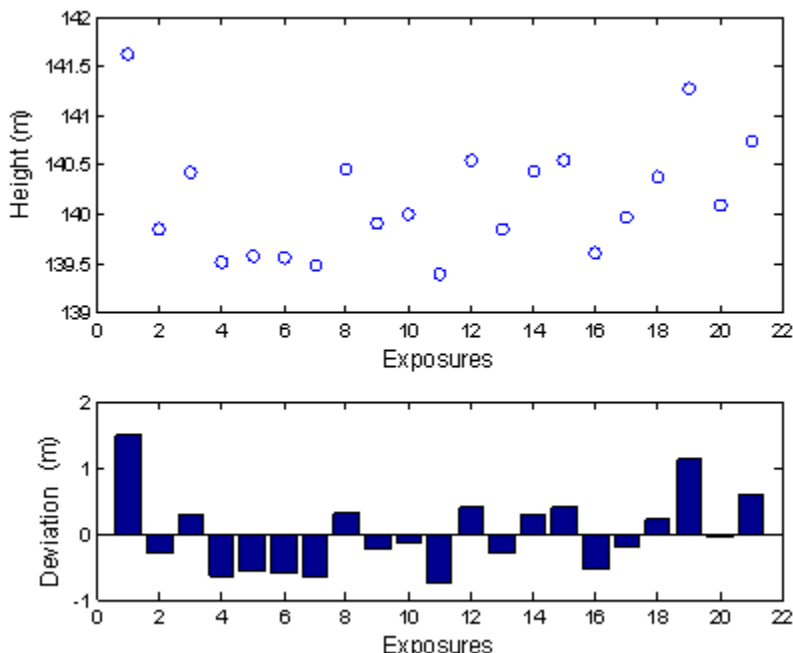


Figure 4-16. Typical vertical deviation of the NOVA II from an ideal flight line

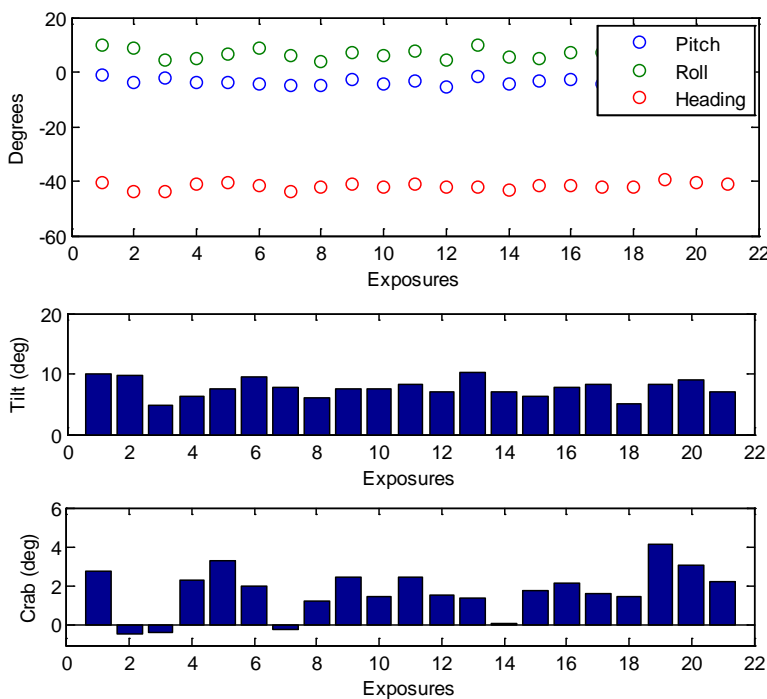


Figure 4-17. Typical orientation deviation of the NOVA II from ideal flight line

NOVA II

Indian Prairie Flights

Sponsored By:



Army Corp of Engineers



Legend

- ◆ 27-01-2009-00-49-06
- ◆ 27-01-2009-01-36-54
- ◆ 27-01-2009-04-54-03
- ◆ 27-01-2009-23-10-15
- ◆ 28-01-2009-00-39-42
- ◆ 28-01-2009-01-55-06

 Spray Areas

Flights: January 26-27th, 2009
Produced: January 28th, 2009

UF | UNIVERSITY of
FLORIDA

Figure 4-18. Coverage map for a two-day data collection mission conducted on behalf of the Army Corp of Engineers

CHAPTER 5

PROCESSING ALGORITHM

Overview of the Algorithm

The goal of the algorithm was first and foremost to produce accurate mapping products from the directly georeferenced remote sensing payload of the NOVA II. The algorithm should only use inputs generated by the DGRS, with no a priori information needed. Due to the large volume of data that was generated by the platform, it was desirable and perhaps necessary to automate the process to the greatest extent possible. Due to the complexity of the problem, it was necessary to make certain assumptions about the geometry of the scene. These assumptions came with a tradeoff of the robustness of the algorithm. The algorithm was designed, where possible, to be computationally efficient due to the extremely large data sets generated by high resolution DGRS [Grenzdörffer, 2004]. The mapping output of the algorithm had to be in a format readable by standard GIS software. These goals underlying goals were met in the development of the algorithm.

The output of the NOVA II platform, an example of which is provided in Appendix A, provides a self-contained data set suitable for input to the algorithm. The flight log files must be parsed to produce the geotag and navigation files prior to starting the algorithm. The data set is contained in a single folder, the path of which is provided to the program. The folder contains all the images from the flight, as well as the unadjusted geotag file which provides the directly georeferenced parameters for each image. In addition to the flight data, calibration data such as the focal length of the camera and the boresight and leverarm calibration are required. Upon providing these initial parameters, the program parses the geotag file and indexes the folder contents to create an internal representation of the data set. The algorithm implements the following steps, each of which will be examined in detail:

- **Preprocessing.** The data set is constructed using the geotags file and the calibration parameters, and the images are pyramided and radiometrically modified for later use.
- **Interest Point Generation.** Each image is analyzed for features with good potential for matching, generating a potential tie point list for each image.
- **Initial Approximation.** Approximations of the object space coordinates of each potential tie point and each image extents is generated.
- **Semi-automatic Point Matching.** Potential tie points are matched based on a search space defined by the initial approximation.
- **Bundle Adjustment.** Matched tie points are collated and a bundle adjustment of all available geometric information is performed.
- **Surface Generation.** A surface is generated based on the object space coordinates of adjusted tie points and used for mosaicing.
- **Mosaicing.** The scene extents are recalculated based on adjusted exterior orientation parameters, the space is segmented into subscenes, the aerial images are resampled using the collinearity equations, and a georeferenced output mosaic is generated.

Preprocessing

To begin, the exterior orientation parameters provided by direct georeferencing must be brought into the object coordinate system. The navigation coordinates are converted to the appropriate UTM coordinate system and the leverarm calibration is applied using Equation 2-15. Recall from the discussion in Chapter 2 that using UTM coordinate as object space coordinates for photogrammetric processing simplifies the final process of generating the georeferenced mosaic at the cost of introducing some error.

It is necessary to filter the data set for valid images, which are selected from the data set by taking the highest altitude in the navigation parameters and selecting all images which are above a threshold altitude. This allows images which were taken during takeoff and landing to be excluded, since they are unlikely to contain sufficient image overlap to be useful. The threshold is set to a fixed offset from the maximum height. The assumption for this filtering process is that the plane's maximum flying height was nearly the flight line flying height.

An initial approximation for the ground height is also calculated by taking the minimum altitude in the navigation data set. This assumption may be violated if the plane was launched from and landed on a platform that was significantly higher than the ground height, such as operating from a levee when mapping nearby wetland vegetation. On an operational basis, it is usually not inconvenient to transport the plane to the average terrain height before launching. An improvement on this initial approximation may be to use a cluster detection algorithm and calculate a mean of the lowest cluster if it is not significantly different from the smallest value, ensuring that an outlier in the navigation-provided height is not used.

A resolution pyramid is generated for each image for use in the tie point matching step, an integral requirement for many tie point matching schemes [Zitová and Flasser, 2003] and a practical method of improving the computational efficiency of initial tie point matching states. Each pyramid level is convolved using a 5×5 Gaussian kernel and then subsampled by a factor of 2 to reach the next level. The number of pyramid levels automatically generated is determined by the size of the source image, which is downsampled until the final pyramid level is less than 500 pixels on both its width and height. This requires four pyramid levels, including the original, to reach a resolution of 456×352 pixels for the default NOVA II payload image size of 3648×2736 pixels.

The image pyramid is converted to grayscale to facilitate intensity-based tie point matching. The conversion is from the three-channel RGB color space to grayscale using Equation 5-1 [OpenCV, 2001]. The histogram of the grayscale images is then equalized using Equation 5-2 in order to maximize contrast and normalize the brightness in the grayscale image. The function maps each occurrence of an original gray level, I_{gray} , to an equalized gray level,

I_{eq} . An equalized histogram indicates that the probability distribution function of grayscale value is uniform, although the ideal is not possible due to discretization.

$$I_{gray} = 0.299I_{red} + 0.587I_{blue} + 0.114I_{green} \quad (5-1)$$

$$I_{eq} = T(I_{gray}) = \frac{\text{total grey levels} - 1}{\text{total pixels}} \sum_{j=0}^{I_{gray}} n_j$$

$n_j = \text{is the number of pixels with the } j_{th} \text{ gray level}$

(5-2)

The preceding radiometric preprocessing steps deal exclusively with preparing the imagery for the subsequent algorithmic processes. In fact, they decrease the available information in the image. It is also of interest in radiometric preprocessing to improve the source images to increase the quality of the output mosaics. These techniques must generally be approached cautiously, since radiometric modification can negatively affect remote sensing techniques if the information content of the imagery is reduced [Showengerdt, 2007]. The most commonly desired improvement is to minimize the apparent discontinuities around mosaic seams, and classic approaches deal with this problem as an integral part of the mosaic process rather than in preprocessing [Kraus, 2007]. A more robust method is to balance the illuminance of the imagery both within each image and between adjacent images [Palubinskas et al., 2003]. By removing the effects of the geometry and variations in intensity of the lighting source, the output mosaic is more visually appealing by reducing the apparent discontinuities between images. This global rather than local approach to color balancing is desirable but comes with considerable computational cost.

Interest Point Generation

As described in Chapter 2, tie points are features in the scene that can be identified in more than one image. The accuracy of the geometry is dependent on the ability to precisely measure the location of the feature in the image. It is essential, then, that tie points be selected that can be uniquely localized in the image, particular in the context of automated image matching [Zitová and Flásher, 2003]. However, localization is complementary to repeatability, which is the ability to detect a point between multiple views [Schmid et al., 2000]. As localization accuracy increases the repeatability rate will decrease. An assessment of the corner detection algorithms in the literature found that the Harris Corner Detector (HCD) performs the best among popular algorithms for both repeatability and localization of matched points between images subject to rotation, scaling, and contrast change [Schmid et al., 2000]. The HCD was implemented in the algorithm to select potential tie points at the desired pyramid image.

The HCD searches for points where a Gaussian-weighted kernel about the point has a high local autocorrelation [Harris and Stephenson, 1988]. A shifted window is approximated by a first-order linearization given by Equation 5-3 and used to calculate the autocorrelation function about the point of interest in Equation 5-4. The Harris Corner Detector is then given in Equation 5-5 by the derived autocorrelation function, excluding the pixel shift terms which act as a constant scale. Corner points are points which have large local variations in intensity values, quantified by the partial derivatives in the HCD matrix. Thus, it would be expected that the HCD would have two large eigenvalues for points of interest. If only one or the other eigenvalue of the HCD is large, then an edge has been detected. If both eigenvalues are small, then the region has little intensity variation and should be rejected. For computational efficiency, the eigenvalues of the HCD are approximated by Equation 5-6.

$$G(x + \Delta x, y + \Delta y) \cong G(x, y) + \left[\frac{\partial x}{\partial G}(x, y) \quad \frac{\partial y}{\partial G}(x, y) \right] \begin{bmatrix} \Delta x \\ \Delta y \end{bmatrix}$$

where $G(x, y)$ is the Gaussian kernel centered about $I(x, y)$

(5-3)

$$R_{GG}(x, y) = [\Delta x \quad \Delta y] HCD(x, y) \begin{bmatrix} \Delta x \\ \Delta y \end{bmatrix}$$

(5-4)

$$HCD(x, y) = \begin{bmatrix} \sum_G \left(\frac{\partial x}{\partial G}(x, y) \right)^2 & \frac{\partial x}{\partial G}(x, y) \frac{\partial y}{\partial G}(x, y) \\ \frac{\partial x}{\partial G}(x, y) \frac{\partial y}{\partial G}(x, y) & \left(\frac{\partial y}{\partial G}(x, y) \right)^2 \end{bmatrix}$$

(5-5)

$$eig(HCD) \cong |HCD| - \kappa \operatorname{trace}^2(HCD)$$

κ = the Harris sensitivity parameter

(5-6)

The HCD assigns an interest factor for all pixels in the image based on the magnitude of the eigenvalues. The algorithm then selects the points which have the highest interest factor above a quality threshold and are separated by a minimum distance, up to a selected maximum number of points. The minimum separation distance ensures that the points are well-distributed across the image. The maximum number of points will not be returned if there are not enough points above the quality threshold, defined as a percentage of the maximum interest factor.

Initial Approximation

The initial approximation process is the core result of the data synthesis arising from DGRS, and significantly affects the essential tasks of tie point matching and the bundle adjustment. Unfortunately, it is accompanied by the need to make strong assumptions about the scene which can greatly reduce the robustness of the method. The initial approximation refers to the need to provide an estimated object coordinate for each potential tie point. As discussed in detail in Chapter 2, direct georeferencing only allows the collinearity equations to be solved up

to a scale factor, repeated here for clarity. With known exterior and interior orientation parameters, the object space coordinate is only known to lie on a line coincident with the perspective center and the image point. This result is certainly a vast improvement over traditional techniques where both the exterior orientation parameters and the Z-ambiguity must be solved simultaneously. However, it remains that estimation of the tie point object space coordinate is dependent on an estimate of where it is along that line.

The current operational paradigm for the NOVA II is flying straight and level flight lines over relatively smooth terrain. In fact, the majority of past and planned missions occur over wetlands where differences in elevation are for all practical purposes non-existent. These conditions give sufficient motivation to make a constant-surface assumption about the scene. This assumption allows the object space Z-coordinate to be assigned based on the ground level, determined in the preprocessing stage. Having resolved the Z-ambiguity, it is a trivial matter to calculate the object coordinates for the potential tie points using the ‘Project Down’ formulation in Equation 2-10.

Having calculated an approximate object space coordinate, it is an obvious result that it can be used as the initial approximation in the linearized bundle adjustment. Real gains, however, are also to be had in the tie point matching algorithm. Considering the typical flight takes about one thousand images, it is clear that it would be computationally burdensome to the point of impracticality to attempt to match thousands of tie points if each tie point could possibly exist anywhere in any of the images. Thus, the algorithm exploits the initial approximations provided by direct georeferencing to vastly narrow the search space of the tie point matching algorithm.

Narrowing the search space is accomplished by projecting the extents of each image down to the constant surface, generating a set of 2D four-vertex polygons. Each interest point object

coordinate is then tested to see whether it falls within each image polygon. This returns a list of tie points which are potentially located within each image, narrowing the search space for each potential tie point to a subset of the images. Furthermore, by using the ‘Project Up’ collinearity equations, Equation 2-9, an approximate image coordinate can be generated for each potential tie point in each of the overlapping images.

In order to account for the error due to both the inaccuracy of the constant surface assumption and the inaccuracy of the exterior orientation parameters provided by direct georeferencing, it is necessary to define a tie point matching search space about the approximate image coordinates. A formulation for empirically determining the extent of the search space is impractical due to the non-linearity of the sequence of projections, and thus in implementation the search space can be tuned experimentally determined based on typical performance. An analysis of the image coordinate approximation is given in Chapter 6. A perhaps more serious consideration is that poor approximation also affect image boundaries. Direct projection of the image extents to the assumed surface may exclude points which are within the uncertainty bounds of the search space but are outside of the polygon because no valid image coordinate approximation exists.

A great deal of improvement is possible in both the object space approximations and the corresponding image coordinate approximations. Chief among these is to utilize an iterative approach, performing a lean bundle adjustment and surface approximation using the first iteration to improve the accuracy of subsequent repetitions of the initial approximation and tie point matching steps. Another improvement would be to better handle the boundary conditions, using a ‘fuzzy’ boundary for the image extents to include nearby points that may fall within the search space. Following each tie point matching procedure, it is also possible to refine the object

coordinate of the tie point calculating the average of the object coordinates calculated from projection of each image observation.

Epipolar geometry can also be employed to improve the search space of the tie point matching algorithm by utilizing direct georeferencing [Kraus, 2007]. Briefly, two epipoles are formed for each pair of images by the projection of the perspective center of each image onto the others image plane using the collinearity equation. An arbitrary surface is used to project the feature of interest from one image to the other. The coplanarity condition then states that the corresponding image features in the second image will lie along the line formed by the reprojected image coordinate and the epipole [Kraus, 2007]. This approach has the advantage of not requiring object coordinates for the tie point, transferring this Z-ambiguity from the object space to the corresponding image space. Combining the coplanarity condition with the described algorithm would allow the search space to be constrained about the epipolar line or intersection of lines if multiple epipole correspondences are calculated, further narrowing the search space.

Semi-Automatic Point Matching

Tie point matching has been an intense area of research in both the photogrammetric and computer vision communities, with a multitude of continually evolving applications and approaches. At the risk of producing an echo, I quote A.W. Gruen, a leading figure in the photogrammetric literature, paraphrasing a comprehensive review by A. Rosenfeld, of equal stature in the computer vision community, “...these new methods do not solve the problems addressed before.” Several pertinent image matching techniques will be discussed here, with the caveat that the method implemented proved sufficient but is entirely open to improvement.

Image matching may generally be divided into two approaches: feature-based matching or template-based (intensity-based) matching [Zitová, 2003]. The former attempts to extract structural information about the scene, such as points, line, or regions, and to then match

corresponding structures. Feature-based techniques typically require expert systems and are usually limited to well-defined image constraints. Moreover, they are the primary subject of the above quote. On the other hand, template-based matching is the more direct approach exploiting the intensity values of the images themselves to seek a match. Template matching can be thought of as image-to-image matching, where some source template (usually a subset of the image) is matched to a corresponding target image (also, usually a subsample of a larger image). The size of the template and target is selected such that distortions due to perspective changes are minimized and at worst can be well-modeled by an affine transformation.

The rudimentary exercise of template matching is to maximize the similarity between two templates and conversely minimize the dissimilarity or error. A common and well-known approach to template matching in the spatial domain is the normalized cross-correlation (NCC), given in Equation 5-8.

$$C = \frac{1}{n-1} \sum_{x,y} \frac{(I(x,y)_{src} - \mu_{I_{src}})(I(x,y)_{trg} - \mu_{I_{trg}})}{\sigma_{I_{src}} \sigma_{I_{trg}}}$$

n = number of pixels
I_{src}, I_{trg} = intensity of corresponding pixels
μ_{I_{src}}, μ_{I_{trg}} = mean intensity
σ_{I_{src}}, σ_{I_{trg}} = standard deviation of intensity

(5-8)

The cross-correlation of the intensity values for each image is normalized by the mean and standard deviation in order to account for variations in image brightness and contrast. The NCC has the advantage of being simple and relatively fast. A matching algorithm is implemented by ‘sliding’ the source template over the target search space to find the image coordinate where the NCC is maximized. The normalized cross-correlation is a translation-invariant matching technique. This method suffers from the inability to account for geometric and radiometric

distortion found in typical images. It is possible to augment the NCC technique with spatial-domain transformations that allow rotation- and scale-invariant matching.

The log-polar transformation (LPT), Equation 5-9, is a method for introducing scale and rotation invariance, both in combination with NCC and frequency-domain matching [Wolber and Zokai, 2000; Reddy and Chatterji, 1996]. Interestingly, the LPT is modeled after human foveal vision, and an example is shown in Figure 5-1. The transformation is not translation invariant, so the origin of the transformation is of account.

$$\begin{aligned} I(x, y) &= I(\theta, r) \\ \theta &= \text{atan}^{-1} \frac{y - y_o}{x - x_o} \\ r &= M \log \sqrt{(x - x_o)^2 + (y - y_o)^2} \end{aligned} \tag{5-9}$$

The LPT is rotation and scale invariant. A rotation in a Euclidean coordinate system corresponds to a linear shift in the θ -direction of the polar coordinate system. Noting that $\log(ax, ay) = (\log x + \log a, \log y + \log a)$, a scale factor in the Euclidean coordinate system corresponds to a linear shift in the r -direction of the log-polar system. The LPT has the additional advantage of effectively weighting the image matching algorithm at the focus of the transform.

Translation, rotation, and scale invariant template matching can be performed by combining NCC and the LPT [Wolber and Zokai, 2000]. Matching proceeds by first performing the LPT on the source template. An LPT transformation is then performed with the origin at each pixel in the target template. Normalized cross-correlation is then performed across each of the LPT-transformed target templates. The x- and y-coordinate that corresponds to the maximum NCC within the LPT-transformed target image corresponds to the scale and rotation parameters,

respectively, and the translation parameter is the origin of the LPT-transformed target image with the maximum NCC among all the transformed targets.

Another affine-invariant technique worth mentioning brings us to the frequency-domain matching methods. The phase correlation of the 2D Fourier transform provides the transformation parameter. An LPT can then be applied to the magnitude component of the Fourier Transform, followed by a second Fourier transform for which phase correlation then solves for the rotation and scale factors [Capodiferro, 1987]. This series of transformations is known as the Fourier-Mellin transform. This technique can also be applied to directly produce an affine-invariant transform if approximations of the affine parameters are not required.

Although the previous methods have been shown to be robust for affine-invariant matching, statistical methods for maximizing the similarity are limited to normalized cross-correlation and are not well-suited for sub-pixel matching. The parameters obtained from these methods may be optimized by employing a least-squares matching technique, given by Equation 5-10 [Gruen, 1985]. The LSM algorithm has the advantage of being robust to radiometric distortion and can provide accurate sub-pixel matching [Ibid.]. The a posteriori adjustment statistics also provide a meaningful measure of the accuracy of the match. Due to the non-linearity of the model initial approximations are required so the model is generally not implemented independent of aforementioned methods. Initial approximations for the parameters must typically provide a match within a few pixels of its true value for the LSM to converge.

$$\begin{aligned}
 I_{src} &= r_0 + r_1 I_{trg}(x', y') \\
 x' &= a_0 + a_1 x + a_2 y \\
 y' &= b_0 + b_1 x + b_2 y \\
 r_0, r_1 &= \text{radiometric shift and scale} \\
 a_0, a_1, a_2, b_0, b_1, b_2 &= \text{affine transformation parameters}
 \end{aligned} \tag{5-10}$$

The algorithm implemented in the proposed direct georeferencing algorithm is the combined NCC/LPT algorithm without a least-squares match. This decision was made because the initial results achieved by the algorithm were adequate, and because sub-pixel matching on the full resolution images was unnecessary for the desired accuracy and likely to be faulty due to perspective changes over irregular ground coverage without more robust blunder detection techniques. An assessment of the tie point matching algorithm performance is presented in the next chapter. The final set of matched tie points is then presented to the operator, allowing the user to reject blundered matches, and as a result of this the process is semi-automatic. No facilities are implemented for the manual addition or editing of tie points; the user is simply presented with the option to accept/reject the automated matches, allowing the manual process to be completed relatively quickly. This is possible because of the very high redundancy already available in the automated algorithm; the loss of a percentage of blundered points has little impact. Implementation of additional statistical blunder detection algorithms may allow the algorithm to be fully automatic.

In summary, there are two observations to be made on the tie point matching algorithm. The first is that despite the perspective projective nature of image formation, image matching techniques typically only model affine transformations. This is due to the assumption that tie points sweep a small area within the projection and for smooth object space features the affine well-approximates the projective transformation in this space. This assumption leads to the second observation that object space features that are irregular such as coarse vegetation tend to produce poor tie point matches. Given the high resolution of the imagery produced by the NOVA II, it can be advantageous to perform the matching on downsampled imagery as a tradeoff of

localization to improve repeatability. Sub-pixel LSM on downsampled images may compensate for some loss in localization.

In an iterative approach to this algorithm, it is advantageous to consider dense tie point generation techniques in preparation for robust surface generation once the image geometry has been adequately reconstructed so that the search space is greatly reduced. Classic approaches to the problem usually involve image resampling so that the epipolar lines lie along the rows of each image, allowing rapid densification using NCC. There are a variety of methods available in the modern literature with varying claims of success ranging from computer vision techniques employing video imagery [Jung and Lacroix, 2003] to robust diffusion techniques [Stretcha et al., 2003].

Bundle Adjustment

The simultaneous bundle adjustment is a technique for the optimal estimation of the camera and scene geometry parameters. It is formulated as a linearized least squares implementation of the collinearity equations. It may also be extended to include the interior orientation parameters, in which case it is referred to as the self-calibrating bundle adjustment. The bundle adjustment is jointly optimal in the sense that it serves to optimally estimate both camera and scene parameters by applying a geometrically consistent model of the image formation [Wolf and Dewitt, 2000]. In a general sense, this is what makes the bundle adjustment a robust estimator, since the physical behavior of light imposes a strict model of the position and orientation of a camera which will produce a given image of a scene. The optimality of the estimation is given by the employment of a least squares. The least square technique is optimal for linear system because it seeks to minimize the quadratic error of the parameters in fitting the model, and can be extended by linearization of the model to optimally solve for nonlinear systems given sufficiently accurate initial approximations. The term ‘bundle’ refers to the

‘bundles of light’ that form the camera images, which denotes the ability of the technique to optimally solve for ‘bundles’ arising from more than one camera.

A special consideration is to be made in the application of the bundle adjustment for direct georeferencing. In traditional photogrammetry, control points that exist in the object space serve as the primary control to the absolute orientation. In direct georeferencing, the only measure of absolute orientation are the parameters provided by the navigation system. Considering that the bundle adjustment solves for the best relative geometry of the scene, the absolute accuracy of the final adjustment is in question. It can be supposed that the bundle adjustment will tend to produce parameters which are an internally consistent geometry for the images due to the strength and redundancy of the image coordinate observations, and therefore accurate in the relative sense. The absolute accuracy of the object space coordinates, or accuracy of the scene and image features with respect to the local-level coordinate system, however, would act only as a weak constraint on the solution given the relatively poor accuracy of the direct georeferencing parameters.

This is best illustrated with respect to the vertical position of the scene geometry. Given that the altitude provided by the navigation system is likely biased (see Chapter 4), it is possible that the bundle adjustment will produce an internally consistent scene geometry which is in absolute error equal to the bias of the altitude. This is not to say that the solution will not be an optimal estimator of the absolute position; in fact, if all observations are properly weighted and the direct georeferencing parameters are normally distributed about the true value, then it indeed should be optimal. However, the possibility of biased measurements at least forewarns the risk of poor solutions in the absolute sense. This consideration is less important in the case of two-dimensional mapping, since the reasonably accurate horizontal navigation parameters and well-

known focal length will tend to produce a strong estimate of the object space scale and orientation.

The accuracy of a self-calibrating bundle adjustment in solving for the interior orientation parameters has not been evaluated for the direct georeferencing technique presented in this thesis, and its use is cautioned. It is not initially apparent that the addition of internal orientation parameters would lead to over-parameterization of the problem, since as was noted earlier the degrees of freedom in the typical problem addressed by this thesis is on the order of thousands. In such a case, how could the addition of just a few unknown parameters affect such a problem? The answer is that the internal orientation parameters are highly correlated to other parameters in the solution [Cramer, 2002]. For example, the focal length is highly correlated to the Z parameter of the exterior orientation, the flying height. The effect of this correlation on the absolute mapping accuracy of NOVA II data set has not been empirically verified.

Two additional factors are noted that would discourage the use of the self-calibrating bundle adjustment for the NOVA II platform. The first is the relatively high noise of the measured parameters, both from low-quality navigation systems and also from automated tie point matching. Low signal to noise ratios may cause the SCBA to model noise as higher-order distortion parameters. The second factor is the low solution inertia caused by poor approximations of the object space coordinates based on a constant-surface assumption. By introducing additional parameters, the number of critical points in the solution space is increased. With poor initial approximations, the possibility of convergence on a suboptimal solution is thereby also increased.

Although not incalculable, the size of the matrices generated by the bundle adjustment for these data sets is of concern for calculating speed [Triggs et al., 1999]. Keeping in mind, of

course, that it is an iterative algorithm that requires a number of passes to converge on a solution. However, several factors lend themselves to improving the situation. First, the sparsity of the normal matrices as well as the ability to directly compute them using partitioned matrices lends itself to a significant amount of algorithmic and computational optimization. The sparsity of the matrix allows efficient use of memory during computation. In addition, the bundle adjustment normal equations are symmetric positive definite matrices for a well-formed data set, allowing efficient factorization methods to be employed for solving the bundle adjustment [Golub, 1996].

A development of both the standard and self-calibrating bundle adjustment is given in Appendix C. The solution of the bundle adjustment is given by iteration, solving for the update vector in Equation 5-14 and updating the initial approximations at each step. This is the Gauss-Newton method for the solution of non-linear systems. It should be noted that the Gauss-Newton method suffers from the possibility that the solution will not converge because a particular update vector ‘overshoots’ and produces a less accurate solution. If this occurs, it is possible to employ a damping factor to the normal equations. This technique is widely implemented as the Levenberg-Marquardt algorithm, Equation 5-11.

$$(N + \lambda \text{diag}(N))\Delta = K$$

λ = Marquardt (damping) parameter

(5-11)

There are several methods in the literature about methods for the selection of the damping parameter λ [Roweis, 2009]. At each iteration, the sum of the squared residuals is calculated and compared to the previous iteration. If the error is smaller, the assumption is made that the solution is improving, and the update from the current iteration is accepted and updated. Accompanying this assumption is the insight that, since the iterations are converging on the correct solution, it is best to ‘speed up’ the gradient descent rate to get to the solution more

quickly. To do this, the damping parameter is decreased by some factor. In the converse situation, where the solution worsens with an iteration, we should ‘slow down’ the solution so that we more closely follow the gradient. To do this, the damping parameter is increased by a factor to decrease the gradient descent rate.

Understanding the impact of the LM algorithm is eased when considering that when the value of $\lambda \text{diag}(N) \rightarrow 0$, the solution will be the same as the Gauss-Newton method.

Alternatively, if the Levenberg formulation in Equation 5-12 is used, then as $\lambda \text{diag}(I) \rightarrow \infty$ the update becomes approximately $\frac{K}{\lambda}$, getting much smaller and in the direction of the gradient of K. The extension of Levenberg’s formulation by Marquardt to replace the identity matrix with the diagonal of the Hessian, N, which allows the algorithm to effectively weight the update in the direction of the smaller gradients. This improves the ability of the algorithm to escape sub-optimal solutions and also increase the rate of convergence [Raweiss]. An important note on the theory of the LM is that it is purely a heuristic method and does not ensure optimality in the selection of the damping parameter. Thus, the selection of the factor by which to increase or decrease the damping factor is a matter of practice and not theory.

$$(N + \lambda \text{diag}(I))\Delta = K$$

I = Identity matrix

(5-12)

Surface Generation

The scene modeling step uses the adjusted tie point object space coordinates to produce a surface model of the scene for the entire area covered by the mosaic. The algorithm developed for the NOVA II uses the constant surface assumption, and therefore this step is simplified to merely calculating the average height of all tie points in the solution. This assumption is suitable for mapping in areas with very little terrain height variations and low vegetation coverage

relative to the flying height. However, great potential lies in extending the algorithm to handle 3D scene modeling. The scene modeling process is most often implemented as digital terrain model generation. If a bare-earth model is developed to remove the relief due to vegetation and anthropogenic features, the process is called digital surface modeling.

The automatic generation of a digital terrain model of comparable quality to a LiDAR-generated model has been demonstrated on a low-altitude mini UAV platform [Eisenbeiss and Zhang, 2006]. Albeit somewhat larger than the NOVA II and using ground control for the bundle adjustment, this serves as the proof-of-concept using similar equipment, generating a DEM consisting of 4.7 million tie points at a resolution of 10 cm. The reported mean difference between the LiDAR and photogrammetrically generated scene models was less than one centimeter with a standard deviation of 6 cm. Moreover, the use of direct georeferencing on larger platforms is used in commercial operations for DEM generation, indicating that the direct georeferencing accuracy will be the only limiting factor, if at all [Yastikli and Jacobsen, 2002].

The scene modeling procedure essentially depends on the output of the tie point procedure. Whether using bundle-adjusted tie points or post-adjustment densification of the tie points, the generation of a DEM is essentially a matter of interpolation of the irregular observations of the object space coordinates. Interpolation is required to provide the elevation value for each groundel in the output. Therefore, the discussion proceeds with a discussion of two relevant methods of surface interpolation, the inverse distance weighted interpolation and the Kriging surface interpolation.

The inverse distance weighting method, Equation 5-13, is a straightforward approach to surface interpolation. The basic idea is that for every unknown point of interest on the surface, the elevation is calculated by taking a weighted sum of the elevations of nearby points. The

weighting function allows control over the smoothness of the interpolation. The primary drawback of the IDW is the tendency to produce ‘bullseye’ artifacts as in Figure 5-2, since the method has no mechanism for accounting for trends in the elevation, such as a ridge line. As a result, a sharp linear ridge in the scene will appear as a linear series of peaks in the interpolated surface.

$$\begin{aligned}\hat{z}(x_p, y_p) &= \frac{\sum_{k=0}^N w_k(x_p, y_p) Z_{I_k}}{\sum_{k=0}^N w_k(x_p, y_p)} \\ w_k(x_p, y_p) &= \frac{1}{\left(\sqrt{(X_I - x_p)^2 + (Y_I - y_p)^2}\right)^S}\end{aligned}\tag{5-13}$$

A smoothing parameter, S , operates such that values $0 < S < 1$ will decrease the relative weight of nearby points and thereby reduce the ‘bullseye’ effect. Decreasing the number of points, N , used for the interpolation allows increasing localization of the interpolation from N being all tie points to some subset of points. The N tie points are selected by a threshold Euclidean distance from the target point. The advantage of the IDW is its simplicity, which allows the algorithm to be easily processed automatically.

A more advanced DEM generation method is the Kriging interpolation technique. There are several forms of the Kriging, and the one described here is the ordinary Kriging, which assumes there is some constant but unknown mean elevation value and a known spatial dependence (covariance) based on an experimental variogram. It is a least squares estimator which attempts to find an unknown elevation as the weighted linear sum of observed elevation values where the weights are chosen such that the prediction error for observed values is minimized. The Kriging relies upon the assumption that the elevation is a dependent variable of the spatial position, a reasonable assumption for most types of natural terrain. The spatial

dependence of the elevation is quantified by a stochastic model given by the experimental variogram, which must be modeled by the observed tie points. The Kriging equation is given by Equation 5-14, where the weighting value w_k for each $p = [x_p, y_p]$ is given by least squares solution of Equation 5-15.

$$\hat{z}(x_p, y_p) = \sum_{k=0}^N w_k(x_p, y_p) Z_{I_k}, \quad (5-14)$$

$$\begin{bmatrix} \gamma(I_1, I_1) & \cdots & \gamma(I_n, I_1) & 1 \\ \vdots & \ddots & \vdots & \vdots \\ \gamma(I_1, I_n) & \cdots & \gamma(I_n, I_n) & 1 \\ 1 & \cdots & 1 & 0 \end{bmatrix} \begin{bmatrix} w_1 \\ \vdots \\ w_n \\ \mu \end{bmatrix} = \begin{bmatrix} \gamma(I_1, p) \\ \vdots \\ \gamma(I_n, p) \\ 1 \end{bmatrix}$$

$$I_n = [X_{I_n}, Y_{I_n}]$$

$\mu = \text{Lagrange multiplier}$

$$(5-15)$$

The variogram function, to emphasize again, is modeled from observed values. This is necessary because the variogram is discontinuous for a discrete set of observed values, and must itself be interpolated. The experimental variogram maps the covariance of a data set as a function of the difference between two points evaluated at a point, given by Equation 5-16.

$$\gamma([X, Y], [x, y]) = \frac{1}{2} \mathbb{E}[(Z(x, y) - Z(X, Y))^2] \quad (5-16)$$

A mathematical model used to fit the variogram is necessary and usually either a linear, exponential, or spherical model as given in Equation 5-17. [Cressie, 1993]

$$\gamma_{linear} = \begin{cases} 0 & h = 0 \\ c_0 + c_l h, & h \neq 0 \end{cases}$$

$$\gamma_{spherical} = \begin{cases} 0 & h = 0 \\ c_0 + c_s \left(\frac{3}{2} \left(\frac{h}{a_s} \right) - \frac{1}{2} \left(\frac{h}{a_s} \right)^3 \right), & 0 < h \leq a_s \\ c_0 + c_s & h \geq a_s \end{cases}$$

$$\gamma_{exponential} = \begin{cases} 0 & h = 0 \\ c_0 + c_e \left(1 - \exp \left(-\frac{h}{a_e} \right) \right), & h \neq 0 \end{cases}$$

$$(5-17)$$

For each model, the variable c_0 is called the ‘nugget’ and is the apparent y-intercept of the experimental variogram and is usually caused by noisy measurements [Cressie, 1993]. The linear model is completed by c_l , equal to the slope of the line. The spherical and exponential models include the variables a_s and a_e , respectively, which are the ‘range’ parameters, equal to the distance at which the terrain is no longer dependent. The spherical and exponential models include a dependent parameter known as the sill, equal to $c_o + c_s$ and $c_o + c_e$ for the respective models, which is the value the variogram converges on as distance increases. In order for the Kriging to be fully automated, the estimation of these model parameters must also be automated. This is accomplished by a least squares approach to the model fitting [Cressie, 1985].

Mosaicing

Three-dimensional models are not generally needed for aerial remote sensing applications. The preferred method of using this type of imagery is to reproject the image onto a two-dimensional surface. If this projection is orthogonal to the mapping plane, an orthophoto is produced. The mathematical formulation of the orthogonal projection, given in Equation 5-18, is straightforward. Applying the orthogonal projection to the object space coordinates, the output simply corresponds to the object space coordinates with an arbitrary (or zero) elevation.

$$\begin{bmatrix} X_I \\ Y_I \\ 0 \end{bmatrix} = P \begin{bmatrix} X_I \\ Y_I \\ Z_I \end{bmatrix} = \begin{bmatrix} 1 & 0 & 0 \\ 0 & 1 & 0 \\ 0 & 0 & 0 \end{bmatrix} \begin{bmatrix} X_I \\ Y_I \\ Z_I \end{bmatrix} \quad (5-18)$$

An orthophoto constructed from an ideal scene reconstruction will remove all perspective geometry and the scene will be viewed from a uniformly infinite vertical perspective. This has the effect of removing all relief displacement from the image. For example, the vertical sides of a building will not be visible. Because of this, any area of the image which is occluded from the perspective view will result in ‘gaps’ in the output orthophoto. Orthophotos produced using the

regularly-spaced pixels common to digital image formats have the extremely useful property of allowing each pixel to have a uniform scale.

Mosaicing is an extension of the orthophoto production process, where multiple images are combined into a single orthogonal projection to produce a composite map. This final step in the process is perhaps the most important, where we arrive at the georeferenced image output. As discussed, the orthogonal projection of images produces a two dimensional map where each pixel covers an approximately equal area on the ground and where the image rows and columns correspond to east and north directions. The approximation is due to the error associated with representing the ellipsoidal surface of the earth using a rectangular grid.

Although other approaches are possible, the technique for mosaicing presented here is designed to exploit the type of imagery collected by the UAV. That is, the imagery tends to have high amounts of overlap and therefore redundancy, and also to minimize the effect of the constant-terrain assumption. Because a constant terrain assumption is used, true orthophotos are not produced unless the terrain is actually flat. An accurate three-dimensional surface model as described in the previous section is required for true orthophotos. Rather, the correct term for the process used here is rectification. That is, the effect of image tilt is removed from the image but any vertical relief remains uncorrected. Since the majority if not all areas of a NOVA II mapping area have stereoscopic coverage, there is the necessary step of choosing the best source image from which to select each groundels radiometric information. There are three considerations.

- **Radiometric quality** is highest along the optical axis due to consistent illuminance, shortest-path travelled, and minimal color distortion due to lens aberrations
- **Geometric quality** is highest at the nadir, where the projection error due to incorrect image parameters is minimized
- **Vertical relief error** is minimized by selecting from the image with the nearest nadir, best approximating the orthogonal projection

Because we are using a constant terrain surface assumption, perhaps the most difficult consideration in the usual orthophoto production can be neglected. That is, where a particular area is occluded in an image due to terrain relief, it is necessary to use an adjacent image in which the occluded area is visible. Using the constant surface assumption, terrain relief error is directly transferred to the output image but is assumed to be small.

The mosaic process proceeds by calculating the constant surface intercept of the nadir of each image, and then for each pixel in the output mosaic the image with the nearest Euclidean distance to the nadir and which contains the target pixel is selected. The object space position of the output pixel is then projected up to the image using the collinearity equations to find the corresponding pixel and color values. In the implemented algorithm, a nearest-neighbor approach is used; whichever pixel contains the object space point is selected. The nearest-neighbor approach is both the most computational efficient and also most suitable for remote sensing classification, since it does not modify the original color information. However, given that it is rare for an object space coordinate to correspond precisely to a single pixel, a more visually appealing results may be obtained by using interpolation techniques about adjacent pixels (Figure 5-3).

Two notable interpolation techniques for the resampling process are the linear and cubic interpolation technique. More advanced techniques such as those described in the scene modeling step are impractical for the computational intensive process of resampling, and these basic techniques are more than adequate. Linear interpolation techniques are well known and will not be repeated here. Linear interpolation has the advantage of being less computational efficient than the other common technique, cubic spline interpolation, but is disadvantaged

because it acts as a low-pass filter, reducing high-frequency detail in the output image [Parker et al., 1983].

Cubic spline interpolation, given in Equation 5-19, employs an approximation of the sinc function as a weighting function for the interpolation. This is important because convolution of the sinc function over a discrete data set that was sampled to meet the Nyquist criteria will exactly reconstruct the original signal.

$$f_{\text{spline}} = \begin{cases} (a + 2)x^3 - (a + 3)x^2 + 1 & 0 \leq x \leq 1 \\ ax^3 - 5ax^2 + 8ax - 4a & 1 \leq x \leq 2 \end{cases}$$

a = desired slope of the function when x equals one
x = absolute distance from the image coordinate to the source pixel

(5-19)

The selection of the free parameter *a* for the cubic spline function is limited to the range of -0.5 to -1 for a good approximation of the sinc function. Typically, the value is selected to be -0.5 which will exactly reproduce quadratic source signals [Wolf and Dewitt, 2000]. Alternatively, values up to -1.0 can be used which progressively amplifies frequencies approaching the stopband and results in more high-frequency information content passing through [Parker, 1983].

Software Implementation

The algorithm was implemented in the Python version 2.6 [Van Rossum]. Python was chosen for implementation due to a rich and open source library of numerical, image processing, and parallelization algorithms. The software was executed from a plain-text script file which allows direct adjustment of the algorithm parameters as well as access to individual processing steps. The algorithm was organized within the `pyGeomatics` Python package. The remainder of this section describes the complete algorithmic flow for a single iteration of the algorithm.

The process was initialized with the directory path of the data and the calibrated focal length. The data log file was processed, during which the image geotags were interpolated from the associated navigation and synchronization packets. If a manually selected subset of the images was desired, it could have been specified in a list. Otherwise, the valid images were automatically selected using the criteria specified in the preprocessing section and the constant surface height was calculated. The boresight and leverarm calibration are applied to the geotags, and the geodetic latitude and longitude values were converted to the appropriate UTM coordinate system using the `pyproj` library which exposes Python bindings for the PROJ.4 library [Evenden]. Two variables are returned, containing an ordered list of the image direct georeferencing parameters and a dictionary of the image file names.

The radiometric preprocessing proceeds by downsampling, grayscaling, and equalizing the histogram for each pyramid level. This process was completed using functions available in the OpenCV library [OpenCV, 2001]. The generated images are saved to a new subdirectory in the source data directory. An optional step at this point was to directly project the images with a specified resolution using the uncorrected exterior orientation parameters. Otherwise, the algorithm proceeds with the automated tie point generation.

The tie point generation algorithm implements the HCD available in the OpenCV library. An edge mask was applied to the image to ensure sufficient space around the potential tie points for the desired template window. The number of unique tie points per image was specified, usually a value between 5 and 15, and a minimum separation distance between tie points was also provided as a percentage of the image width. The HCD sensitivity parameter κ and the kernel size were also required. A kernel size of 11 and the default sensitivity of 0.04 were found to be effective. A relatively low quality threshold, 0.2, was found to be sufficient to reject low-

quality features such as open areas of water. The initial approximation of the object space coordinates of the potential tie points was then calculated. The tie point generation process returns two more variables, an unordered nested list of image coordinate observations and an ordered list which contained the object space initial approximations. Each image coordinate observation was associated with the image index and tie point index from their respective ordered lists.

The next procedure was to generate the initial approximations of the object space boundaries of each image in preparation for the tie point matching step. This returned an ordered, nested list of the image boundaries. For each tie point, a list of overlapping images was generated by evaluating whether the object space approximation of the tie point was within the polygon defined by the approximated image boundaries. The nested list of overlapping images for each tie point was then returned.

The tie point matching algorithm allowed the image pyramid level to be used for matching to be specified, as well as the template window size and the search window size. A minimum value for the normalized cross-correlation can be provided, but was not used due to the subsequent manual filtering step. The tie point matching algorithm proceeded by finding the maximum NCC for the log-polar transformed template and target windows within the search space. The center of search space was determined by the ‘Project Up’ Equation 2-10 using the initial approximations generated during the tie point generation step. The best match found was then presented to the user to either be accepted or rejected. Each successfully matched tie point was added to the list of image coordinate observations, which was returned at the conclusion of this procedure. Optionally, at this point the matched tie points can then be manually reviewed a second time using the full-color source images and poor matches rejected (Figures 5-4 and 5-5).

Because not all of the potential tie points will ultimately be matched, it was necessary to then calculate the observational redundancy of each tie point. Tie points which do not have at least two observations were then scrubbed from the list of tie points, as well as the associated image coordinate observation. This completes the generation of all necessary data for the bundle adjustment process. At this point, the generated data set was exported to a text file for inspection or for future reuse, with facilities provided for reloading previously generated data sets. A formatted data file for the bundle adjustment was also generated using specified observation weights and saved to the source directory.

The bundle adjustment algorithm was a self-contained module within the `pyGeomatics` package. A function was called to load the desired data set from a file, and a number of internal data structures are generated. For each iteration of the bundle adjustment solution, the normal equations were generated as described in the bundle adjustment section. The `NumPy` and `SciPy` libraries were used for optimized numerical computation facilities, and sparse-matrix storage of the normal equations and the optimized linear algebra solution algorithm was provided by the `PySparse` library [Geus and Arbenz, 2003]. It is again noted that the current implementation was restricted to the regular bundle adjustment and did not include the interior orientation parameters or boresight and lever arm parameters in the adjustment. The bundle adjustment was optionally solved using either a standard least squares approach or the Levenberg-Marquardt technique. The standard deviation of unit weight was calculated and output at each iteration. The direct solution was usually used and provides satisfactory convergence. The adjusted exterior orientation parameters and tie point object space coordinates were saved to an output text file. The variables containing the image exterior orientation parameters, tie point object space coordinates, and image observations were updated with the adjusted values.

It is at this stage of the algorithm that the surface generation technique should be implemented in future development. As discussed previously, this step was simplified by the constant surface assumption to simply taking the average tie point height. In preparation for the mosaicing process, the object space image boundaries were recalculated and updated using the new surface and adjusted EOPs.

The final step in the algorithm was the mosaicing process. The algorithm allows the user to specify the extents of the generated mosaic, or to automatically calculate the full extents using the image boundaries. The mosaic was generated as a set of subset images, tiles, with a specified number of pixels in order to reduce individual file sizes. The resolution of the output image can either be specified or automatically calculated as the minimum size of a projected groundel for the data set. As described, the source of each output pixel was selected by finding the image with the nearest nadir. The algorithm does not currently implement pixel interpolation in the resampling procedure. The mosaic tiles and an associated world file were generated which contained the image georeferencing parameters using the ESRI specification [World File, 2008]. In addition, a routine was run to automatically parse the directly projected or mosaic tile images world files to convert them to the .KML format compatible with Google Earth [KML, 2009].

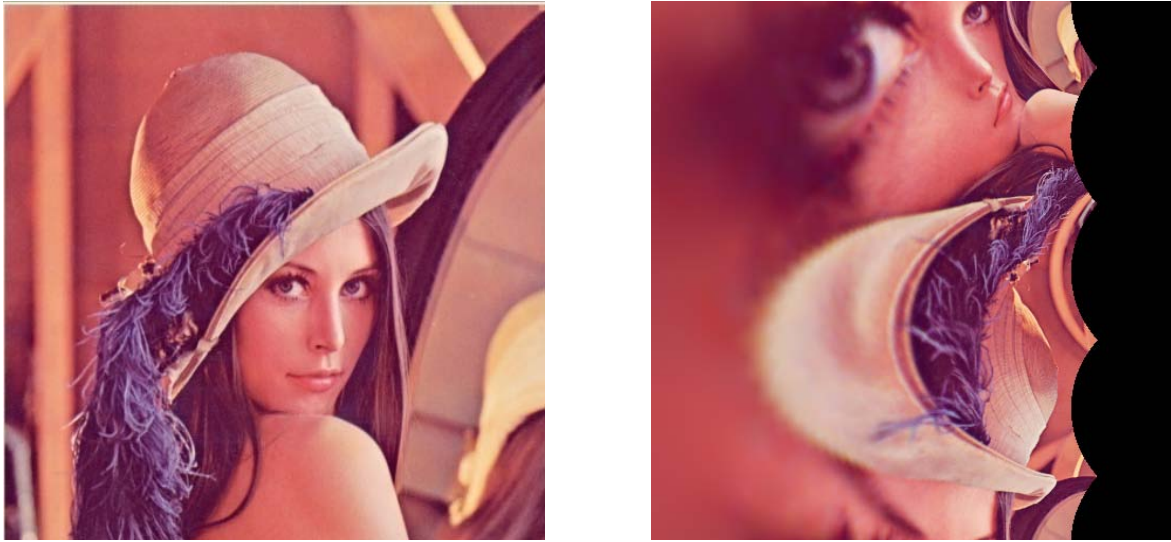


Figure 5-1. Example of the Log-Polar Transformation. The origin of the transform is the center of the source image with $M = 72$, Source: [Lena]

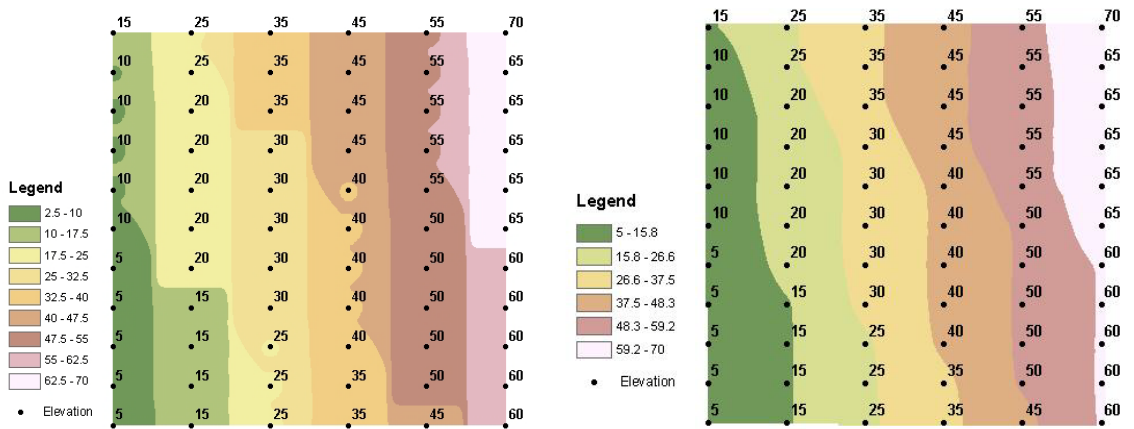
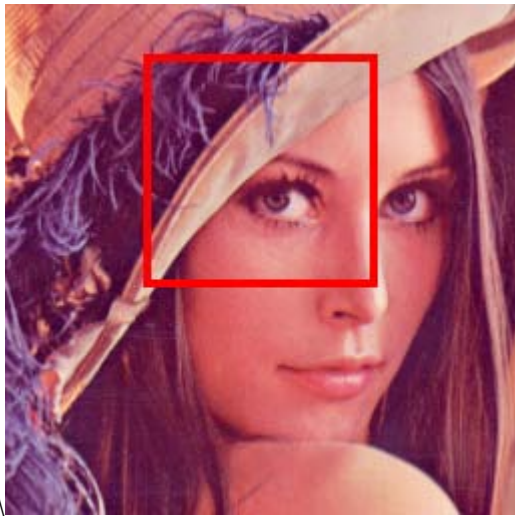


Figure 5-2. Comparison of IDW (left) and Kriging (right) interpolation techniques demonstrating the ‘bullseye’ effect of the IDW



Original



None



Linear



Cubic Spline ($a = -0.5$)

Figure 5-3. Comparison of resampling techniques at 200% enlargement, Source: [Lena]

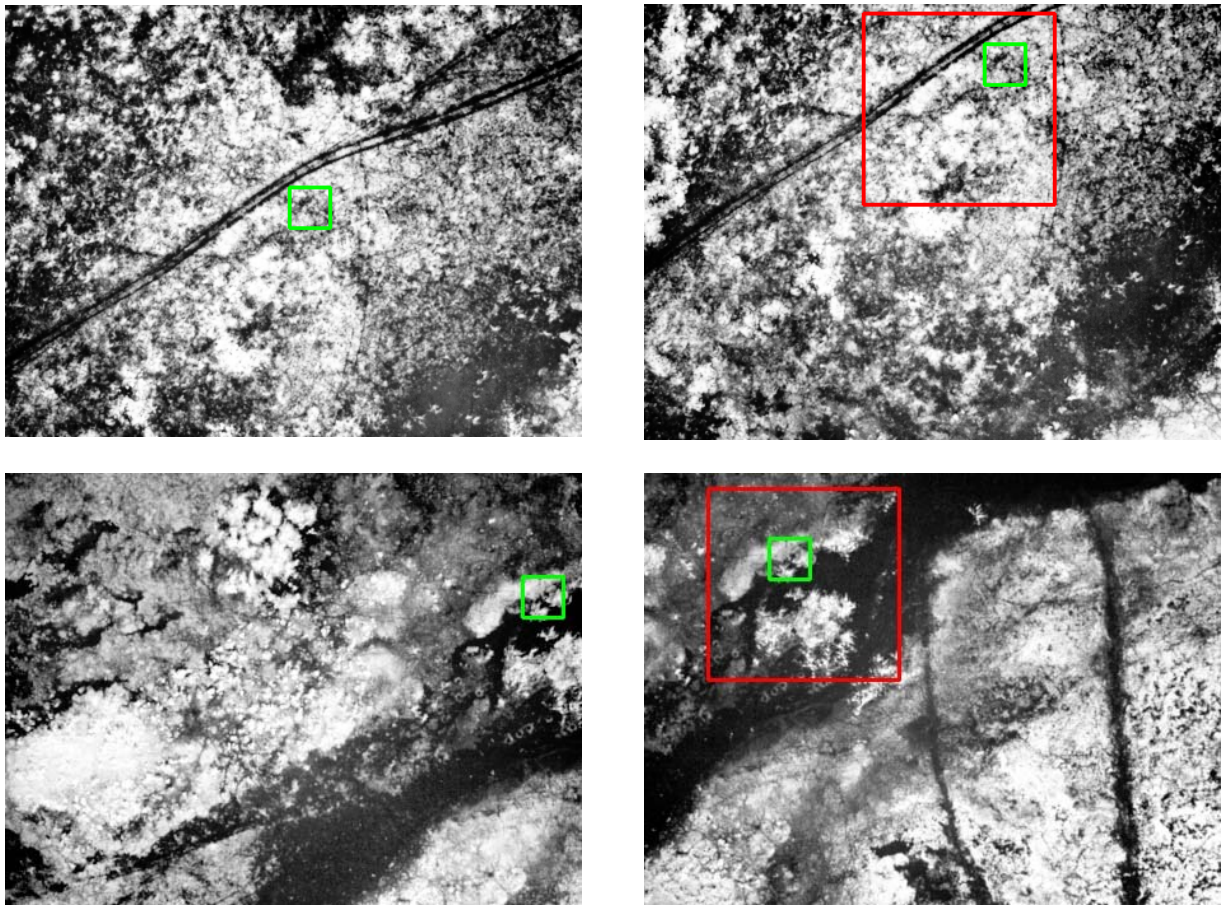


Figure 5-4. Example correct tie point matches between source (left) and target (right) images, matched template in green and search space in red

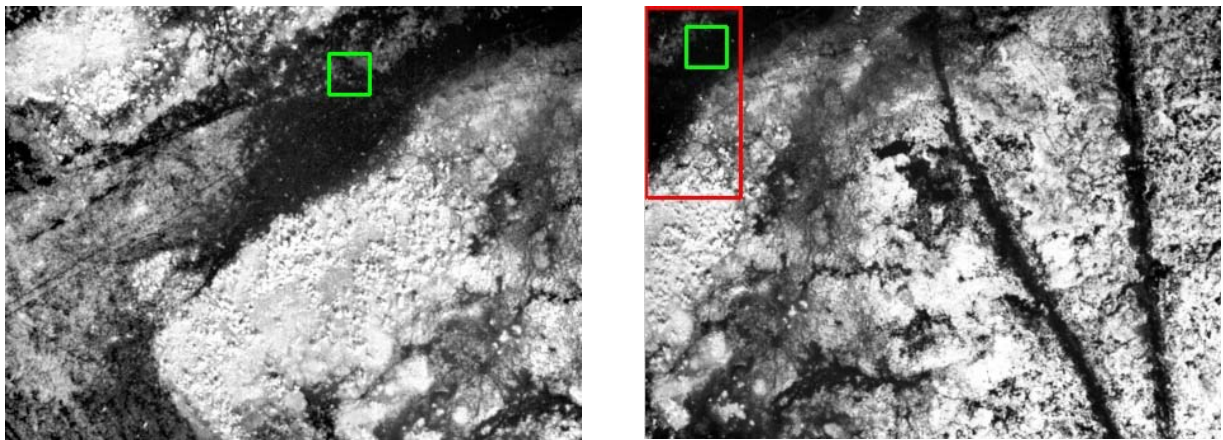


Figure 5-5. Example of an incorrect tie point matches due to poor initial approximation of the image boundary, matched template in green and search space in red

CHAPTER 6 ASSESSMENT AND CONCLUSIONS

Assessment

The goal of the assessment was to evaluate the relative accuracy of the output mosaic (Figure 6-3) by measuring the image-to-image agreement of the location of features within the data set. This assessment was limited by the fact that ground truthing values were not available. However, the assessment reflects both the actual operating conditions that the NOVA II platform is designed for, as well as evaluates the output from the standpoint of its intended use. The calibrated focal length obtained in the camera calibration described in Chapter 4 was used. The boresight and leverarm correction was estimated from the physical mounting. The lack of a refined calibration for the full interior orientation parameters and boresight and leverarm parameters suggests that these results are conservative estimates of the overall accuracy of the system, and should be considered a rudimentary measure of the system's potential.

The data set used for this adjustment was selected randomly from a typical NOVA II mission. The average flying height above the terrain was about 160 m (commanded flying height of 150 m) and the average flight line spacing was approximately 72 m with a target airspeed of 23 m/s and a prevailing wind speed of approximately 3.5 m/s. The data was collected under clear sky conditions at approximately 11:00 AM on April 23, 2009, for a total flight duration of approximately 35 minutes. Twenty-seven images were selected from the upwind portion of the dipole flight pattern. The output mosaic was generated for an area of 40,000 sq. m. at a resolution of 2.5 cm centered within the coverage area.

The algorithm described in the software implementation of Chapter 5 was employed directly, with no manual intervention of the process except during the specified manual matched tie point filtering step. The data set was processed twice, the first using a smaller set of tie points

to generate a somewhat improved estimate of the EOPs so that the subsequent processing step had improved initial approximations. For both bundle adjustments, the original EOPs provided by direct georeferencing were used as the initial approximations; only the tie point observations varied between adjustments.

A standard methodology was developed for evaluating the relative accuracy of the mosaic. For each image, the perimeter of the image was traversed and approximately every 912 pixels (1/3 of the height and 1/4 of the width) a matchable feature was selected. This evaluation was completed using both the adjusted and unadjusted EOPs. The error distance was measured to the same feature in each immediately adjacent image. This process was completed using individual image projections to evaluate the accuracy of the full extent of each image. It was expected that the error would be greater as distance from the nadir increased. Because the mosaicing process compensates for this effect, it was of interest to compare the ‘edge’ accuracy to the mosaic ‘seam’ accuracy. To this end, the mosaic itself was analyzed by traversing each mosaic seam and selecting a matchable feature every 10 m. Because of errors in projection and terrain relief, some features along the seam were immeasurable due to occlusion, and these seam locations were excluded from the analysis.

The first iteration of the algorithm projected the images to a constant surface using the EOPs provided directly by direct georeferencing. The unadjusted edge error had a mean of 9.8 m and a standard deviation of 4.3 m. The tie point matching algorithm was performed on the twice-downsampled images and resulted in 112 successful tie point matches, 26 (19%) potential tie points matches that fell outside of the target image due to the initial approximation error, and 13 (9%) tie point matches which fell within the target image but were incorrectly matched. The

overall success rate of the tie point matching algorithm for the first iteration was 72%. The bundle adjustment was then completed using the first iteration tie points.

The second iteration of the algorithm used the solved EOPs of the first bundle adjustment for initial approximation of the tie point matching algorithm operating on the once-downsampled images. This resulted in a total of 295 successful tie point matches. The number of potential tie points which were outside of the target image was 28 (7%) and the number of incorrectly matched points was 42 (12%) for an overall success rate of 81%. The increased success rate was clearly due to better initial approximations of the search space and image extents. It should be noted that for both the first and second iteration, no tie point matches failed due to an insufficient search space; the manual selection of the search space based on a priori estimates of the navigation accuracy proved to be an effective method. The increase in the number of mismatched points is likely attributable to the move from twice- to once-downsampled images, which necessarily decreased repeatability as discussed in Chapter 5. The distributions of tie points from the first and second iteration are compared in Figure 6-1. The results of the second bundle adjustment are shown in Table 6-1.

The edge accuracy of the adjusted images was found to have a mean error of 0.50 m with a standard deviation of 0.31 m, nearly an order of magnitude of improvement over naïve direct georeferencing. No significant correlation was found between the number of tie points in an image and the image edge accuracy. The mosaicing seam accuracy assessment gave a mean error of 0.37 m with a standard deviation of 0.21 m, an improvement over the edge accuracy as was expected. The distribution of the mosaicing seam errors is shown in Figure 6-2.

Conclusions

The research and development presented in this thesis has demonstrated the feasibility and perhaps even the practicality of developing a true directly georeferenced remote sensing system on a small UAV platform. The most significant contribution of this thesis is the systematic development of a technique in which each element of the direct georeferencing process is based on an empirical model. The result is a system which produces mapping products with a predictable error budget based on the contribution of quantifiable errors from the individual elements of the technique. Given this advance, it is now possible to systematically review and improve individual components of the technique until the desired mapping accuracy is reached, within the physical limitations of the platform and sensing hardware.

In the development of an empirical approach to directly georeferencing remote sensing on small UAVs, a strong contrast has been drawn with alternative approaches. Surveying the literature on aerial mapping technique for small UAVs, there has not been a shortage of attempts. However, this approach does not suffer the shortcomings from incorrect camera models [Taylor, 2008; Xiang, 2007], it does not rely on unrealistic image warping methods [Mujambar, 2004; Ilstrup, 2008], and it does not require preexisting imagery [Zhu, 2005]. The technique does not require ground control points or extrinsic scene models, neither of which are currently possible within the scope of the platform or mission profiles [Ladd, 2006; Grenzdörffer, 2008; Nagai, 2009; Eisenbeiss, 2006].

The synthesis of this technique overcame other limitations of directly georeferenced remote sensing implementation on a small, inexpensive UAV as discussed in Hruska [2005]. Employing and integrating a suite of consumer off-the-shelf sensors proved to be a practical and cost-effective approach, requiring only a single custom synchronization component.

Interestingly, the Burredo proved to be the most accurate synchronization system among the other published approaches in direct georeferencing despite its low cost and simple design. Utilizing standard computer hardware and interfaces allowed for rapid development of a flexible architecture open to modification with additional sensors or data collection features. Finally, the processing algorithm was written with, and utilized only, open-source tools, helping to ensure compatibility with future development.

Importantly, the synthesis of existing techniques also allowed for concise treatment of the most significant problems identified in previous direct georeferencing approaches [Skaloud, 1999]. Despite the greatly reduced accuracy and quality of the sensor suite on the NOVA II platform when compared to surveying-grade, manned-aircraft systems, many elements of existing direct georeferencing techniques had parallels on the UAV platform. This was particularly evident in the calibration of the payload, where the methods for camera and boresight/leverarm calibration proved feasible. To this end, a permanent installation for the future calibration and accuracy analysis was established at the University of Florida Lightning Lab (Appendix B).

In terms of final mosaic accuracy, the processing algorithm is arguably the most important element of the new technique. The algorithm, although synthesized from existing methods, made use of a sensor fusion approach allowing for a robust and efficient processing method. In particular, the application of the bundle adjustment to the directly georeferenced observations served to increase the mosaicing accuracy by better than an order of magnitude. Despite this, the algorithm remains open for significant improvement, particularly in terms of the algorithmic efficiency. The sheer amount of data collected in a single flight proved to be more than could be reasonably processed using the technique and algorithm on an operational basis. The mosaic

generated in the accuracy assessment, consisting of only 27 images, and took approximately 6 hours on a modern laptop computer to process.

The resolution of the system is obviously of great importance to the overall goal of the NOVA II project. Figure 6-5 provides some examples of the quality of imagery obtained from the NOVA II platform. Groundel sizes of 2.5 cm or less are achievable on this platform while still maintaining sufficient overlap for 2D mosaicing. A baseline assessment for the quality of the imagery required for the operational scope of the NOVA II discussed among those involved in the project was the reliable identification of small targets. The reliable identification of various ecological targets proved to be well within the capability of the system, and future improvements to optical sensors will augment the capability.

Recommendations

It is not entirely predictable whether the most significant gain in accuracy will be achieved by improving the sensor accuracy, calibration quality, or the robustness of the processing algorithm. Initial emphasis should be placed on calibration quality since it requires minimal resources for maximum returns. A full calibration of both the camera and boresight and leverarm at the Lightning Lab site should be completed and analyzed for improvements. With respect to the calibration procedure itself, the most feasible modification would be to integrate both the camera and boresight calibration into a single procedure, allowing for a more efficient calibration process in the future. Beyond this, a radically different approach to calibration would be to integrate the calibration procedure into the data collection process itself by employing a self-calibrating bundle adjustment on the data without the use of ground control points. Such an approach is unproven, but is certainly worthy of investigation. However, as discussed in Chapter 4, the effect of cross-parameter correlation in both the proposed alternative procedure is not clear and should be evaluated.

Improvement of the sensor suite is feasible, but is strongly constrained by the limitations of the small UAV platform. Two areas of improvement that will have a significant impact on the accuracy are foreseeable in the near future. The first is in improving the accuracy of the GPS system. In particular, moving to differential (ground station based) and dual-frequency GPS should result in an order of magnitude improvement in the absolute position error of the navigation system [Misra et al., 1999]. Given that the GPS serves as the primary control in the algorithm's adjustment procedure, this is expected to have the largest impact on the final accuracy among sensor improvements. Currently, the primary deterrent to installation of geodetic-grade GPS on the NOVA II is the weight of the antenna, which is relatively bulky. The second improvement would be to install a single-beam EDM device on the aircraft. Such a device would depart from the passive sensor approach currently employed on the NOVA II platform, and would add very useful data. This approach has been successfully employed on small UAV platforms for Z-ambiguity estimation, and serves to add an empirical measurement of the actual image-to-object space correspondence [Zhu]. This addition would allow significantly more robust initial approximation procedures by allowing for a stronger estimate of the Z-ambiguity, even with only a single ranging observation per image.

The processing algorithm is certainly leaves room for improvement, as discussed throughout its development. First and foremost, the efficiency of the algorithm must be improved. This is largely possible through the development of parallelized algorithms for the tie point matching and mosaic generation procedures. Both are ‘embarrassingly parallel’ problems, which allow for efficient distribution among an arbitrary number of processors and could be scaled to as large of a system as needed. In addition, the costly calculation of the bundle adjustment normal equations can be parallelized, which although it performs adequately in the

current version will quickly decrease in performance as the size of the processed data set increases due to the $O(n^2)$ complexity, i.e., the number of required computations increases as the square of the number of individual elements. The solution of the bundle adjustment is processed optimized sparse and symmetric matrix solvers, widely available in open source tools and not expected to be a significant problem.

At the cost of increasing computational complexity, the tie point algorithm should be improved in two ways. First, the accuracy of the algorithm should be improved by employing a more robust sub-pixel least squares matching algorithm on the full resolution imagery, perhaps even including radiometric information from multiple color bands for improved performance. A significant outcome of such a procedure would be a more robust estimate of the quality of the match, leading to another improvement in the algorithm. By employing statistical measures of the match quality, deviation from the epipolar geometry, and locally modeled terrain variations, a robust outlier rejection algorithm such as RANSAC [Fischler, 1981] could be employed to eliminate the need for a human operator.

Although the goal of this directly georeferenced remote sensing technique is the production of two-dimensional mapping applications, vertical relief error due to projection is transferred directly to the output mosaic. The algorithm development in this thesis and its application are greatly enhanced by the nearly constant terrain of South Florida, however, expanding the operational scope of the platform to other terrains necessitates improvements. The ability to produce a strong 3D scene reconstruction will largely be dependent on the densification of the tie points post-adjustment. Given a proper densification procedure and an appropriate DEM generation technique, a transition to true orthophoto production and even the generation of color 3D models should be achievable with moderate effort.

Table 6-1. Corrections to the exterior orientation parameters obtained by the bundle adjustment of the assessed data set

Image	Omega (deg)	Phi (deg)	Kappa (deg)	Easting (m)	Northing (m)	Height (m)
Image82	-1.36	-5.60	0.14	-2.30	2.05	1.57
Image83	-4.43	-4.81	0.83	-0.95	-1.22	1.41
Image84	-1.86	-4.80	0.21	-0.28	3.16	0.79
Image85	0.29	-3.30	0.06	0.50	-4.02	1.01
Image439	-4.52	-6.33	-2.27	-1.21	0.88	2.87
Image440	-3.51	-3.34	-2.29	4.50	0.28	2.82
Image441	-5.40	-3.42	-1.77	3.62	0.95	2.07
Image442	-2.75	-1.08	-2.80	2.02	-0.96	2.93
Image443	-2.05	-5.23	-2.73	-1.91	5.70	3.11
Image530	-4.40	-3.84	2.74	-4.69	1.38	2.57
Image531	-3.40	-2.56	2.89	-0.29	-1.72	2.58
Image532	-4.19	-3.85	2.68	-0.99	3.10	2.16
Image533	-6.28	-1.31	2.82	1.85	0.28	2.01
Image534	-6.47	-1.98	3.32	3.61	0.29	1.71
Image535	-4.95	-4.55	2.73	2.39	1.68	2.86
Image536	-0.71	-5.10	2.56	-4.34	-1.02	2.28
Image537	-3.23	-4.05	2.95	-4.93	-0.72	2.19
Image538	-0.10	-3.44	2.97	2.24	-3.87	1.34
Image624	-2.62	-4.15	2.42	-1.37	-2.56	3.55
Image625	-2.70	-6.10	2.46	-4.26	-2.59	3.91
Image626	-2.86	-3.58	2.37	2.95	-2.24	3.16
Image627	-2.53	-2.64	2.07	1.16	-3.68	2.82
Image628	-3.01	-2.84	1.76	-0.55	2.56	2.46
Image629	-6.64	-1.26	2.09	1.41	1.87	1.73
Image630	-6.50	-1.64	2.55	2.63	4.47	1.63
Image719	-3.82	-1.80	2.00	1.48	3.06	2.76
Image720	-2.79	-4.98	2.22	-1.49	-3.64	4.10
Image721	-2.66	-4.99	2.08	-0.79	-3.45	3.86

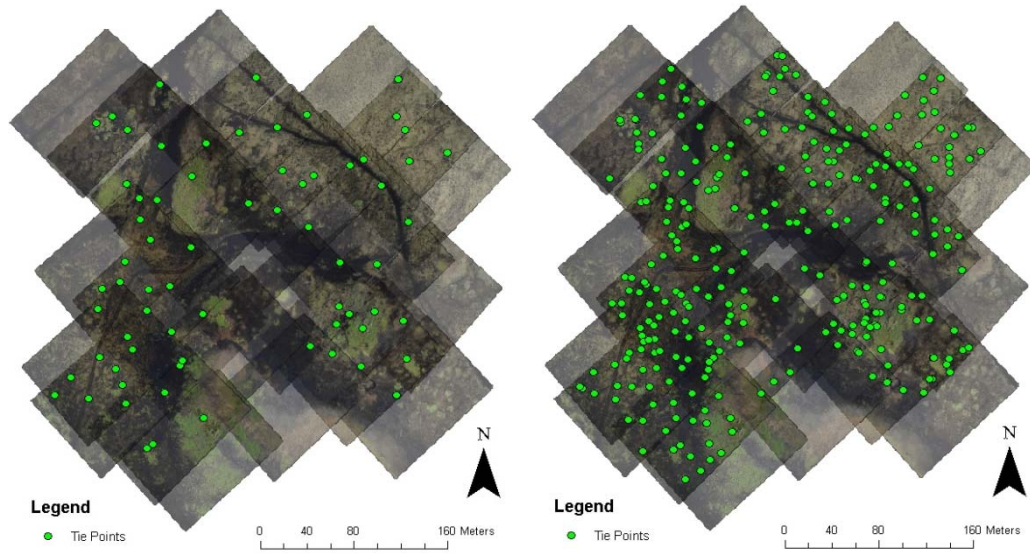


Figure 6-1. The distribution of tie points for the first (left) and second (right) iteration of the assessed data set

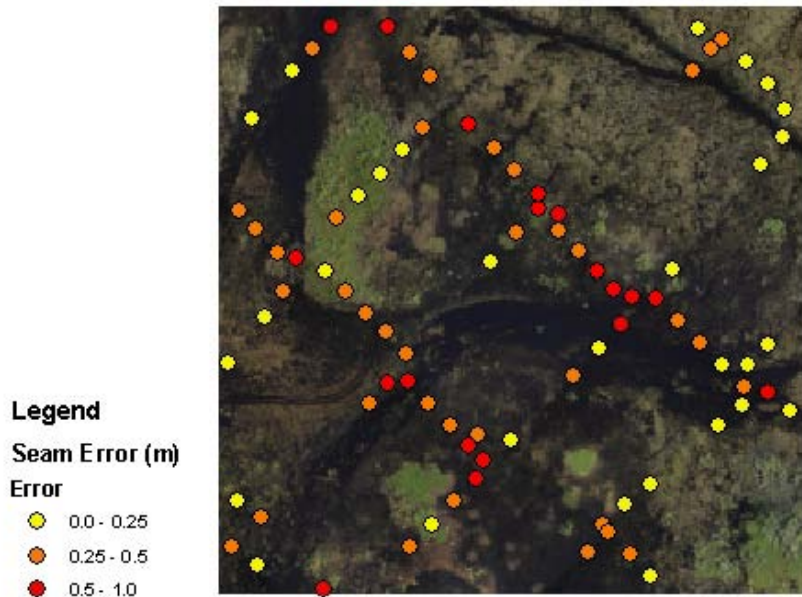


Figure 6-2. Distribution of mosaic seam error measurements and their values

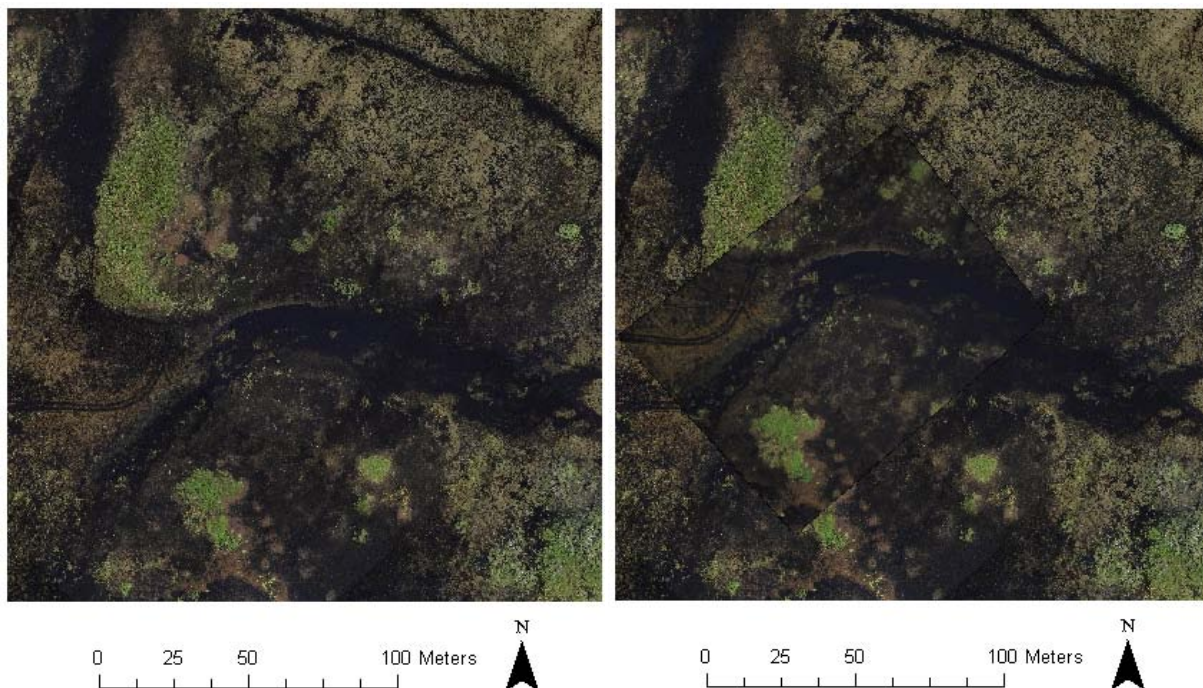


Figure 6-3. Comparison of the mosaic (left) to the unadjusted direct projection of one of the composing images (right) showing the magnitude of the adjustment

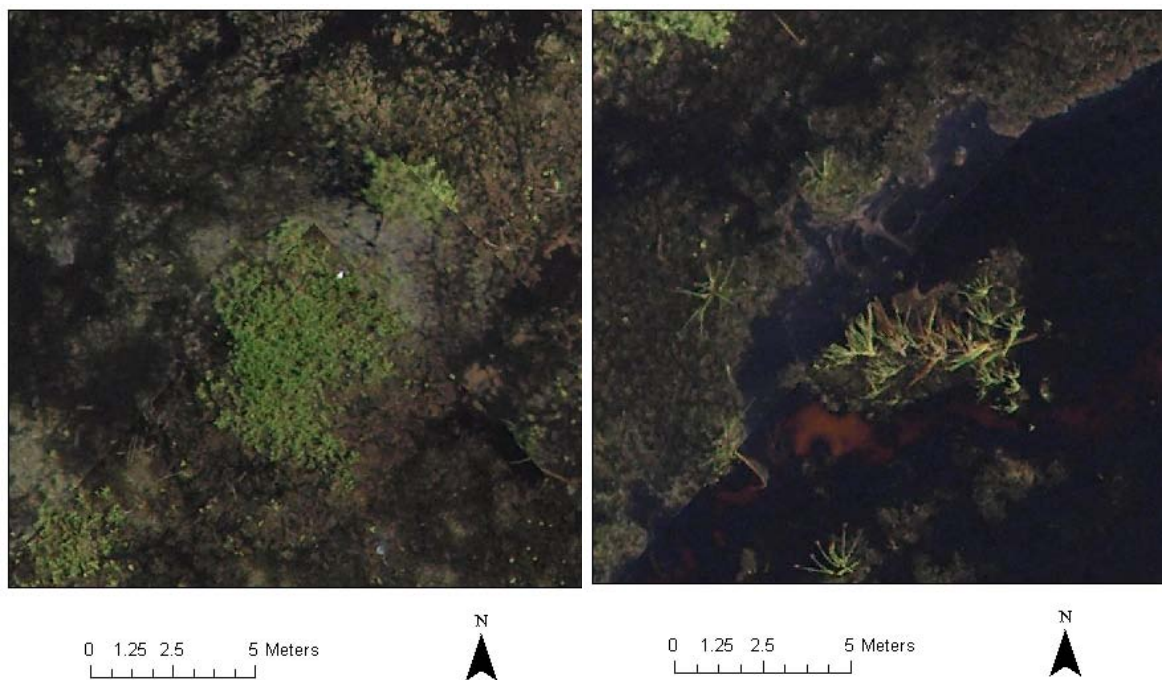


Figure 6-4. Detail of typical mosaicing seam errors at the farther distance from nadir (left) and due to vertical relief in the image (right)



Figure 6-5. Demonstration of detail with observations of a (a) low flying bird, (b) wading birds, a (c) basking alligator, and (d) swimming alligators

APPENDIX A EXAMPLE NOVA II DATA

Each NOVA II flight automatically generates a folder labeled with the time and date. The folder contains two elements, the image files and a log file. The format of the image files is by default .jpg, although the image format is selectable. The log file is generated in real time and combines the information from all payload sensors (except imagery) into a single ASCII file. The log is formatted with each line corresponding to a data or status packet, prefixed by a three-letter code indicating the source of the packet. The packets are described in Table A-1.

The log file is parsed and the packets processed to produce two output files. The most critical file is the geotags file, which provides the direct georeferencing parameters associated with each image. The parameters are calculated by interpolation of the navigation packets using the Burredo synchronization packets associated with the image exposure. A navigation file is also output which simply extracts the trajectory information from the navigation packets

Table A-1. Description of data packets generated by the NOVA II payload

Packet	Description
#nav	Primary data packet from the MTi-G. The columns contain, in order: Accelerometer X, Y, Z (m/s^2) Gyroscope X, Y, Z (deg/s) Magnetometer X, Y, Z (normalized unit vector) Roll, Pitch, Heading (deg) Latitude, Longitude, Height (deg, deg, m) Velocity X, Y, Z (m/s) Status Byte Sample Counter
#bur	Primary data packet from the Burredo. Contains columns: Total clock ticks per epoch Tick count at time of event (0 if no event)
#cam	Camera status packet. The following status messages are available: connect – Camera is detected and driver is successfully loaded disconnect – Camera disconnect detect triggered – Command to take exposure issued captured – Image has been successfully captured and transmitted to host
#img	Occurs after ‘#cam captured’ packet, and indicates the received image’s filename
#bat	Camera battery voltage indicator; decays from 100 to 0 in four decrements

```

.
.
#nav    -0.1696556,   1.200896,      9.28831,     -0.06118384,   -0.1322838, ...
#bur    12709,      0
#nav    -0.4715462,   0.9584169,     8.511579,     0.1064306,     -0.09009447, ...
#bur    12715,      8888
#nav    -0.38655,     0.4612255,     8.632549,     0.117613,      0.046223, ...
#bur    12709,      0
.
.
#nav    2.673782,     2.24282,      11.96289,     -0.174685,     0.4817191, ...
#bur    12710,      0
#nav    -1.024713,     1.151173,     7.965509,     -0.07573284,     0.3828225, ...
#cam captured
#bur    12717,      0
#nav    -0.8589637,   0.05515208,    7.93262,      0.1407275,     0.1154017, ...
#img Image54
#bur    12715,      0
#nav    -0.6533332,   0.7426301,     10.64554,     0.1325313,     0.06682684, ...
#bat 100
#cam triggered
#bur    12714,      0
#nav    -0.7618415,   2.973755,     10.88066,     -0.05635519,     0.03778771, ...
#bur    12715,      0
.
.

```

Figure A-1. Example snippet of the raw NOVA II log file

```

.
.
.
Image54,11.1584336,7.5038065,-46.6413418,27.04287,-80.94872,-16.1395
Image55,13.6815535,7.4690475,7.8909606,27.04287,-80.94868,-15.6799
Image56,11.4603011,3.6719962,20.1081349,27.04289,-80.9486653259,-15.3064
Image57,8.4011598,-1.4245067,35.7729761,27.04291,-80.94865,-15.6219
Image58,12.1938477,-0.4545177,-31.5806834,27.04292,-80.94866,-16.0656
Image59,6.7489705,-7.7903075,-71.8355905,27.04292,-80.94867,-16.2097
.
.
.
```

Figure A-2. Example snippet of the generated NOVA II geotags file

APPENDIX B LIGHTNING LAB CALIBRATION SITE

A regularly spaced grid of ground control points was needed for the calibration and accuracy analysis of the NOVA II payload. A suitable site was selected at the University of Florida Lightning Research Lab in Starke, FL. A model runway used for lightning research was located conveniently adjacent to the selected site, allowing for routine takeoff and landing of the UAV. The GCP grid consisted of raised aerial targets mounted on threaded iron rods driven into the ground and spaced approximately 20 meters apart. The aerial targets were constructed as shown in Figure B-1. The aerial targets consisted of rigid 2' by 2' boards with 18" diameter high-contrast black and white semicircles. In addition to the 32 aerial targets, 5 permanent reference monuments (5' iron rods) were driven into the ground so that the aerial targets could be conveniently resurveyed at a later date.

A precision geodetic survey of the 5 permanent reference monuments was conducted using nearby NGS control with Trimble 5800 GPS equipment. The closest NGS control monuments were KINGLSEY and KINGSLEY RESET. Once the permanent reference points were established, an RTK GPS survey of the 32 aerial targets was completed using Leica System 1200 GPS equipment. Due to post-survey data loss, two of the permanent reference monuments were excluded from the network adjustment due to insufficient GPS observations. The coordinates of PRMs are given in Table B-1. The adjusted WGS 84 UTM Zone 17N coordinate values of the aerial targets are provided in Table B-2. The relative standard deviation of error for the aerial targets was 0.76 cm using a posteriori adjustment statistics and the absolute accuracy was determined to be 2.02 cm.

Table B-1. Lightning Lab Calibration Site permanent reference monument WGS84 coordinates

Control	Latitude (DMS)	Longitude (DMS)	Height (m)
B	29°56'30.74647"	-82°01'52.51608"	44.791
C	29°56'29.64313"	-82°01'55.29755"	43.509
E	29°56'28.61991"	-82°01'52.57836"	43.824

Table B-2. Lightning Lab Calibration Site aerial target WGS84 UTM Zone 17N Coordinates

Point ID	Easting (m)	Northing (m)	Height (m)
1	400333.13	3312789.13	43.61
2	400350.91	3312789.28	43.63
3	400372.44	3312789.14	44.08
4	400392.53	3312788.79	44.09
5	400412.11	3312788.70	43.78
6	400431.80	3312788.62	44.21
7	400452.09	3312788.41	44.48
8	400471.77	3312788.33	44.98
9	400471.19	3312770.83	45.14
10	400452.19	3312770.65	44.83
11	400431.66	3312770.37	44.19
12	400412.17	3312770.26	43.65
13	400392.24	3312770.02	43.43
14	400372.14	3312769.77	43.27
15	400350.86	3312769.57	43.11
16	400332.47	3312769.29	43.23
17	400331.88	3312749.58	42.93
18	400350.77	3312749.71	42.85
19	400371.77	3312750.19	43.29
20	400391.87	3312750.65	43.69
21	400412.12	3312751.06	44.10
22	400431.41	3312751.59	44.73
23	400452.41	3312751.98	45.04
24	400471.36	3312752.31	44.56
25	400471.47	3312729.85	44.03
26	400451.50	3312729.73	44.05
27	400431.17	3312729.63	43.96
28	400412.13	3312729.66	43.97
29	400391.50	3312729.59	43.79
30	400371.40	3312729.46	43.68
31	400350.71	3312729.51	43.22
32	400331.30	3312729.45	43.15

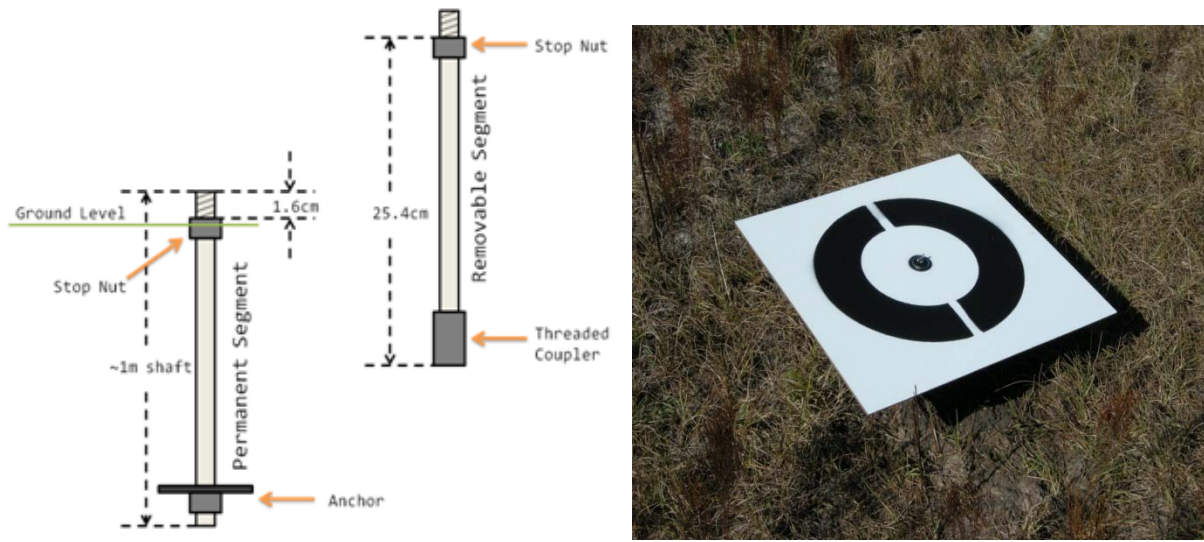


Figure B-1. Physical Design of the Lightning Lab Ground Control Point Aerial Targets

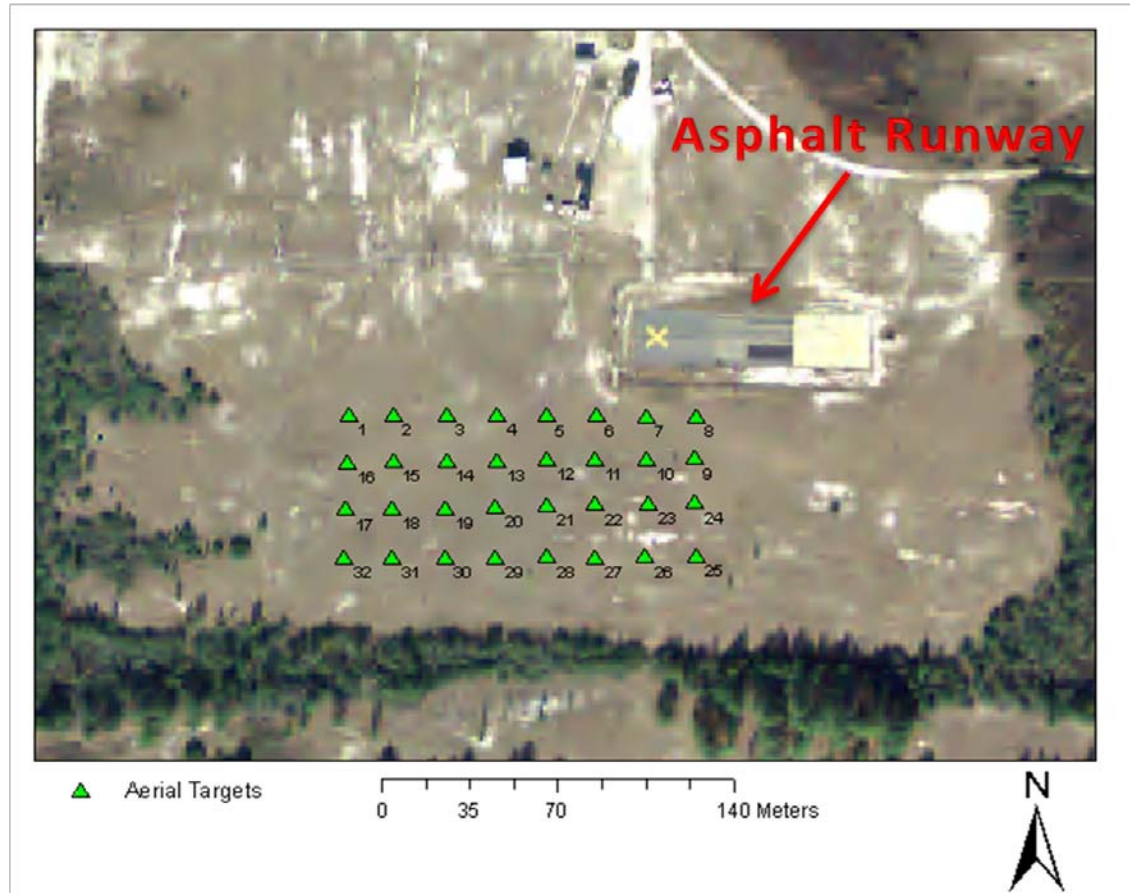


Figure B-2. Aerial view of the Lightning Lab Calibration Site Targets indicating the target distribution

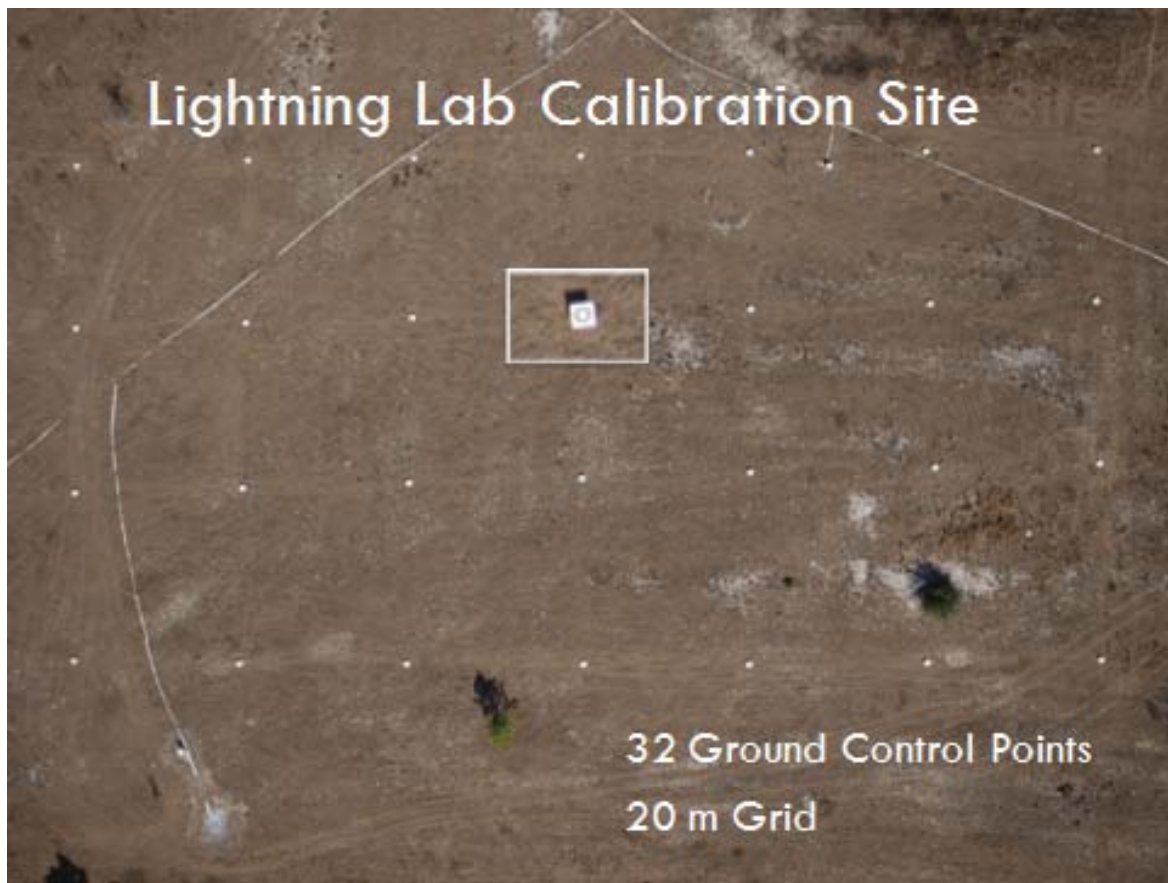


Figure B-3. Aerial view of the Lightning Lab Calibration Site Targets captured by NOVA II with a zoomed inset of an individual target



Figure B-4. NGS Control Monument KINGSLEY (left) and GPS setup (right)

APPENDIX C BUNDLE ADJUSTMENT DEVELOPMENT

The derivation of the bundle adjustment is given here for convenience. The development is then extended to include the interior orientation parameters discussed in Chapter 2. In order to optimally solve the collinearity equations using least squares, they must be linearized. The nonlinearity of the collinearity equations is evident first in their rational form, but the complexity of their linearization is due more to the trigonometric terms in the DCM representation of R_I . Note that the linearization is parameterized with respect to the Euler angle representation of R_I , which allows the orthonormality constraints of a valid rotation matrix to be implicitly enforced. The linearized observation equations, weight matrices, and the direct construction of the normal matrices is developed in Equations C-1 through C-11 with a brief description of each and reflects the development in Wolf and Dewitt [2000]. Rearranging Equation 2-9 gives Equation C-1.

$$F = -f \frac{r}{q} = x_I$$

$$G = -f \frac{s}{q} = y_I$$

$$q = m_{31}\Delta X + m_{32}\Delta Y + m_{33}\Delta Z$$

$$r = m_{11}\Delta X + m_{12}\Delta Y + m_{13}\Delta Z$$

$$s = m_{21}\Delta X + m_{22}\Delta Y + m_{23}\Delta Z$$

$$\Delta X = X_I - X_L,$$

$$\Delta Y = Y_I - Y_L,$$

$$\Delta Z = Z_I - Z_L$$

$$R_I = \begin{bmatrix} m_{11} & m_{12} & m_{13} \\ m_{21} & m_{22} & m_{23} \\ m_{31} & m_{32} & m_{33} \end{bmatrix}$$

(C-1)

First-order Taylor series linearization with respect to image and scene geometry parameters results in Equation C-2.

$$\begin{aligned}
& \left(\frac{\partial F}{\partial \omega_I} \right)_0 d\omega_I + \left(\frac{\partial F}{\partial \phi_I} \right)_0 d\phi_I + \left(\frac{\partial F}{\partial \kappa_I} \right)_0 d\kappa_I + \left(\frac{\partial F}{\partial X_L} \right)_0 dX_L + \left(\frac{\partial F}{\partial Y_L} \right)_0 dY_L + \left(\frac{\partial F}{\partial Z_L} \right)_0 dZ_L \\
& + \left(\frac{\partial F}{\partial X_I} \right)_0 dX_I + \left(\frac{\partial F}{\partial Y_I} \right)_0 dY_I + \left(\frac{\partial F}{\partial Z_I} \right)_0 dZ_I = x_I - F_0 + v_x \\
& \left(\frac{\partial G}{\partial \omega_I} \right)_0 d\omega_I + \left(\frac{\partial G}{\partial \phi_I} \right)_0 d\phi_I + \left(\frac{\partial G}{\partial \kappa_I} \right)_0 d\kappa_I + \left(\frac{\partial G}{\partial X_L} \right)_0 dX_L + \left(\frac{\partial G}{\partial Y_L} \right)_0 dY_L + \left(\frac{\partial G}{\partial Z_L} \right)_0 dZ_L \\
& + \left(\frac{\partial G}{\partial X_I} \right)_0 dX_I + \left(\frac{\partial G}{\partial Y_I} \right)_0 dY_I + \left(\frac{\partial G}{\partial Z_I} \right)_0 dZ_I = y_I - G_0 + v_y
\end{aligned} \tag{C-2}$$

Expanding and simplifying Equation C-2 gives the image observation Equation 5-13.

$$\begin{aligned}
& b_{11}d\omega_I + b_{12}d\phi_I + b_{13}d\kappa_I - b_{14}dX_L - b_{15}dY_L - b_{16}dZ_L + b_{14}dX_I + b_{15}dY_I + b_{16}dZ_I \\
& = J + v_x \\
& b_{21}d\omega_I + b_{22}d\phi_I + b_{23}d\kappa_I - b_{24}dX_L - b_{25}dY_L - b_{26}dZ_L + b_{24}dX_I + b_{25}dY_I + b_{26}dZ_I \\
& = K + v_y
\end{aligned}$$

$$\begin{aligned}
b_{11} &= \frac{f}{q^2} (r(-m_{33}\Delta Y + m_{32}\Delta Z) - q(-m_{13}\Delta Y + m_{12}\Delta Z)) \\
b_{12} &= \frac{f}{q^2} (r(\cos \phi \Delta X + \sin \omega \sin \phi \Delta Y - \cos \omega \sin \phi \Delta Z) \\
&\quad - q(-\sin \phi \cos \kappa \Delta X + \sin \omega \cos \phi \cos \kappa \Delta Y - \cos \omega \cos \phi \cos \kappa \Delta Z)) \\
b_{13} &= -\frac{f}{q} (m_{21}\Delta X + m_{22}\Delta Y + m_{23}\Delta Z) \\
b_{14} &= \frac{f}{q^2} (rm_{31} - qm_{11}) \\
b_{15} &= \frac{f}{q^2} (rm_{32} - qm_{12}) \\
b_{16} &= \frac{f}{q^2} (rm_{33} - qm_{13}) \\
J &= x + f \frac{r}{q} \\
b_{11} &= \frac{f}{q^2} (s(-m_{33}\Delta Y + m_{32}\Delta Z) - q(-m_{23}\Delta Y + m_{22}\Delta Z)) \\
b_{12} &= \frac{f}{q^2} (s(\cos \phi \Delta X + \sin \omega \sin \phi \Delta Y - \cos \omega \sin \phi \Delta Z) \\
&\quad - q(\sin \phi \sin \kappa \Delta X - \sin \omega \cos \phi \sin \kappa \Delta Y + \cos \omega \cos \phi \sin \kappa \Delta Z)) \\
b_{13} &= -\frac{f}{q} (m_{11}\Delta X + m_{12}\Delta Y + m_{13}\Delta Z) \\
b_{14} &= \frac{f}{q^2} (rm_{31} - qm_{21})
\end{aligned}$$

$$\begin{aligned}
b_{15} &= \frac{f}{q^2} (rm_{32} - qm_{22}) \\
b_{16} &= \frac{f}{q^2} (rm_{33} - qm_{23}) \\
K &= x + f \frac{s}{q}
\end{aligned} \tag{C-3}$$

The normal equation is given by Equation C-4.

$$N\Delta = K \tag{C-4}$$

The unknown state vector is given by Equation C-5.

$$\Delta = \begin{bmatrix} \dot{\Delta}_1 \\ \dot{\Delta}_2 \\ \vdots \\ \dot{\Delta}_m \\ \ddot{\Delta}_1 \\ \ddot{\Delta}_2 \\ \vdots \\ \ddot{\Delta}_n \end{bmatrix}, \quad \dot{\Delta}_i = \begin{bmatrix} d\omega_i \\ d\phi_i \\ d\kappa_i \\ dX_i \\ dY_i \\ dZ_i \end{bmatrix}, \quad \ddot{\Delta}_j = \begin{bmatrix} dX_j \\ dY_j \\ dZ_j \end{bmatrix}, \tag{C-5}$$

The matrix form of Equation C-3 is given by Equation C-6.

$$\begin{aligned}
\dot{B}_{ij}\dot{\Delta}_i + \ddot{B}_{ij}\ddot{\Delta}_j &= \varepsilon_{ij} + V_{ij} \\
\dot{B}_{ij} &= \begin{bmatrix} b_{11_{ij}} & b_{12_{ij}} & b_{13_{ij}} & -b_{14_{ij}} & -b_{15_{ij}} & -b_{16_{ij}} \\ b_{21_{ij}} & b_{22_{ij}} & b_{23_{ij}} & -b_{24_{ij}} & -b_{25_{ij}} & -b_{26_{ij}} \end{bmatrix} \\
\ddot{B}_{ij} &= \begin{bmatrix} b_{14_{ij}} & b_{15_{ij}} & b_{16_{ij}} \\ b_{24_{ij}} & b_{25_{ij}} & b_{26_{ij}} \end{bmatrix} \\
\varepsilon_{ij} &= \begin{bmatrix} J_{ij} \\ K_{ij} \end{bmatrix}, \quad V_{ij} = \begin{bmatrix} v_{x_{ij}} \\ v_{y_{ij}} \end{bmatrix}
\end{aligned} \tag{C-6}$$

Noting that the superscript ⁰ indicates a calculated value and the superscript ⁰⁰ indicates a measurement, the direct georeferencing observations of the exterior orientation parameters are given in a linearized form by Equation C-7.

$$\begin{aligned}
\omega_i^0 + d\omega_i &= \omega_i^{00} + v_{\omega_i} \\
\phi_i^0 + d\phi_i &= \phi_i^{00} + v_{\phi_i} \\
\kappa_i^0 + d\kappa_i &= \kappa_i^{00} + v_{\kappa_i}
\end{aligned}$$

$$\begin{aligned}
X_i^0 + dX_i &= X_i^{00} + v_{X_i} \\
Y_i^0 + dY_i &= Y_i^{00} + v_{Y_i} \\
Z_i^0 + dZ_i &= Z_i^{00} + v_{Z_i} \\
\dot{\Delta}_i &= \dot{C}_i + \dot{V}_i \\
\dot{C}_i &= [\omega_i^0 \quad \phi_i^0 \quad \kappa_i^0 \quad X_i^0 \quad Y_i^0 \quad Z_i^0] \\
\dot{V}_i &= [v_{\omega_i} \quad v_{\phi_i} \quad v_{\kappa_i} \quad v_{X_i} \quad v_{Y_i} \quad v_{Z_i}]
\end{aligned} \tag{C-7}$$

Similarly, observations for ground control points, if used, are given by Equation C-8,

$$\begin{aligned}
X_j^0 + dX_j &= X_j^{00} + v_{X_j} \\
Y_j^0 + dY_j &= Y_j^{00} + v_{Y_j} \\
Z_j^0 + dZ_j &= Z_j^{00} + v_{Z_j} \\
\ddot{\Delta}_j &= \ddot{C}_j + \ddot{V}_j \\
\ddot{C}_j &= \begin{bmatrix} X_j^{00} - X_j^0 \\ Y_j^{00} - Y_j^0 \\ Z_j^{00} - Z_j^0 \end{bmatrix} \\
\ddot{V}_j &= \begin{bmatrix} v_{X_j} \\ v_{Y_j} \\ v_{Z_j} \end{bmatrix}
\end{aligned} \tag{C-8}$$

For all observations, appropriate weight matrices must be used. Note that all weight matrices are scaled by the reference variance, usually chosen as 1.0, and are given by Equation C-9.

$$W_{ij} = \sigma_0^2 \begin{bmatrix} \sigma_{x_{ij}}^2 & \sigma_{x_{ij}y_{ij}} \\ \sigma_{y_{ij}x_{ij}} & \sigma_{y_{ij}}^2 \end{bmatrix}^{-1}$$

$$\dot{W}_i = \sigma_0^2 \begin{bmatrix} \sigma_{\omega_i}^2 & \sigma_{\omega_i\phi_i} & \sigma_{\omega_i\kappa_i} & \sigma_{\omega_iX_i} & \sigma_{\omega_iY_i} & \sigma_{\omega_iZ_i} \\ \sigma_{\phi_i\omega_i} & \sigma_{\phi_i}^2 & \sigma_{\phi_i\kappa_i} & \sigma_{\phi_iX_i} & \sigma_{\phi_iY_i} & \sigma_{\phi_iZ_i} \\ \sigma_{\kappa_i\omega_i} & \sigma_{\kappa_i\phi_i} & \sigma_{\kappa_i}^2 & \sigma_{\kappa_iX_i} & \sigma_{\kappa_iY_i} & \sigma_{\kappa_iZ_i} \\ \sigma_{X_i\omega_i} & \sigma_{X_i\phi_i} & \sigma_{X_i\kappa_i} & \sigma_{X_i}^2 & \sigma_{X_iY_i} & \sigma_{X_iZ_i} \\ \sigma_{Y_i\omega_i} & \sigma_{Y_i\phi_i} & \sigma_{Y_i\kappa_i} & \sigma_{Y_iX_i} & \sigma_{Y_i}^2 & \sigma_{Y_iZ_i} \\ \sigma_{Z_i\omega_i} & \sigma_{Z_i\phi_i} & \sigma_{Z_i\kappa_i} & \sigma_{Z_iX_i} & \sigma_{Z_iY_i} & \sigma_{Z_i}^2 \end{bmatrix}^{-1}$$

$$\ddot{W}_j = \sigma_0^2 \begin{bmatrix} \sigma_{X_j}^2 & \sigma_{X_j Y_j} & \sigma_{X_j Z_j} \\ \sigma_{Y_j X_j} & \sigma_{Y_j}^2 & \sigma_{Y_j Z_j} \\ \sigma_{Z_j X_j} & \sigma_{Z_j Y_j} & \sigma_{Z_j}^2 \end{bmatrix}^{-1} \quad (\text{C-9})$$

Using Equations C-6 through C-9, the normal equations can be composed directly by Equation C-10 and C-11.

$$N = \begin{bmatrix} \dot{N}_1 + \dot{W}_1 & 0 & \cdots & 0 & \bar{N}_{11} & \bar{N}_{12} & \cdots & \bar{N}_{1n} \\ 0 & \dot{N}_2 + \dot{W}_2 & \cdots & 0 & \bar{N}_{21} & \bar{N}_{22} & \cdots & \bar{N}_{2n} \\ \vdots & \vdots & \ddots & 0 & \vdots & \vdots & \vdots & \vdots \\ 0 & 0 & 0 & \dot{N}_m + \dot{W}_m & \bar{N}_{m1} & \bar{N}_{m2} & \cdots & \bar{N}_{mn} \\ \bar{N}_{11}^T & \bar{N}_{21}^T & \cdots & \bar{N}_{m1}^T & \ddot{N}_1 + \ddot{W}_1 & 0 & \cdots & 0 \\ \bar{N}_{12}^T & \bar{N}_{22}^T & \cdots & \bar{N}_{m2}^T & 0 & \ddot{N}_2 + \ddot{W}_2 & \cdots & 0 \\ \vdots & \vdots & \cdots & \vdots & \vdots & \vdots & \ddots & 0 \\ \bar{N}_{1n}^T & \bar{N}_{2n}^T & \cdots & \bar{N}_{mn}^T & 0 & 0 & 0 & \ddot{N}_n + \ddot{W}_n \end{bmatrix}$$

$$\dot{N}_i = \sum_{j=1}^n \dot{B}_{ij}^T W_{ij} \dot{B}_{ij}$$

$$\ddot{N}_j = \sum_{i=1}^m \ddot{B}_{ij}^T W_{ij} \ddot{B}_{ij},$$

$$\bar{N}_{ij} = \dot{B}_{ij}^T W_{ij} \ddot{B}_{ij} \quad (\text{C-10})$$

$$K = \begin{bmatrix} \dot{K}_1 + \dot{W}_1 \dot{C}_1 \\ \dot{K}_2 + \dot{W}_2 \dot{C}_2 \\ \vdots \\ \dot{K}_m + \dot{W}_m \dot{C}_m \\ \ddot{K}_1 + \ddot{W}_1 \ddot{C}_1 \\ \ddot{K}_2 + \ddot{W}_2 \ddot{C}_2 \\ \vdots \\ \ddot{K}_n + \ddot{W}_n \ddot{C}_n \end{bmatrix}$$

$$\begin{aligned}\dot{K}_i &= \sum_{j=1}^n \dot{B}_{ij}^T W_{ij} \varepsilon_{ij} \\ \ddot{K}_j &= \sum_{i=1}^m \ddot{B}_{ij}^T W_{ij} \varepsilon_{ij}\end{aligned}\tag{C-11}$$

Recalling that the interior orientation parameters can be specified in the collinearity equations, it is obvious that they can be included in the simultaneous bundle adjustment solution. The assumption will be made for this development that all data is collected using the same camera at approximately the same time, with the conclusion being that the interior orientation parameters are constant over all images for a particular bundle adjustment. Thus, we proceed by linearizing the additional interior orientation parameters from Equation 2-14.

$$\begin{aligned}F &= x_o + \Delta x - f \frac{r}{q} = x_l \\ G &= y_o + \Delta y - f \frac{s}{q} = y_l\end{aligned}\tag{C-12}$$

$$\begin{aligned}\left(\frac{\partial F}{\partial f}\right)_0 df + \left(\frac{\partial F}{\partial x_o}\right)_0 dx_o + \left(\frac{\partial F}{\partial k_{r_1}}\right)_0 dk_{r_1} + \left(\frac{\partial F}{\partial k_{r_2}}\right)_0 dk_{r_2} + \left(\frac{\partial F}{\partial k_{r_3}}\right)_0 dk_{r_3} \\ + \left(\frac{\partial F}{\partial k_{t_1}}\right)_0 dk_{t_1} + \left(\frac{\partial F}{\partial k_{t_2}}\right)_0 dk_{t_2} + \left(\frac{\partial F}{\partial k_{a_1}}\right)_0 dk_{a_1} + \left(\frac{\partial F}{\partial k_{a_2}}\right)_0 dk_{a_2} \\ + \left(\frac{\partial F}{\partial \omega}\right)_0 d\omega + \left(\frac{\partial F}{\partial \phi}\right)_0 d\phi + \left(\frac{\partial F}{\partial \kappa}\right)_0 d\kappa + \left(\frac{\partial F}{\partial X_L}\right)_0 dX_L + \left(\frac{\partial F}{\partial Y_L}\right)_0 dY_L \\ + \left(\frac{\partial F}{\partial Z_L}\right)_0 dZ_L + \left(\frac{\partial F}{\partial X_A}\right)_0 dX_A + \left(\frac{\partial F}{\partial Y_A}\right)_0 dY_A + \left(\frac{\partial F}{\partial Z_A}\right)_0 dZ_A = x - F_0 + v_x \\ \left(\frac{\partial G}{\partial f}\right)_0 df + \left(\frac{\partial G}{\partial y_o}\right)_0 dy_o + \left(\frac{\partial G}{\partial k_{r_1}}\right)_0 dk_{r_1} + \left(\frac{\partial G}{\partial k_{r_2}}\right)_0 dk_{r_2} + \left(\frac{\partial G}{\partial k_{r_3}}\right)_0 dk_{r_3} \\ + \left(\frac{\partial G}{\partial k_{t_1}}\right)_0 dk_{t_1} + \left(\frac{\partial G}{\partial k_{t_2}}\right)_0 dk_{t_2} + \left(\frac{\partial G}{\partial \omega}\right)_0 d\omega + \left(\frac{\partial G}{\partial \phi}\right)_0 d\phi + \left(\frac{\partial G}{\partial \kappa}\right)_0 d\kappa \\ + \left(\frac{\partial G}{\partial X_L}\right)_0 dX_L + \left(\frac{\partial G}{\partial Y_L}\right)_0 dY_L + \left(\frac{\partial G}{\partial Z_L}\right)_0 dZ_L + \left(\frac{\partial G}{\partial X_A}\right)_0 dX_A + \left(\frac{\partial G}{\partial Y_A}\right)_0 dY_A \\ + \left(\frac{\partial G}{\partial Z_A}\right)_0 dZ_A = y - G_0 + v_y\end{aligned}\tag{C-13}$$

Equation C-3 is simplified in Equation C-4, with b_{xx} terms identical to their definition in Equation C-3, and the matrix formulation given in Equation C-5.

$$\begin{aligned}
& \gamma_{11}df + \gamma_{12}dx_o + \gamma_{14}dk_{r_1} + \gamma_{15}dk_{r_2} + \gamma_{16}dk_{r_3} + \gamma_{17}dk_{t_1} + \gamma_{18}dk_{t_2} + \gamma_{19}dk_{a_1} \\
& \quad + \gamma_{1,10}dk_{a_2} + b_{11}d\omega + b_{12}d\phi + b_{13}d\kappa - b_{14}dX_L - b_{15}dY_L - b_{16}dZ_L \\
& \quad + b_{14}dX_A + b_{15}dY_A + b_{16}dZ_A = J + v_x \\
& \gamma_{21}df + \gamma_{23}dx_o + \gamma_{24}dk_{r_1} + \gamma_{25}dk_{r_2} + \gamma_{26}dk_{r_3} + \gamma_{27}dk_{t_1} + \gamma_{28}dk_{t_2} + b_{21}d\omega \\
& \quad + b_{22}d\phi + b_{23}d\kappa - b_{24}dX_L - b_{25}dY_L - b_{26}dZ_L + b_{24}dX_A + b_{25}dY_A \\
& \quad + b_{26}dZ_A = J + v_x
\end{aligned} \tag{C-14}$$

$$\dot{\Delta}_{ij} + \ddot{\Delta}_{ij} + \Gamma_{ij}\ddot{\Delta} = \varepsilon_{ij} + V_{ij}$$

$$\Gamma = \begin{bmatrix} \gamma_{11} & 1 & 0 & \gamma_{14} & \gamma_{15} & \gamma_{16} & \gamma_{17} & \gamma_{18} & \gamma_{19} & \gamma_{1,10} \\ \gamma_{21} & 0 & 1 & \gamma_{24} & \gamma_{25} & \gamma_{26} & \gamma_{27} & \gamma_{28} & 0 & 0 \end{bmatrix}$$

$$\ddot{\Delta} = [f \quad x_o \quad y_o \quad k_{r_1} \quad k_{r_2} \quad k_{r_3} \quad k_{t_1} \quad k_{t_2} \quad k_{a_1} \quad k_{a_2}]^T$$

$$\begin{aligned}
\gamma_{11} &= -r/q \\
\gamma_{14} &= xd^2 \\
\gamma_{15} &= xd^4 \\
\gamma_{16} &= xd^6 \\
\gamma_{17} &= d^2 + 2x^2 \\
\gamma_{18} &= 2xy \\
\gamma_{19} &= x \\
\gamma_{1,10} &= y \\
\gamma_{21} &= -s/q \\
\gamma_{24} &= yd^2 \\
\gamma_{25} &= yd^4 \\
\gamma_{26} &= yd^6 \\
\gamma_{27} &= 2xy \\
\gamma_{28} &= d^2 + 2y^2
\end{aligned} \tag{C-15}$$

In the case that one or more internal orientation parameters are known a priori, we must take into account direct observations of the internal orientation parameters which is developed directly in matrix form by Equation C-16.

$$\ddot{\Delta} = \ddot{C} + \ddot{V}$$

$$\ddot{C} = \begin{bmatrix} f^{00} - f^0 \\ x_o^{00} - x_o^0 \\ y_o^{00} - y_o^0 \\ k_{r_1}^{00} - k_{r_1}^0 \\ k_{r_2}^{00} - k_{r_2}^0 \\ k_{r_3}^{00} - k_{r_3}^0 \\ k_{t_1}^{00} - k_{t_1}^0 \\ k_{t_2}^{00} - k_{t_2}^0 \\ k_{a_1}^{00} - k_{a_1}^0 \\ k_{a_2}^{00} - k_{a_2}^0 \end{bmatrix}, \quad \ddot{V} = \begin{bmatrix} v_f \\ v_{x_o} \\ v_{y_o} \\ v_{k_{r_1}} \\ v_{k_{r_2}} \\ v_{k_{r_3}} \\ v_{k_{t_1}} \\ v_{k_{t_2}} \\ v_{k_{a_1}} \\ v_{k_{a_2}} \end{bmatrix}, \quad w_{\ddot{\Delta}} = \begin{bmatrix} \sigma_f \\ \sigma_{x_o} \\ \sigma_{y_o} \\ \sigma_{k_{r_1}} \\ \sigma_{k_{r_2}} \\ \sigma_{k_{r_3}} \\ \sigma_{k_{t_1}} \\ \sigma_{k_{t_2}} \\ \sigma_{k_{a_1}} \\ \sigma_{k_{a_2}} \end{bmatrix}, \quad \ddot{W} = [\sigma_0^2 w_{\ddot{\Delta}} w_{\ddot{\Delta}}^T]^{-1}$$

(C-16)

The terms of the self-calibrating bundle adjustment normal equation can be composed directly by Equations C-17 and C-18.

$$N = \left[\begin{array}{ccccccccc} \ddot{N} + \ddot{W} & \widehat{N}_1 & \widehat{N}_2 & \cdots & \widehat{N}_m & \widehat{N}_1 & \widehat{N}_2 & \cdots & \widehat{N}_n \\ \widehat{N}_1^T & \dot{N}_1 + \dot{W}_1 & 0 & \cdots & 0 & \bar{N}_{11} & \bar{N}_{12} & \cdots & \bar{N}_{1n} \\ \widehat{N}_2^T & 0 & \dot{N}_2 + \dot{W}_2 & \cdots & 0 & \bar{N}_{21} & \bar{N}_{22} & \cdots & \bar{N}_{2n} \\ \vdots & \vdots & \vdots & \ddots & 0 & \vdots & \vdots & \vdots & \vdots \\ \widehat{N}_m^T & 0 & 0 & 0 & \dot{N}_m + \dot{W}_m & \bar{N}_{m1} & \bar{N}_{m2} & \cdots & \bar{N}_{mn} \\ \widehat{N}_1^T & \bar{N}_{11}^T & \bar{N}_{21}^T & \cdots & \bar{N}_{m1}^T & \ddot{N}_1 + \ddot{W}_1 & 0 & \cdots & 0 \\ \widehat{N}_2^T & \bar{N}_{12}^T & \bar{N}_{22}^T & \cdots & \bar{N}_{m2}^T & 0 & \ddot{N}_2 + \ddot{W}_2 & \cdots & 0 \\ \vdots & \vdots & \vdots & \cdots & \vdots & \vdots & \vdots & \ddots & 0 \\ \widehat{N}_n^T & \bar{N}_{1n}^T & \bar{N}_{2n}^T & \cdots & \bar{N}_{mn}^T & 0 & 0 & 0 & \ddot{N}_n + \ddot{W}_n \end{array} \right]$$

$$\begin{aligned}
\ddot{N} &= \sum_{i=1}^m \sum_{j=1}^n \Gamma_{ij}^T W_{ij} \Gamma_{ij} \\
\widehat{N}_i &= \sum_j^n \Gamma_{ij}^T W_{ij} \dot{\mathbf{B}}_{ij} \\
\widehat{N}_j &= \sum_i^m \Gamma_{ij}^T W_{ij} \ddot{\mathbf{B}}_{ij}
\end{aligned} \tag{C-17}$$

$$\mathbf{K} = \begin{bmatrix} \ddot{K} + \ddot{W} \ddot{C} \\ \dot{K}_1 + \dot{W}_1 \dot{C}_1 \\ \dot{K}_2 + \dot{W}_2 \dot{C}_2 \\ \vdots \\ \dot{K}_m + \dot{W}_m \dot{C}_m \\ \ddot{K}_1 + \ddot{W}_1 \ddot{C}_1 \\ \ddot{K}_2 + \ddot{W}_2 \ddot{C}_2 \\ \vdots \\ \ddot{K}_n + \ddot{W}_n \ddot{C}_n \end{bmatrix}$$

$$\ddot{K} = \sum_{i=1}^m \sum_{j=1}^n \Gamma_{ij}^T W_{ij} \varepsilon_{ij} \tag{C-18}$$

LIST OF REFERENCES

- Acutime, 2007. Trimble® AcuTime® Gold GPS smart antennae user guide, *Trimble Incorporated*, 128 p.
- Bendat, J. and A. Piersol, 2000. Random Data Analysis and Measurement Procedures. *Wiley-Interscience*, New York, NY, 594 p.
- Bowman, S., 2008 Design and validation of an autonomous rapid mapping system using a small UAV, *Master's Thesis*, University of Florida, Gainesville, FL, 115 p.
- Bowman, W. S., A. C. Watts, J. H. Perry, M. Morton, P. G. Ifju, 2008. UAS as monitoring tools for assessing the Nation's levees and monitoring invasive plant populations. Presentation Slides. *Workshop held at the US Army Corps of Engineers Research and Development Center*, March 19, Vicksburg, MS.
- Brown, D.C., 1971. Close-range camera calibration, *Photogrammetric Engineering*, 37(8):855-866.
- Burgess, M.A., P.G. Ifju, H.F. Percival, J.H. Perry, and S.E. Smith, 2009. Development of a survey-grade sUAS for natural resource assessment and monitoring, *Florida Cooperative Fish and Wildlife Research Unit Annual Coordinating Committee Meeting*, Slide presentation, May 23, Gainesville, FL.
- Capodiferro, L., R. Cusani, G. Jacovitti, and M. Vascotto, 1987. A Correlation Based Technique for Shift, Scale, and Rotation Independent Object Identification, Acoustics, Speech, and Signal Processing, *IEEE International Conference on ICASSP '87*, 12:221-224
- Chao, H., M. Baumann, A. Jensen, Y.Q. Chen, Y. Cao, W. Ren, and M. McKee, 2008. Band-reconfigurable Multi-UAV-based Cooperative Remote Sensing for Real-time Water Management and Distributed Irrigation Control, *Proceedings of the 17th Word Congress of the International Federation of Automatic Control*, July 6-11, Seoul, Korea, 6 p.
- Chatfield, A., 1997. Fundamentals of High Accuracy Inertial Navigation, *American Institute of Aeronautics and Astronautics*, Reston, WA, 339 p.
- Cox, T., C. Nagy, A. Mark, M. Skoog, and I. Somers, 2004. Civil UAV Capability Assessment. *NASA Draft Report*. 103 p.
- Cramer, M., 1999. Direct geocoding - is aerial triangulation obsolete?, *Photogrammetric Week '99*, Heidelberg, Germany pp. 59–70.
- Cramer, M. and D. Stallmann, 2002. System calibration for direct georeferencing. International Archives of Photogrammetry, *Remote Sensing and the Spatial Information Sciences*, 34(3A): 79–84.

- Cramer, M., D. Stallman, and N. Haala, 2000. Direct georeferencing using GPS/inertial exterior orientations for photogrammetric applications, *Proceedings of ISPRS XIX Congress*, Amsterdam, Netherlands, pp. 198–205.
- Cressie, N., 1985. Fitting Variogram Models by Weighted Least Squares, *Mathematical Geology*, 17(5): 563-586
- Cressie, N., 1993. Statistics for Spatial Data, Wiley-Interscience, Hoboken, N.J., 928 p.
- Ebner, H., 1976. Self-calibrating block adjustment, *Congress of the International Society for Photogrammetry, Invited Paper of Commission III*, Helsinki, Finland, 11 p.
- Eisenbeiss, H. and L. Zhang, 2006. Comparison of DSMs Generated From Mini UAV Imagery and Terrestrial Laser Scanner in a Cultural Heritage Application, *ISPRS Commission V: Image Engineering and Vision Metrology Symposium*, Sept. 25-27, Dresden, Germany, 36(5):90-96.
- Eisenbeiss, H., 2004. A Mini Unmanned Aerial Vehicle (UAV): System Overview and Image Acquisition, *International Workshop on Processing and Visualization Using High-Resolution Imagery*, Nov. 18-20, Pitsanulok, Thailand, 7 p.
- Evenden, G., PROJ.4 - Cartographic Projections Library, *RemoteSensing.Org*, retrieved June 2009: <http://www.remotesensing.org/proj/>
- Finlayson, G. D., B. Schiele, and J. Crowley, 1998. Comprehensive Colour Image Normalization. *Computer Vision – ECCV'98*, Springer-Berlin, pp. 475-490.
- Fischler, M. A. and R.C. Bolles, 1981. Random sample consensus: A paradigm for model fitting with applications to image analysis and automated cartography. *Communication of the Association of Computing Machinery*, 24(6):381–395.
- Fraser, C., 1997. Digital Camera Self-Calibration, *Journal of Photogrammetric Engineering and Remote Sensing*, 52(3):149-159.
- Geus, R. and P. Arbenz, 2003. PySparse and PyFemax: A Python framework for large scale sparse linear algebra. *PyCon '03*, March 13, Washington, DC, 10 p.
- Greening, W. J., W. Schickler, and A. Thorpe, 2000. The Proper Use Of Directly Observed Orientation Data: Aerial Triangulation Is Not Obsolete, *ASPRS Annual Conference*, May 22-26, Washington, DC, 8 p.
- Grenzdörffer, G.J., A. Engel, and B. Teichert, 2008. The Photogrammetric Potential of Low-Cost UAVs in Forestry and Agriculture, *The International Archives of the Photogrammetry, Remote Sensing and Spatial Information Sciences*, 31(B3):1207-1214.
- Grenzdörffer, G.J., 2004, Digital Low-Cost Remote Sensing with PFIFF, the Integrated Digital Remote Sensing System, *ISPRS Annual Conference*, July 12-23, Istanbul, Turkey, pp. 235-239.

- Greening, T., W. Schickler, A. Thorpe, 2000. The proper use of directly observed orientation data: Aerial triangulation is not obsolete. *ASPRS Annual Conference*, May 20-24, Washington, DC, 12 p.
- Golub, G. and C. Van Loan, 1996. Matrix Computations, 3rd Edition, *John Hopkins University Press*, Baltimore, MD, 694 p.
- Gruen, A.W., 1985. Adaptive Least Squares Correlation: A Powerful Image Matching Technique, *South African Journal of Photogrammetry, Remote Sensing and Cartography*, 14(3): 175-187.
- Habib, A, A. Pullivelli, E. Mitishita, M. Ghanma, and E. Kim, 2005. Stability analysis of low-cost digital cameras for aerial mapping using different georeferencing techniques, *The Photogrammetric Record*, 21(113):29-43.
- Harris, C. and M. Stephens, 1988. A combined corner and edge detector, *Proceedings of the Fourth Alvey Vision Conference*, Manchester, U.K., pp. 147–151.
- Hartley, R. and J. Mundy, 1994. The relationship between photogrammetry and computer vision, *SPIE Proceedings*, 1944:92-105.
- Heipke, C., K.Jacobsen, and H. Wegmann, (Eds.), 2002. Integrated Sensor Orientation: test report and workshop proceedings. *OEEPE Official Publication 43*. 297 pages.
- Honkavaara, E., R. Ilves, and J. Jaakkola, 2003. Practical results of GPS/IMU/camera system calibration. *ISPRS International Workgroup: Group I/5 Theory, Technology and Realities of Inertial/GPS Sensor Orientation*, Sept. 22-23, Castelldefels, Spain, 10 p.
- Horn, B.K., 1999. Projective geometry considered harmful, Manuscript, retrieved June 2009, <http://www.ai.mit.edu/people/bkph/>
- Hruska, R., G. Lancaster, J. Harbour, and S. Cherry, 2005. Small UAV-acquired, High-Resolution, Georeferenced Still Imagery, *Wildlife Society 12th Annual Conference*, Sept. 25-29, Madison, WI, 13 p.
- Ilstrup, D., M. Lizarraga, G. Elkaim, and J. Davis, 2008. Aerial Photography using a Nokia N95, *World Congress on Engineering and Computer Science*, Oct. 22-24, San Francisco, CA., 7 p.
- Jensen, A., M. Baumann, and Y. Chen, 2008. Low-Cost Multispectral Aerial Imaging Using Autonomous Runway-Free Small Flying Wing Vehicles, *IEEE International Geoscience and Remote Sensing Symposium*, July 7-11, Boston, MA, 4 p.
- Jones, G.P., L.G. Pearlstine, H.F. Percival, 2006. An Assessment of Small Unmanned Aerial Vehicles for Wildlife Research, *Wildlife Society Bulletin*, 34(3): 750-758
- Jones, P., 2003. The Feasibility of Using Small Unmanned Aerial Vehicles for Wildlife Research, *Master's Thesis*, University of Florida.

- Jung, I., and S. Lacroix, 2003. High Resolution Terrain Mapping Using Low Altitude Aerial Stereo Imagery, *Proceedings of the Ninth IEEE International Conference on Computer Vision*, Oct. 14-17, Nice, France, 6 p.
- Khoshelham, K., 2009. Role of Tie Points in Integrated Sensor Orientation for Photogrammetric Map Compilation, *Photogrammetric Engineering and Remote Sensing*, 75(3):305-311.
- Kraus, K. 2007, Photogrammetry, 2nd Ed., *de Gruyter*, New York, 459 p.
- KML, 2009. KML Documentation Website, Google, Inc., retrieved June 2009, <http://code.google.com/apis/kml/documentation/>
- Kuipers, J., 1999. Quaternions and Rotation Sequences. *Princeton University Press*, Princeton, NJ, 371 p.
- Ladd, G., A. Nagchaudhuro, T. Earl, and M. Mitra, 2006. Rectification, Georeferencing, and Mosaicing of Images Acquired with Remotely Operated Aerial Platforms, *ASPRS Annual Conference*, May 1-5, Reno, Nevada, 10 p.
- Lena. "Lena", 512x512 pixels, USC-SIPI Image Database. <http://sipi.usc.edu/database/>
- Legat, K., 2006. Approximate direct georeferencing in national coordinates, *Journal of Photogrammetry and Remote Sensing*, 60(4):239-255.
- Li, B., C. Rizos, H.K. Lee, and H.K. Lee, 2006. A GPS-slaved Time Synchronization System for Hybrid Navigation, *GPS Solutions*, 10:207-217.
- Majumdar, J., S. Vinay, and S. Selvi, 2004. Registration And Mosaicing For Images Obtained From UAV, *IEEE International Conference on Signal Processing and Communications*, Dec. 11-14, Bangalore, India, pp. 198-203.
- Misra, P., B. Burke, and M. Pratt, 1999. GPS Performance in Navigation. Proceedings of the IEEE, 87(1):65-85.
- Mohamed, A., R. Price, 2002. Near the Speed of Flight, Aerial mapping with GPS/INS Direct Geo-referencing, *GPS World*, 13(3):40:46.
- Mostafa, M.M.R., and K.P. Schwarz, 2000. A Multi-Sensor System for Airborne Image Capture and Georeferencing. *Photogrammetric Engineering & Remote Sensing*, 66(12):1417-1423.
- Nagai, M., T. Chen, R. Shibasaki, H. Kumagai, and A. Ahmed, 2009. UAV-Borne 3-D Mapping System by Multisensor Integration, *IEEE Transactions On Geoscience And Remote Sensing*, 47(3):701-708.
- Olympus E-420, 2008. Olympus E-420 Instruction Manual, Olympus USA, Inc. retrieved June 2009, http://www.olympusamerica.com/files/E-420_Instruction_Manual_EN.pdf

OpenCV, 2001. Open Source Computer Vision Library: Reference Manual, Intel Corporation, 443 p.

Palubinskas, G., R. Muller, and P. Reinartz, 2003. Radiometric Normalization of Optical Remote Sensing Imagery, *International Geoscience And Remote Sensing Symposium*, July 21-25, Toulouse, France, 2:720–722.

Parker, J.A., R.V. Kenyon, and D.E. Troxel, 1983. Comparison of Interpolating Methods for Image Resampling, *IEEE Transactions on Medical Imaging*, 2(1):31-39.

Perry, J., A. Mohamed, A. Abd-Elrahman, W.S. Bowman, Y. Kaddoura, and A. Watts, 2008. Precision Directly Georeferenced Unmanned Aerial Remote Sensing System: Performance Evaluation. *Proceedings of the ION National Technical Meeting*, Jan. 24-26, San Diego, CA, 7 p.

Reddy, B.S. and B.N. Chatterji, 1996. An FFT-Based Technique for Translation, Rotation, and Scale-Invariant Image Registration, *IEEE Transaction on Image Processing*, 5(8):1266-1271.

Ressl, C., 2002. The impact of conformal map projections on direct georeferencing, International Archives of Photogrammetry, *Remote Sensing and Spatial Information Sciences*, 34(3A):283–288.

Roweis, S. Levenberg-Marquardt Optimization. *Informal Notes*. retrieved June 2009, <http://www.cs.toronto.edu/~roweis/notes/lm.pdf>

Schmid, C., R. Mohr, and C. Bauckhage, 2000. Evaluation of Interest Point Detectors, *International Journal of Computer Vision*, 37(2):151–172.

Schwarz, K.P. and M. Wei, 2000. INS/GPS Integration for Geodetic Applications, *Lecture Notes*, Department of Geomatics Engineering, University of Calgary, 117 p.

Showengerdt, R., 2007. Remote Sensing: Models and Methods for Image Processing, 3rd Edition, *Elsevier Academic Press*, New York, NY, 515 p.

Simon, D., 2006. Optimal State Estimation: Kalman, H_∞, and Nonlinear Approaches, *Wiley-Interscience*, New York, NY, 526 p.

Skaloud, J. and K. Legat, 2007. Theory and reality of direct georeferencing in national coordinates, *Journal of Photogrammetry and Remote Sensing*, 63(2):272-282.

Skaloud, J., 1999. Problems in Direct-Georeferencing by INS/DPGS in the Airborne Environment, *ISPRS Workshop on 'Direct versus indirect methods of sensor orientation'*, Commission III, Working Group III/1, Nov. 25-26, Barcelona, Spain, 9 p.

Strecha, C., T. Tuytelaars, and L. Van Gool, 2003. Dense Matching of Multiple Wide-baseline Views, *Proceedings of the Ninth IEEE International Conference on Computer Vision*, Oct. 14-17, Nice, France, 8 p.

- Sullivan, D. and A. Brown, 2002. High Accuracy Autonomous Image Georeferencing Using a GPS/Inertial-Aided Digital Imaging System, *Proceedings of the Institute of Navigation National Technical Meeting*, San Diego, CA, pp. 598-603.
- Taylor, C.N., and E.D. Andersen, 2008. An Automatic System for Creating Geo-referenced Mosaics from MAV, *IEEE/RSJ International Conference on Intelligent Robots and Systems*, Sept. 22-26, Nice, France, 6 p.
- Toth, C., S.W. Shin, D.A. Grejner-Brzezinska and J.H. Kwon, 2008. On Accurate Time Synchronization of Multi-Sensor Mapping Systems, *Journal of Applied Geodesy*, 2(3):159–166.
- Triggs, B., P. McLauchlan, R. Hartley, and A. Fitzgibbon, 1999. Bundle Adjustment: A Modern Synthesis. *Vision Algorithms: Theory and Practice*, Springer-Berlin, pp. 153-177.
- Van Rossum, G., et al. Python Language Website, retrieved June 2009: <http://www.python.org/>.
- VIA EPIA, 2009. EPIA Specifications, VIA Technologies, Inc., retrieved June 2009: http://via.com.tw/en/products/embedded/ProductDetailTabs.jsp?motherboard_id=690
- Wackrow, R., 2008. Spatial Measurement with Consumer Grade Digital Cameras, *PhD Thesis*, Loughborough University, 241 p.
- Watts, A., W.S. Bowman, A.H. Abd-Elrahman, A. Mohamed, B.E. Wilkinson, J. Perry, Y. Kaddoura and K. Lee, 2008. Unmanned Aircraft Systems (UASs) for Ecological Research and Natural-resource Monitoring, *Journal of Ecological Restoration*, 26(1):13-14.
- Wilkinson, B.E., 2007. The Design of Georeferencing Techniques for an Unmanned Autonomous Aerial Vehicle for Use with Wildlife Inventory Surveys: A Case Study of the National Bison Range, Montana. *Master's Thesis*, University of Florida, 115 p.
- Wolber, G. and S. Zokai, 2000. Robust Image Registration Using Log-Polar Transform. *Proceedings of the IEEE International Conference on Image Processing*, Sept. 10-13, Vancouver, Canada, pp. 493-496.
- Wolf, P., and B. Dewitt, 2000. Elements of Photogrammetry with Applications in GIS, 3rd Edition, McGraw-Hill, Boston, MA, 608 p.
- World File, 2008. “FAQ: What is the format of the world file used for georeferencing images?”, ESRI, Inc., Article ID: 17489, retrieved July 2009, <http://support.esri.com/index.cfm?fa=knowledgebase.techarticles.articleShow&d=17489>
- Wu, J., G. Zhou and Q. Li, 2006, Calibration of Small and Low-Cost UAV Video System for Real-Time Planimetric Mapping, *International Geoscience and Remote Sensing Symposium*, July 31-Aug. 4, Denver, CO., 4 p.

Xiang, H. and L. Tian, 2007. Autonomous Aerial Image Georeferencing for an UAV Based Data Collection Platform Using Integrated Navigation System. 2007 ASABE Annual International Meeting, June 17-20, Minneapolis, MN, 28 p.

Xsens MTi-G, 2009. MTi-G™ User Manual, Xsens, Inc., 78 p.

Yastikli, N. and K. Jacobsen, 2002. Investigation of Direct Sensor Orientation for DEM Generation, *Proceedings of ISPRS Commission I Symposium*, Denver, CO, 6 p.

Zebedin, L., A. Klaus, B. Gruber-Geymayer, and K. Karner, 2006. Towards 3D map generation from digital aerial images. *Journal of Photogrammetry and Remote Sensing* 60(6):413-427.

Zhu, Z., E.M. Riseman, A.R. Hanson, and H. Schultz, 2005. An Efficient Method for Geo-referenced Video Mosaicing for Environmental Monitoring, *Machine Vision and Applications*, 16(4):203-216.

Zitová, B. and J. Flusser, 2003. Image Registration Methods: A Survey, *Image and Vision Computing*, 21(11):977-1000.

BIOGRAPHICAL SKETCH

John Hendrix Perry has always had a fascination with science and technology. Despite his recent attempts at specialization in the field of geomatics, he is a generalist with a broad background in programming, electronics, philosophy, music, and variety of other muses. He is an avid reader and enjoys longs walks in the park as long as it accompanies a vigorous debate. He started working at the age of 14 washing dishes and has been employed at some job or other nearly continuously since.

John was admitted to the University of Florida on a National Merit Scholarship and completed an undergraduate degree in geomatics in a more or less reasonable amount of time. He met a number of interesting people and worked on a number of interesting projects, including a stint with Engineers Without Borders, wherewith he travelled to the Republic of Macedonia to the birthplace of Philip the Great to map a landfill and sewer system. As part of this project, he received a University Scholars Program grant and participated in a Davis grant and EPA P3 grant. He was a teaching assistant for two classes in the Geomatics Program.

Upon graduation in 2007, he worked for the Geomatics Program full-time at a newly established campus in Plant City, FL concurrent with his first year of graduate studies. Upon returning to Gainesville in 2008, he commenced work on the NOVA II project. In related research, he was presented with an Institute of Navigation Best Presentation award. Recently, he has been awarded a National Science Foundation Graduate Research Fellowship and a University of Florida Alumni Fellowship. He is the author or coauthor of eight academic works that have been presented or published, with three more in manuscript. His graduation with a Master of Science in forest resources and conservation with a concentration in geomatics and a minor in mechanical and aerospace engineering is expected forthwith. He will commence study for a PhD in the fall of 2009 at the University of Florida. Go Gators.